LBL--27632

DE90 000125

Mapping of Upper Electronic Reaction Surfaces by Tuned Laser Photolysis and by Absorption and Emission Spectroscopies

By

Meredith Ann Morgan

PhD Thesis

July, 1989

Chemical Biodynamics Division
Lawrence Berkeley Laboratory
University of California
Berkeley, CA 94720

This work was supported by the Office of Energy Research, Office of Basic Energy Sciences, Chemical Sciences Division of the U.S. Department of Energy, under Contract Number DE-AC03-76SF00098.

Mapping of Upper Electronic Reaction Surfaces by Tuned Laser Photolysis and by Absorption and Emission Spectroscopies

by

Meredith Ann Morgan

Abstract

Potential energy surfaces for photorotamerization of two intramolecularly hydrogen-bonded molecules, o-hydroxybenzaldehyde (OHBA) and methyl salicylate (MS), isolated in cryogenic matrices have been spectroscopically mapped. In addition, the external heavy atom effect of krypton and xenon matrices on the coupling between the S_1 and T_1 surfaces of 4-(dimethylamino)benzonitrile has been examined.

Based on steady-state and time-resolved emission measurements, the S_1 state of OHBA is postulated to be an n,π^* hydrogen atom transfer state with a 10.6 kcal barrier to formation of the non-intramolecularly hydrogen-bonded photorotamer, while S_2 is proposed to be a π,π^* proton transfer state, with a 17.7 kcal barrier. A higher quantum yield is detected upon photolysis of OHBA a few kcal above the S_1 barrier. The five-fold greater quantum yield for the forward over the reverse reaction observed within 15 kcal of the S_1 0-0 energy is interpreted to be a manifestation of reaction on either the triplet surface or in the vibrationally excited ground state manifold.

In contrast, photolysis of MS in xenon or SF_6 matrices yields a rotamer having an intramolecular hydrogen-bond between the phenolic hydrogen and the ether oxygen of the ester moiety. The results from time-resolved and steady-state emission spectroscopies are consistent with MS having an

S_1 π,π^* proton transfer state with a 12.7 kcal S_1 barrier to formation of the ether-bonded conformer. The forward reaction proceeds at the S_1 0-0 energy by either a triplet or vibrationally excited ground state mechanism. This reaction was found to not be photochemically reversible.

Heavy atom matrices are known to increase rates of spin-forbidden processes. The phosphorescence intensity of DMABN increases in krypton and xenon matrices, while the fluorescence intensity, and phosphorescence and fluorescence lifetimes, decrease. These effects are interpreted in terms of a model in which the phosphorescence rate constant increases 300-fold in xenon compared to argon, while the rate constants for intersystem crossing and nonradiative relaxation from the triplet state increase by factors of less than 5. Lifetime measurements in argon matrices doped with heavy atoms indicate that even one heavy atom neighbor has a signficant effect on both singlet and triplet lifetimes.

ACKNOWLEDGEMENTS

First and foremost, I thank my research advisor, Professor George Pimentel. His ideas and insight were crucial to this dissertation. While I am deeply saddened by the recent death of this enthusiastic, inventive, and courageous teacher and scientist, I am grateful for the opportunity I had to learn from, and be inspired by, this wonderful man.

I would also like to thank Professors Herb Strauss and Brad Moore, who stepped in when needed and provided valuable input on the final drafts.

The studies of o-hydroxybenzaldehyde and methyl salicylate were a collaborative effort with Ed Orton. His initial emission experiments, and work identifying the ground state rotamer of o-hydroxybenzaldehyde were invaluable to this study, as were the many fruitful discussions throughout my five year's here.

I thank Ward Brown, who not only wrote the computer program and assembled the electronics of the fluorimeter used extensively in this work, but who also helped maintain and modify it long after his studies here were completed.

To the family, friends, fellow Pimentel group members, professors, and inhabitants of the round building, who provided encouragement, discussion, answers, laughter, Kleenexes, and companionship, I am forever grateful.

TABLE OF CONTENTS

LIST OF FIGURES

LIST OF TABLES

CHAPTER I. INTRODUCTION

Excited state chemistry is determined by the energy and shape of the electronic potential surfaces, and the coupling to other nearby surfaces. However, little is experimentally known about the reaction surfaces of most photochemically reactive molecules. The aim of this work is to map electronic surfaces of photochemically reactive molecules in cryogenic matrices. With information from vibrational and electronic absorption spectroscopies, steady-state excitation and emission, time-resolved emission, tuned laser photolysis, and variation of the spin-orbit coupling ability and cage size of the matrix, both the contours of the electronic potential surfaces and the dynamics of reaction on those surfaces are better understood.

The choice of a cryogenic rare gas matrix environment for this study involves three considerations. Firstly, the temperature range accessible with a matrix is important. High enthalpy photoproducts can be trapped for leisurely study at 12K. Although o-hydroxybenzaldehyde and methyl salicylate, two subjects of this work, exist almost exclusively as their internally hydrogen-bonded conformers in aprotic solvents at room temperature, the most stable non-hydrogen bonded rotamer of o-hydroxybenzaldehyde and the alternate hydrogen-bonded conformer of methyl salicylate can be photolytically produced and trapped in cryogenic matrices. Since activation energies for thermal regeneration of the initial internally hydrogen-bonded forms are in the range of only 10 kcal, this would not be possible at high temperatures. On the other hand, it is sometimes desirable to employ a matrix that can be deliberately raised to a high temperature to investigate thermal processes without diffusion. Use of xenon as the host matrix allows access to temperatures as high as 75K, while SF_6, which shares many characteristics with the inert rare gases, allows access to temperatures as high as 100K while still maintaining isolation of the guest molecule.

Secondly, high resolution absorption and emission spectra of trapped species are easily obtained in rare gas matrices and tell much about potential surfaces of both the ground and excited states. Precise identification of ground state conformers is possible with high resolution infrared spectra. With low temperature high resolution excitation and emission spectra one can accurately determine electronic 0-0 transition energies. By correlation of vibrational spacing in emission spectra with ground state vibrational frequencies one can identify chromophores, while the Franck-Condon maximum is an indication of the degree of displacement of the excited state relative to the ground state. Anharmonicity in the ground state potential well is manifested by a change in the vibrational spacing upon emission into the higher vibrational states, while the disappearance of vibrational features may signal the unbound region of the potential surface. Analogously, vibrational features in excitation and absorption spectra can indicate bond strengths, anharmonicity, and bound regions in the excited states.

Thirdly, the rare gas matrix affords an opportunity to measure barriers to reaction. The poor coupling between guest molecules and the low energy phonon modes of the crystalline rare gases means that evolution of the initially excited superposition of vibrationally excited states into one characterized by the nuclear geometry of the product molecule is better able to compete with deactivation or cooling of the vibrationally excited molecule. Excitation to a superposition of states above a barrier to reaction might then result in direct formation of the product species, with a consequent higher reaction quantum yield at those energies compared with excitation to an energy below the barrier. Frei and Pimentel[1] report large increases in quantum yields with increasing photolysis energy for infrared initiated reactions in rare gas matrices. For example, they determined that the reaction $C_2H_4 + F_2$ has a quantum yield 250 times larger upon photolysis with 5.4 kcal/mole photons as compared to 2.7 kcal/mole photons, very much in line with the 4.5 kcal barrier to reaction measured in the gas phase. Thus, it has been shown that by measuring the wavelength dependence of infrared initiated reaction quantum yields one can detect ground state barriers to reaction.

There is much evidence to suggest that the analogous electronically excited state experiment is feasible, although complicated somewhat by the presence of a number of closely spaced or overlapping electronic absorptions. Michl et al.[2] measured the quantum yields for the photolyses of two annellated cyclobutenes to phenanthrene and pleiadene, respectively, at a number of different wavelengths in 77K hydrocarbon glasses. The higher quantum yields measured at the greater photolysis energies indicate that reactions from vibrationally excited or higher electronic states can compete with deactivation to the negligibly reactive thermalized S_1 state.

The work of Rentzepis and Bondybey[3] quantifies the lifetime of some higher vibrational levels in the S_1 manifold of napthazarin. They report fluorescence from these vibrationally excited states with lifetimes as long as 320 picoseconds in argon matrix. If this time scale is generalizable to most guest molecules in rare gas matrices, it is very reasonable to think that most unimolecular reactions could compete effectively with deactivation. Thus, it may indeed be possible to measure an excited state barrier to reaction by measuring the wavelength dependence of the quantum yield to reaction in a rare gas matrix environment.

An ideal subject for a mapping study of this type would yield information from all these spectroscopic and photolytic techniques. Unimolecular rearrangements are one class of particularly appropriate subjects, potentially yielding information about the reaction surface in both the forward and reverse directions. Another favorable attribute is fluorescence. Not only does fluorescence confirm the 0-0 energy of the S_1 surface, but fluorescence of both the reactant and product implies two excited state minima corresponding to the two ground state minima, and therefore a state barrier on the S_1 surface. It is of course also desirable to have structured fluorescence, phosphorescence, and excitation spectra, so as to gain maximal information about the chromophores and excited state bonding.

o-Hydroxybenzaldehyde (OHBA-C, below) fulfills many of the above criteria. Upon UV photolysis in cryogenic matrices it undergoes reversible rotation to yield a non-hydrogen-bonded conformer (OHBA-F).

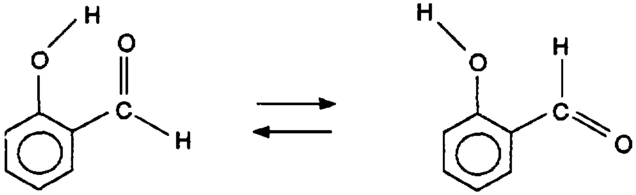

OHBA-C

OHBA-F

OHBA-F has no detectable fluorescence, but does exhibit highly structured phosphorescence and absorbance into both S_1 and S_2. OHBA-C exhibits no phosphorescence, but has broad, structureless fluorescence excitation and emission profiles with weak 0-0 transitions. The fluorescence from OHBA-C and the structure into OHBA-F's S_1 absorption system indicate that there are two minima in S_1, and therefore that there is a barrier to reaction on the S_1 surface. The structure present in OHBA-F's excitation and emission spectra does much to enhance our knowledge of the excited states. Analysis of the reaction quantum yields is simplified by the fact that there is less than one per cent loss to side reactions upon photolysis to steady state in either direction.

Methyl salicylate in its normal form MS-C shares some characteristics with OHBA-C. It has a broad fluorescence band with a weak 0-0 transition, and no detectable phosphorescence. On the other hand, the photoproduct MS-E, identified herein from IR spectra, bears little resemblance to OHBA-F. Not only does it contain an (albeit weaker) internal hydrogen bond, but it is also fluorescent. MS-E's phosphorescence has much more congested vibrational structure and a very different lifetime from that of OHBA-F. Furthermore, photolysis of MS-E does not regenerate MS-C at the wavelengths investigated. However, as with OHBA, the S_1 surface of MS must have two minima, as fluorescence is detected for each of the two forms.

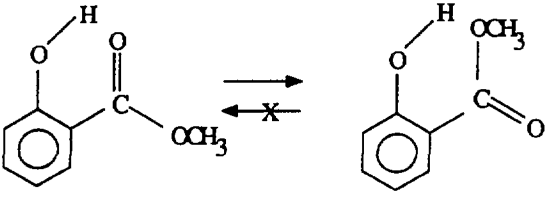

MS-C MS-E

The excitation, emission, and photolysis characteristics of MS-C and MS-E provide an extremely interesting contrast to those of OHBA-C and OHBA-F, and are discussed in relation to the reaction surfaces of OHBA-C and OHBA-F.

The coupling between electronic surfaces plays a significant role in determining the progress of a photochemical reaction. There are now several examples indicating that the spin-orbit coupling ability of the matrix environment can control branching ratios of products in the matrix via the external heavy atom effect.[4-7] Direction to the triplet surface with an external heavy atom matrix such as xenon, or by triplet sensitization with a molecule such as mercury, can lead to an entirely new set of products from those generated in a matrix such as argon. A natural conclusion to draw from these examples is that without help in crossing over to the triplet surface by a heavy atom (either by substitution on the molecule itself or as part of the solvent), excitation to the singlet surface tends to lead to reaction on the singlet surface.

This study, characterizing the reaction surfaces of OHBA and MS, provides a test for this assertion. Data are presented showing that both OHBA-C and MS-C photolyze at or near their S_1 0-0 energies. Since the S_1 states are shown to be bound, this implies that at these lower energies reaction must proceed on either the triplet surface or in the vibrationally excited S_0 manifold upon photolysis at these lower energies. (The third possibility, that reaction proceeds by a tunneling mechanism, is dismissed since the rotating groups are so large.) The relative quantum yields for the forward and reverse reactions for OHBA in both argon and xenon have been determined at a number of different wavelengths, and are compared to determine whether reaction below the S_1 barrier proceeds on the triplet surface, and if so, whether or not assistance is needed to promote efficient transfer to the triplet surface. Singlet and triplet lifetimes have also been determined for both OHBA and MS, and provide further information about coupling between the singlet and triplet surfaces and the dynamics of reaction upon excitation at the S_1 0-0 energies.

The utilization of both steady-state and time-resolved matrix emission techniques permits quantification of the effects of heavy atom matrices on rates of spin-forbidden processes. The rates of intersystem crossing, fluorescence, phosphorescence, and non-radiative decay from the S_1 and T_1 states of dimethylaminobenzonitrile (DMABN, below) in argon, krypton and xenon matrices are modelled in Chapter V.

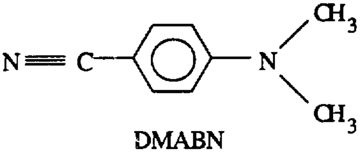

DMABN

The effect of a heavy atom matrix on the rate of intersystem crossing is of particular interest, in that branching between singlet and triplet reaction pathways is a function of this rate. Experiments with mixed argon:heavy atom matrices were done in order to explore the effect of a single heavy atom neighbor on singlet and triplet lifetimes of DMABN. Also discussed in Chapter V is the applicability of the DMABN results to interpretation of the singlet and triplet lifetimes of OHBA and MS.

All three of these molecules, OHBA, MS, and DMABN are of current interest. DMABN has been studied extensively, as it exhibits a second, red-shifted fluorescence in room temperature polar solvents[8]. Much work has been done to characterize the second fluorescent state, and to measure its excited state barrier to formation[9]. The excited state barrier of DMABN, in relation to this work in the rare gas matrices, is discussed in Chapter V.

As the non- or more weakly hydrogen-bonded forms OHBA-F and MS-E are of higher energy and have very different UV and IR absorption systems, they are of interest as prototypes for molecular energy or information storage systems. MS and OHBA also represent two of the simpler molecules which are thought to undergo either excited state proton or hydrogen atom transfer. The broad structureless or weakly structured fluorescence emissions of both OHBA-C and MS-C, with weak $S_1 \rightarrow S_0$ 0-0 transitions, are likely to be manifestations of the proton or hydrogen-atom transfer excited states. The implications of proton or hydrogen-atom transfer excited states to the singlet excited state reaction barriers are discussed.

Although characterization of excited states has been stressed up to this point, much of the work on the ground states is also new, particularly with regard to MS-E. MS-E has not previously been generated in a cryogenic matrix, owing to the large cage size and long photolysis times required to produce it. This work presents the first IR, the first phosphorescence, and the first high resolution condensed phase fluorescence spectra of MS-E, together with fluorescence and phosphorescence lifetimes, and in so doing sets to rest many questions about this molecule.

The remainder of this dissertation consists of: Chapter II, detailing the methods used to generate the vibrational and electronic absorption spectra, the excitation and emission spectra, and the photolysis quantum yields; Chapter III, presenting the results of the spectroscopic and photolysis quantum yield studies of o-hydroxybenzaldehyde and methyl salicylate; Chapter IV, discussing these results; Chapter V, which models the effects of external heavy atoms on photophysical rates of DMABN; and Chapter VI, which is a discussion of some general theoretical and experimental aspects of mapping excited state barriers by the wavelength dependence of the quantum yield, and suggestions of suitable subjects for future mapping projects.

CHAPTER II. EXPERIMENTAL

Materials

Methyl salicylate (Aldrich Chem. Co.) was purified by vacuum distillation, while o-hydroxybenzaldehyde was additionally purified by flash chromatography. Both substances were stored under nitrogen until immediately prior to use, whereupon they were degassed by at least four freeze-pump-thaw cycles. The first third of the sample was then pumped away, leaving the middle fraction with which to make the gas mixture. Deuteration of the phenolic hydrogen of OHBA and MS was achieved by mixing with a thirty-fold molar excess of MeOD (Aldrich, 99.5% pure), removing the MeOD by vacuum distillation, and repeating the process with another thirty-fold molar excess of MeOD. Without passivation of the glass deposition vacuum line, this resulted in a mixture with approximately 60% deuteration. DMABN (Aldrich Chem. Co.) was purified by flash chromatography, which removed an impurity detectable by thin layer chromatography. Argon (Pacific Oxygen Company, 99.998% pure), xenon (Airco, 99.9995% pure) and SF_6 (Matheson Gas Products, 99.8% pure) were used without further purification.

Matrices

Matrices were deposited onto the appropriate optical window (CsI for FTIR spectra, BaF_2 or sapphire for UV/Vis and emission spectra) cooled by a Displex Model CSW202 (Air Products and Chemicals, Inc.) closed cycle helium refrigerator. The window could be rotated for deposition, spectra, and photolysis within the vacuum shroud, which was maintained at a pressure of 10^{-6} Torr. Outer windows were of CsI for IR spectra and of CaF_2 for UV/Vis and emission spectra. Photolysis was achieved through a Suprasil or CaF_2 window.

Gas mixtures of OHBA and MS for IR experiments were made by allowing the room temperature vapor pressure of the degassed material to equilibrate with at least 75 Torr (MS mixtures) or 120 Torr (OHBA mixtures) of the rare gas for at least one hour, and usually three or more hours. As the vapor pressure of room temperature methyl salicylate in contact with an oil-covered mercury manometer is ~0.2 Torr (MKS Baratron), M:R (mole ratio, matrix:reactant) was at least 375:1. M:R for measurement of MS-C's fluorescence lifetimes was greater, ~1000:1. The vapor pressure of OHBA is somewhat higher (~.4 Torr, MKS Baratron), implying M:R of at least 300:1. Assuming three non-linear substitutional sites (25 nearest neighbors) in the hexagonal close-packed rare gas matrices and a statistical distribution, M:R of 375:1 gives ~94% isolation, with only a small fraction of the remaining 6% in a position to participate in intermolecular hydrogen-bonding. Matrices for UV absorption spectra were somewhat more concentrated (~200:1) so as to minimize scattering. The actual concentrations were however apparently often lower than those estimated from the vapor pressures, in that deposition of mixtures of the same concentration on subsequent days often showed increasing amounts of deposited guest molecules. This behavior is attributed to passivation of the hardware connecting the deposition vacuum line to the cold substrate window, in particular passivation of the greased connections to which these hydrogen-bonding species are attracted.

Matrices were deposited at approximately 0.3 mmole/hour for 0.25 to 2 hours, depending on the optical density desired. Argon matrices were deposited at 12K, xenon at 30K, and SF_6 at 12K for emission spectra and 30K for IR spectra.

DMABN matrices for quantum yield measurements and singlet lifetimes were made by flowing the matrix gas of 2 mmole per hour for 1 hour over the room temperature solid which was positioned between the gas metering valve and the cryostat. Matrices for the higher resolution and triplet lifetime studies were made by equilibrating the room temperature solid with 50 Torr of the matrix gas. The resulting mixture was then deposited at 0.5 mmole per hour for 40 minutes. The vapor pressure of DMABN opened to a vacuum line reaches less than 5 mTorr in one hour (MKS Baratron) at room temperature, implying that M/R in the higher resolution matrices is in excess of 10,000. M/R in the optically thick matrices used for the quantum yields is also estimated to be around 10,000. Optical thickness was determined in separate experiments with a UV spectrometer under appropriate deposition conditions. Argon matrices were deposited at 12K, krypton at 12 or 20K, and xenon at 12 or 30K. All spectra were recorded at 12K. Gas mixtures were prepared using standard manometric techniques. Usually two or more hours, but at least 30 minutes, were allowed for mixing per dilution.

IR Spectra

IR spectra (0.5 cm^{-1} resolution) were obtained with an IBM model IR97 FTIR. Photolysis of IR samples was achieved either with a 1000 Watt high pressure Hg-Xe lamp, or with the frequency-modified output of a DCR Nd:YAG-pumped (Quanta Ray) dye laser (Model PDL-I, Spectra Physics), fitted with filled-in doughnut optics. The dye laser was run in its end-pumped amplifier configuration to maintain a circular output. A Wavelength Extension System (Quanta Ray Model WEX-1) was used to either double the output of the dye laser, accessing wavelengths in the region 280-330 nm with the set of dyes Rhodamine 590, Rhodamine 610, Kiton Red, Rhodamine 640, and DCM (all from Exciton), or to add the 1.06 μm fundamental output of the Nd:YAG to the output of the dye laser, thereby accessing wavelengths in the region 366-407 nm with the aforementioned dyes. The UV output from the WEX was separated from the visible output with a Pellin-Broca prism, and then directed to the matrix with a series of four right angle turning prisms over a distance of ten meters, and defocussed with a quartz plano-convex lens (focal distance of 50mm) so as to just fill the 1" diameter matrix window. Photolysis powers were usually maintained at less than 0.6 mJoules per pulse at 10 Hz, and were measured immediately prior to and following photolysis with a Scientech model 38-0105 power meter placed between the final right angle turning prism and the lens. The output of the dye laser is selected with a grating, precise to ± .001 nm. Resolution of the dye laser output is on the order of 0.1 cm^{-1}, while the pulse width is approximately 5 nsec. The wavelength of the visible dye laser output was calibrated with a 1 meter single monochromator (McKee-Pedersen Instruments, Model MP-1018), which was in turn calibrated with mercury pen lamp and found to be correct to ±0.1 nm.

UV/Vis Spectra

UV/Vis spectra were obtained with a Shimadzu 2100 UV/Vis Spectrometer, at 0.1 or 0.2 nm bandpass as warranted by the resolution of the matrix. To determine relative UV extinction coefficients of OHBA-C in Ar as a function of wavelength, a spectrum of the 12K window was obtained prior to deposition, followed by a spectrum of the Ar:OHBA matrix, both using air as the reference. The next day, a correction for the scattering of the matrix gas itself was obtained by taking a spectrum of the cooled window, then depositing under identical conditions (temperature, flow rate) an equivalent amount of the pure matrix gas. The spectra of the cooled, bare windows served to ensure that the condition of the windows and spectrometer had not changed, so that the relative extinction coefficients could be obtained as the difference between the absorption spectrum of OHBA-C in argon and that of argon itself. The relative extinction coefficients of OHBA-F were obtained by photolyzing the matrix with a 1000 Watt high pressure Hg-Xe lamp through a six inch water filter and a 7-60 Corning glass filter (passing light between 300 and 380 nm) for ten minutes, followed by subtraction of the pure argon matrix absorption spectrum.

The equivalent correction for scattering was more difficult in xenon, since it proved difficult to reproduce the high temperature deposition and subsequent cooling necessary with this highly scattering matrix material. Thus, extinction coefficients of OHBA-C and OHBA-F were obtained from a difference spectrum of the OHBA:Xe matrix minus the cooled, bare window. The contribution of scattering to the UV absorption difference spectrum, and thus the relative extinction coefficients, was then approximated by assuming a straight line between the "absorbance" at 400 nm and that at 270 nm. While scattering has a theoretical v^3 dependence, the pure argon matrix spectrum showed that this straight line approximation is valid in this short wavelength region.

UV spectra of methyl salicylate and its photoproduct in xenon were similarly generated with subtraction of the bare window spectrum. Photolysis was achieved by photolyzing with the laser for 29 hours at 320 nm (6 mWatts average power).

Steady state Excitation and Emission Spectra

Steady state excitation and emission spectra were collected using a Spex Fluorolog 2 (Model 212T) spectrofluorometer equipped with single photon counting discriminators and interfaced to a DEC PDP LSI11 for data acquisition and processing. The BaF_2 or sapphire window was positioned so that excitation was approximately 15 degrees from the normal to the surface, and emission light was collected at 30 degrees from the normal. Approximately four percent of the excitation light from the 150 watt xenon source was split off to a rhodamine B quantum reference counter to correct for the wavelength dependence of the excitation intensity. Additionally, an identical rhodamine solution was periodically placed in the sample compartment in order to generate the correction factors accounting for differences in the sample and quantum reference counter paths. A standardized lamp (Optronic Laboratories) was used to generate a correction for the spectral response of the emission monochromator and PMT. The 150 Watt xenon excitation source also served as a photolysis source for generation of OHBA-F and MS-E.

Steady state emission spectra were recorded with a 4.0 nm bandpass at the excitation monochromator and 0.1-4.0 nm bandpass at the emission monochromator. For excitation spectra, the bandpass was 0.1-4.0 nm at the excitation monochromator and 4.0 nm at the emission monochromator. Spectra were taken in 0.1-1.0 nm increments, integrating for 0.25-30 seconds at each point, depending on the signal intensity and the resolution desired. Wavelength accuracy of the monochromators was determined using a mercury pen lamp, and was found to be ± 0.2 nm between 250 and 550 nanometers.

Phosphorescence Lifetimes

Phosphorescence decay curves were also obtained using the steady state fluorometer. For lifetimes longer than 0.05 seconds, a mechanical shutter was used to cut off the excitation light after steady state illumination (shutter time << .02 seconds). The decay curves were then recorded by counting photons emitted in 0.1 second intervals and analyzed by a non-linear least-squares fitting program.

The millisecond lifetime of OHBA-F's phosphorescence was determined in a similar manner by connecting the output of the emission PMT directly to a digital oscilloscope (Explorer IIIA, Nicolet Instrument Corporation), triggered by the closure of a fast electronic shutter (UniBlitz Model 100-2B, A. W. Vincent Assoc., Inc.). The recorded signal decay (5 μsec/channel) was subsequently plotted on an x-y plotter and the process repeated three times to reduce the noise Discounting the first millisecond of decay, encompassing the time of shutter closure, the decay curve was analyzed by the above fitting program, assuming a single lifetime. The lifetime was determined with excitation at 290 nm and emission at 404 nm (4 nm bandpass) in argon matrix.

Fluorescence Lifetimes

Singlet lifetimes were obtained using a time-correlated single photon counting H_2 flashlamp system. The repetition rate of the flashlamp (PRA, model 510B) was 30 KHz. Excitation light was attenuated with neutral density filters and/or the iris adjacent to the source shutter so that less than 2% (or 600 counts per second) of the excitation pulses resulted in an event at the emission PMT. For each emission event, the time difference between reception of photons at the PMT next to excitation source and the fluorescence emission photon was, by way of a time-to-amplitude converter, recorded in one of the 1028 channels of a Pulse Height Analyzer (Northern Scientific Inc., Model NS636). In this manner a histogram of the emission profile is collected, with roughly 10,000 counts collected in the maximum channel. Selection of excitation and emission light was achieved with filters, as given in Table I.

The matrix was positioned so that excitation was approximately 20 degrees from the normal, and emission was collected by a lens gathering

Table I. Filters Used in Nanosecond Lifetime Apparatus

Molecule	Excitation Filter	Emission Filter
OHBA-C	7-37 colored glass (Corning Glass), 320-400 nm	4-65 colored glass (Corning Glass) 460-600 nm
MS-C	282 nm interference (29 nm bandpass at 10% of maximum transmission, Baird Atomic)	3-74 colored glass (Corning Glass) 400-4600 nm
MS-E	261 nm interference (18 nm bandpass at 10% of maximum transmission, Baird Atomic)	7-60 colored glass (Corning Glass) 300-380 nm
DMABN	261 nm intereference (18 nm bandpass at 10% of maximum transmission, Baird Atomic)	7-37 colored glass (Corning Glass) 320-380 nm

light between 60 and 80 degrees from the normal, (i.e. 80 to 100 degrees from the incident angle) so as to minimize scatter. The instrument response functions were obtained by replacing the excitation filter with one passing the same wavelength light as the emission filter. The instrument response function showed a lamp pulse of about 2.0 nsec FWHM. Data analysis was carried out on a VAX 11/780 computer using an iterative deconvolution program, and the quality of the fit was determined by the reduced χ^2 ($R\chi^2$) values and visual inspection of the weighted residuals.

Reaction Quantum Yields for the Photolysis of OHBA

Reaction quantum yields for the photolysis of OHBA-C were obtained by monitoring the disappearance of OHBA-C, represented by the diminishing height of its 1673 cm^{-1} carbonyl stretch band, as a function of incident photons at a particular wavelength. The decay curves were analyzed as a single exponential decay by a non-linear least-squares fitting curve, which yielded a rate constant for the photolysis of OHBA-C to OHBA-F when evaluated at zero incident photons. Matrices for these experiments were as thin as was practical, typically .1 mmoles of a 300:1 (or greater) Ar:OHBA mixture deposited on the 1" CsI window, giving an absorbance height of ~.1 absorbance units in the IR. Deposition under identical conditions showed that the maximum absorbance in the UV for such a matrix is about .2 absorbance units. Thinner matrices were used for photolysis at the wavelengths of maximum absorption. Each photolysis curve was generated from a freshly deposited matrix.

Similar curves were generated for the photolysis of OHBA-F to OHBA-C by monitoring the disappearance of the 1701 cm^{-1} carbonyl stretch band after generation of >97% pure OHBA-F, either by photolysis at 325 nm with the dye laser or by photolysis with the 1000 Watt Hg-Xe lamp through a colored glass filter (Corning 7-60, passing light between 300 and 380 nm).

Ratios of the forward reaction to the reverse reaction were generated by determining the relative amounts of OHBA-C and OHBA-F from the areas of the respective carbonyl peaks (1668 - 1679 cm^{-1} for OHBA-C and 1695 - 1709 cm^{-1} for OHBA-F) after photolysis for extended periods to achieve a steady state mixture. Matrices for these experiments were generally much thicker, with typical absorbances at 1675 cm^{-1} of 0.7 absorbance units for the initially deposited matrix of OHBA-C. Ratios at a few photolysis wavelengths were also determined from thin matrices from relative heights of the carbonyl peaks.

Estimation of ΔH for the Reaction OHBA-C→OHBA-F

The enthalpy and entropy of reaction were determined from the temperature dependence of the UV absorption spectrum of OHBA in solutions of n-decane (99+%, Aldrich Chemical Company). The temperature of the solution was maintained at ± 0.1°C with a Neslab RTE5B Refrigerated Circulating Bath, which circulated a mixture of ethylene glycol and water through a brass block in thermal contact with the 1 cm quartz UV cell placed in the Shimadzu 2100 UV spectrophotometer. UV spectra at a resolution of 2 nm were recorded at 20.2, 54.0, 68.2, 82.1 and 96.5°C, as determined by an iron-constantin thermocouple in contact with the brass block cell holder. The concentration of the solution was 2.75 x 10^{-4} molar at 22°C. The temperature dependence of the solution density (and hence concentration) was approximated by measuring the absorbance of a sample of n-decane at its 216 nm shoulder at each of the temperatures and assuming adherence to Beer's Law.

CHAPTER III. RESULTS

o-HYDROXYBENZALDEHYDE

Ground States of o-Hydroxybenzaldehyde

Figure 1 is an FTIR difference spectrum of OHBA-C (negative features) and its photolysis product (alternating 20 second intervals of 291 and 297 nm laser light, 3 minutes total photolysis time, 4 mWatt power). The product has been identified as the non-hydrogen bonded conformer OHBA-F[10], pictured below.

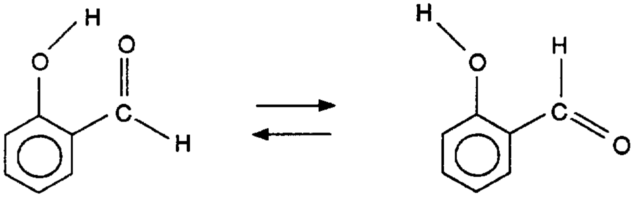

OHBA-C **OHBA-F**

OHBA-F is identified as a non-hydrogen-bonded form by the carbonyl and phenolic O-H stretch frequencies, located at 1701 cm^{-1} and 3632 cm^{-1}, respectively, in argon matrix, and similar in value to those of the simpler molecules benzaldehyde (1718 cm^{-1}) and phenol (doublet, 3639 and 3635 cm^{-1}). These frequencies are strikingly different from those of the intramolecularly hydrogen-bonded OHBA-C, whose carbonyl and O-H stretches are red-shifted to 1673 and ~3195 cm^{-1}, respectively. The O-H stretch of OHBA-C displays the breadth typical of hydrogen bonded systems, whereas the O-H stretch of OHBA-F is sharp. The red-shifted carbonyl and O-H stretches of the hydrogen-bonded OHBA-C and the corresponding carbonyl and O-H stretches of the non-hydrogen bonded OHBA-F are labelled in Figure 1. These assignments were verified by deuteration of the phenolic group and ^{18}O substitution of the aldehydic oxygen.[10]

Figure 1. FTIR difference spectrum in 12K argon matrix of OHBA-C (negative features) and its photolysis product (positive features) after 3 minutes total photolysis with 20 second intervals of alternating 291 and 297 nm light at 4 mWatt power. The frequencies of the carbonyl and OH stretches are noted.

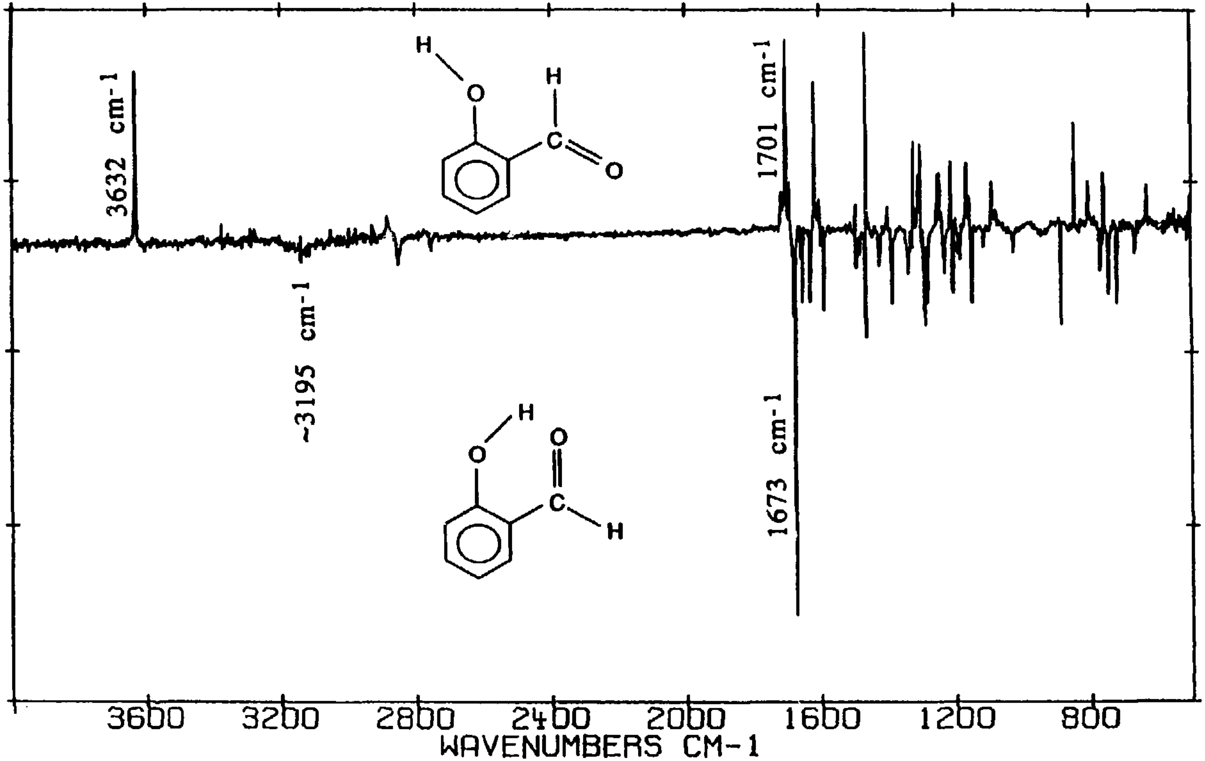
3632 cm-1
~3195 cm-1
1701 cm-1
1673 cm-1
H
O
H
C
O
O
H
O
C
H
3600
3200
2800
2400
2000
1600
1200
800
WAVENUMBERS CM-1

There are several possibilities for a non-hydrogen bonded conformer of OHBA-C; ones in which either or both the hydroxyl and the aldehydic groups are rotated out of the aromatic plane, one in which only the aldehydic group has rotated 180 degrees, one in which only the hydroxyl group has rotated 180 degrees, and one in which both groups have rotated 180 degrees. The first possibility is dismissed by the fact that approximately 3.5 kcal are required to rotate the hydroxyl group of phenol[11], and 7.9 kcal to rotate the aldehydic group of benzaldehyde[12] out of the molecular plane. The barriers to rotation of these groups are thought to be large because there is considerable conjugation of the non-bonded hydroxyl electrons and the π electrons of the carbonyl group with the aromatic ring.

Of the three planar possibilities, the one formed by 180 degree rotation of the aldehyde group alone does not seem at all plausible since in this conformation the two hydrogen atoms are in very close proximity. There is however convincing evidence that the aldehyde group does rotate, in that the infrared spectrum of OHBA-C's photoproduct is strikingly similar to that of o-fluorobenzaldehyde[10], both in the intensity pattern and frequency location of all absorptions not particular to the fluorine or the hydroxyl group. o-Fluorobenzaldehyde's predominant form is a planar one, in which the aldehydic group is rotated such that the aldehydic proton is adjacent to the fluorine atom, thereby minimizing the repulsive F - C=0 interaction and maximizing the attractive interaction between the aldehydic proton and the fluorine[13]. Thus, the coincidence of the infrared absorptions of OHBA-F and o-fluorobenzaldehyde, particularly in the regions pertaining to motions of the aldehyde group, suggests that the aldehydic proton in OHBA-F is adjacent to the phenolic oxygen. Further evidence that the photoproduct of OHBA-C entails rotation of the aldehydic group is provided by the relative photolysis rates of OHBA-C and its methylated analogue, o-hydroxyacetophenone. While OHBA-C photolyzes quite readily in argon matrix, o-hydroxyacetophenone photolyzes much more slowly[14], presumably due to the larger size of the rotating ketone group. Thus, the conclusion is that photolysis of OHBA-C leads to 180 degree rotation of both the aldehydic and hydroxyl groups, yielding the structure OHBA-F. IR frequencies of OHBA-C and OHBA-F are given in Table II, along with approximate relative intensities.

Figure 2 is a portion of the IR spectrum of a steady-state mixture (photolysis wavelength 309.0 nm) of OHBA-C and OHBA-F, showing the carbonyl stretch region. The carbonyl stretch absorptions of both OHBA-F and OHBA-C, and in fact all the infrared absorptions of these two conformers, are doublets or higher multiplets, split by at most a few wavenumbers. The immediate concern is that one of the sets of absorptions might be due to multimers capable of forming intermolecular-hydrogen bonds. However, it was confirmed by dilution studies that neither of the OHBA-C carbonyl peaks shown in Figure 2 is due to multimers, as matrices with M/R as high as 750:1 had the same peak height ratio in the initially deposited matrix as more concentrated matrices.

The relative intensity of OHBA-C's carbonyl stretch peaks is however sensitive to temperature, the lower frequency stretch being favored even more at higher temperatures, while cooling back to 12K retrieves the original population distribution. The relative intensity of these two peaks can also be affected by photolysis. Photolysis at 314.1 nm of a matrix containing >97% OHBA-F favors selective photolysis of the lower frequency carbonyl stretch band of OHBA-F, with selective regeneration of the higher

Table II. Infrared Absorptions (cm^{-1}) of OHBA-C and Its Photoproduct OHBA-F in 12K Ar Matrix

OHBA-C	rel. int.	OHBA-F	rel. int.
2850.2	w	3632.2	v s
2751.3	w	2883.9	w
1680.6	sh, w	2770.7	v w
1674.8	d, vs	1714.9	sh, m
1673.2		1702.8	t, s
1655.3	sh, w	1701.8	
1650.3	m	1700.6	
1627.8	m	1690.8	m
1593.6	w	1649.3	w
1586.8	m	1615.3	s
1519.3	v w	1615.3	s
1494.3	d, m	1601.8	m
1491.4		1511.4	w
1482.2	w	1495.5	m
1465.8	m	1464.6	s
1450.1	v w	1401.7	m
1425.3	w	1323.8	m
1390.4	sh, w	1309.6	m
1386.7	m	1302.6	m
1388.8	w	1251.1	m
1325.5	w	1244.7	m
1299.5	w	1211.5	m
1288.6	m	1197.0	w
1280.4	m	1176.8	w
1232.0	d, w	1165.9	m
1229.1		1156.5	m
1206.4	d, m	1092.6	m
1204.0		1083.0	w
1190.5	t, w	845.7	m
1185.9		805.5	m
1184.2		760.4	d, m
1177.0	v w	757.5	
1149.3	m	633.6	m
1116.7	w	502.9	m
1029.4	w		
885.5	m		
773.7	w		
768.6	w		
759.4	m		
744.7	m		
721.3	m		
668.3	w		
563.7	v w		
539.3	v w		

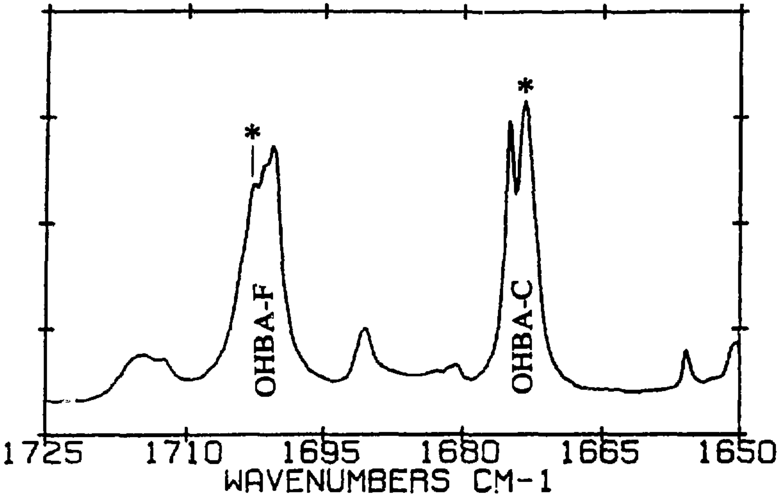

Figure 2. Expanded FTIR spectrum of a steady state mixture of OHBA-C and OHBA-F in argon matrix after extended photolysis at 309.0 nm. Asterisks mark the carbonyl stretch bands of the higher energy sites.

frequency carbonyl stretch of OHBA-C, while photolysis at 313.7 nm favors diminution of the higher frequency carbonyl stretch of OHBA-F and regeneration of the low frequency stretch of OHBA-C.

An explanation for these phenomena is that there are two (or more) sites for OHBA-C in argon matrix, the higher energy one(s) having the lower frequency carbonyl stretch absorption while the corresponding OHBA-F form has a higher frequency carbonyl stretch transition and slightly lower energy electronic transitions in the 314-309 nm region. As all infrared peaks are split by at most a few wavenumbers, large splittings would be expected with major conformational differences (such as juxtaposition of the carboxylic oxygen with the phenolic oxygen in an alternate non-hydrogen bonded form), and there is only one conformation possible for a planar internally' hydrogen-bonded form, the most likely explanation for the observed infrared absorption splittings is that of different sites.

UV/Vis Absorption and Emission of OHBA-C

Figure 3 is an electronic absorption spectrum of OHBA-C in argon matrix at 0.1 nm resolution. No vibrational structure is detectable in the long wavelength band, either in this spectrum or in the fluorescence excitation spectrum shown in Figure 4, Curve A (the structured features in Figure 4, Curve A, marked with asterisks, are due to excitation of the product OHBA-F, to which OHBA-C rapidly photolyzes). The fluorescence emission spectrum (Figure 4, Curve B) also displays no vibrational structure except from the contaminating photoproduct, either at this resolution of 4 nm or at higher resolution up to 0.1 nm. This fluorescence has a measured lifetime of 0.9 ± 0.2 nsec in both argon and xenon. The short lifetime, insensitive to the enhanced spin-orbit coupling of the xenon matrix, is an indication of an

Figure 3. 12K UV-Vis absorption difference spectrum (0.1 nm resolution) of 0.35 mmoles of an ~1:200 OHBA-C:Ar mixture deposited onto a 1" BaF_2 window, minus a corresponding spectrum of 0.35 mmoles Ar.

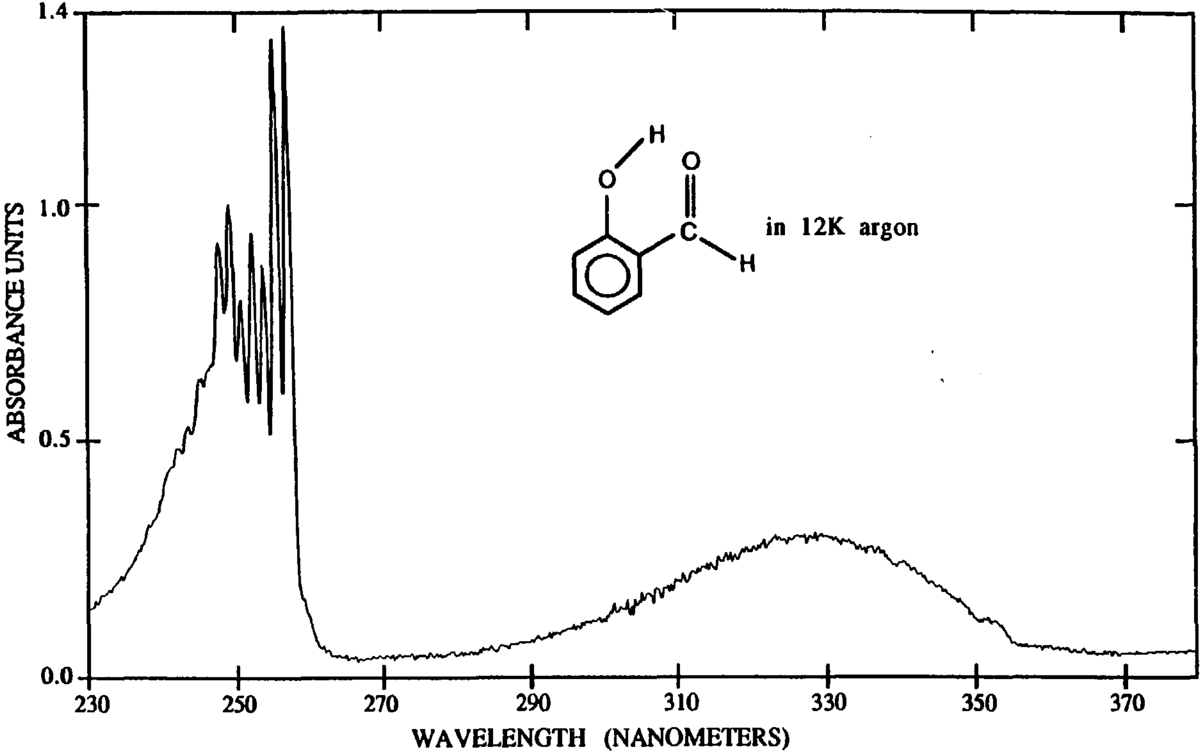
1.4
1.0
0.5
0.0
ABSORBANCE UNITS
230
250
270
290
310
330
350
370
WAVELENGTH (NANOMETERS)
H
O
O
C
H
in 12K argon

Figure 4. Curve A: Excitation spectrum of OHBA-C in 12K Ar, resolution of 4 nm, monitoring emission at 530 nm. Features marked with asterisks are due to product OHBA-F. **Curve B:** Emission spectrum of OHBA-C in 12K Ar, resolution 4 nm, with excitation at 325 nm.

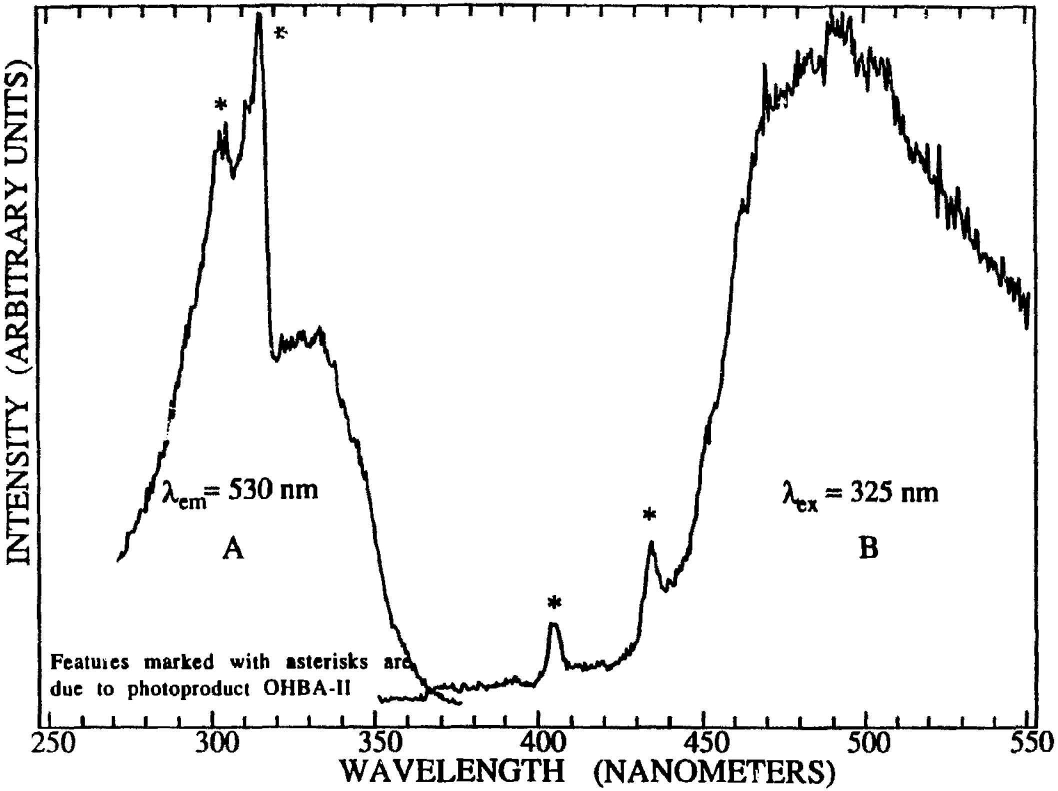
Features marked with asterisks are due to photoproduct OHBA-II

n,π* S_1 state[15].

The lack of vibrational structure in S_1, the large energy difference between the Franck-Condon maxima for excitation and emission, and the apparently low emission quantum yield make positive identification of the S_1 0-0 energy difficult, but it is tentatively assigned to 375 nm, the point at which there is an apparent excitation onset in Figure 4, Curve A. The crossing point between the excitation and emission spectra of Figure 4 appears to be closer to 365 nm, but at least some of the short wavelength, low intensity emission in Curve B is due to impurities present prior to deposition. Confirmation of 375 nm as the approximate S_1 0-0 energy is also obtained from photolysis in this region. The rate at 371.1 nm was one third that at 366.9 nm, which was in turn one fourth that at 364.9 nm, consistent with a 0-0 energy in the region of 375 nm. The longer value for the 0-0 transition wavelength is also reasonable in terms of that measured for a closely related compound, o-hydroxyacetophenone, whose 0-0 transition has been measured at 396.1 nm in durene mixed crystals[16].

The extinction coefficient of OHBA-C is approximately 3600 $M^{-1}cm^{-1}$ in n-decane solution at 330 nm, indicative of π,π* excitation. With S_1 assigned as n,π* from its fluorescence lifetimes, the abrupt increase in the extinction coefficient at 355 nm may then indicate the 0-0 energy of this π,π* state, which will be referred to as S_2.

The next major transition lies between 230 and 260 nm, and is highly structured. This transition, with an absorption coefficient comparable to that of the S_2 state, has previously been identified as π,π*[17], and will be referred to as S_3. It's 0-0 energy is identified as 256 nm, based on the following considerations. Three factors govern the intensity of a particular vibronic transition: symmetry, overall transition intensity, and Franck-

Condon overlap. The 0-0 transition in OHBA-C will not be symmetry forbidden, as the only symmetry element of OHBA-C is the horizontal plane. The 0-0 transition of this π,π^* state will also not be hidden because of an overall low transition probability. Finally, Franck-Condon factors vary fairly smoothly within a vibrational progression. As the intensities of the vibrational features do not taper off at the long wavelength end of this absorption band, but rather end abruptly with the longest wavelength peak at 254 nm, the leading edge of this peak is chosen as the S_3 0-0 energy. The 0-0 energies of OHBA-C are listed in Table IIIa.

UV/Vis Absorption and Emission of OHBA-F

The absorption, excitation, and emission spectra of OHBA-F are highly structured, as shown in Figures 5, 6, and 7, respectively. The phosphorescence excitation spectrum (Figure 6) mimics the absorption spectrum (Figure 5), with the appearance of additional, low intensity, features at long wavelength not detectable above the noise in the absorption spectrum. Again, the low symmetry of this molecule makes it reasonable to identify 0-0 energies from the onsets of absorption and emission. The relatively low intensity of the long wavelength features in Figure 6, and the distance of 1796 cm^{-1} from the first feature in the phosphorescence spectrum (Figure 7) are consistent with identification of the 377.8 nm feature as the 0-0 energy of an n,π^* transition. The phosphorescence spectrum was identified as such by its measured lifetime of 2.1 msec. The sharp onset at 314 nm is then interpretable as the 0-0 absorption band for an S_2 π,π^* transition, while the 405 nm peak in the phosphorescence spectrum signals the T_1 0-0 energy, having again invoked the argument that the 0-0 transitions of these bands should not be symmetry or Franck-Condon forbidden. Table IIIb lists the 0-0 energies for these three states in argon

Table IIIa. 0-0 Transition Energies of OHBA-C

Matrix	T_1		S_1		S_2		S_3	
	nm	cm^{-1}	nm	cm^{-1}	nm	cm^{-1}	nm	cm^{-1}
Argon	n.a.		375	26670	355	28170	256.0	38760
Xenon	n.a.		382	26180	359	27850	263.6	37940

Table IIIb. 0-0 Transition Energies of OHBA-F

Matrix	T_1		S_1		S_2		S_3	
	nm	cm^{-1}	nm	cm^{-1}	nm	cm^{-1}	nm	cm^{-1}
Argon	404.5	24720	379.0	26380	314.6	31790	251.6	39750
Xenon	405.9	24640	379.6	26340	319.8	31270	257.4	38850

* Values marked with asterisks represent crossing point between excitation and emission spectra, all others are the wavelength or frequency at half height of the leading peak in structured emission.

Figure 5. 12K UV-Vis absorption difference spectrum (0.1 nm resolution) of 0.35 mmoles of an ~1:200 OHBA-C:Ar mixture, deposited onto a BaF_2 window and then photolyzed for 10 minutes with a 1000 Watt Hg-Xe lamp through a Corning 7-60 filter (passing 320-380 nm), minus the corresponding absorption spectrum of 0.35 mmoles Ar.

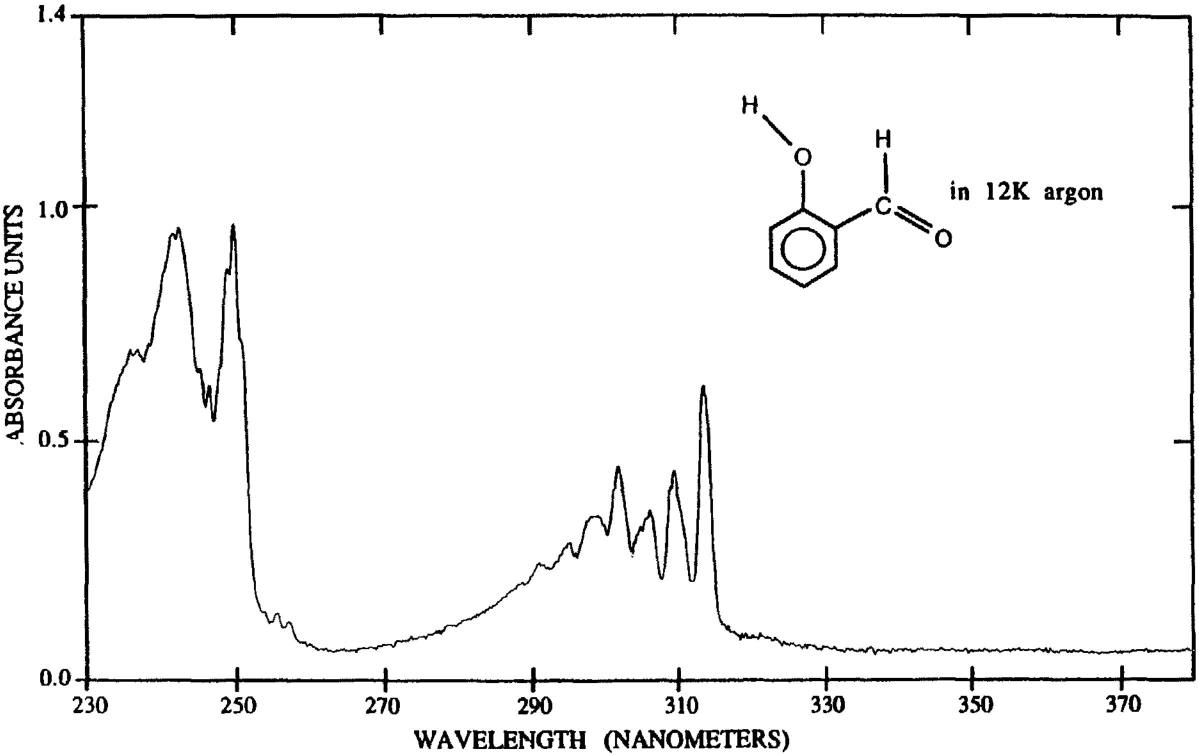
1.4
1.0
0.5
0.0
ABSORBANCE UNITS
230
250
270
290
310
330
350
370
WAVELENGTH (NANOMETERS)
H
O
H
C
O
in 12K argon

Figure 6. Excitation spectrum of OHBA-F (generated by 10 minutes photolysis with the spectrometer lamp source at 335 nm) in 12K Ar, resolution of 0.4 nm, monitoring emission at 435 nm.

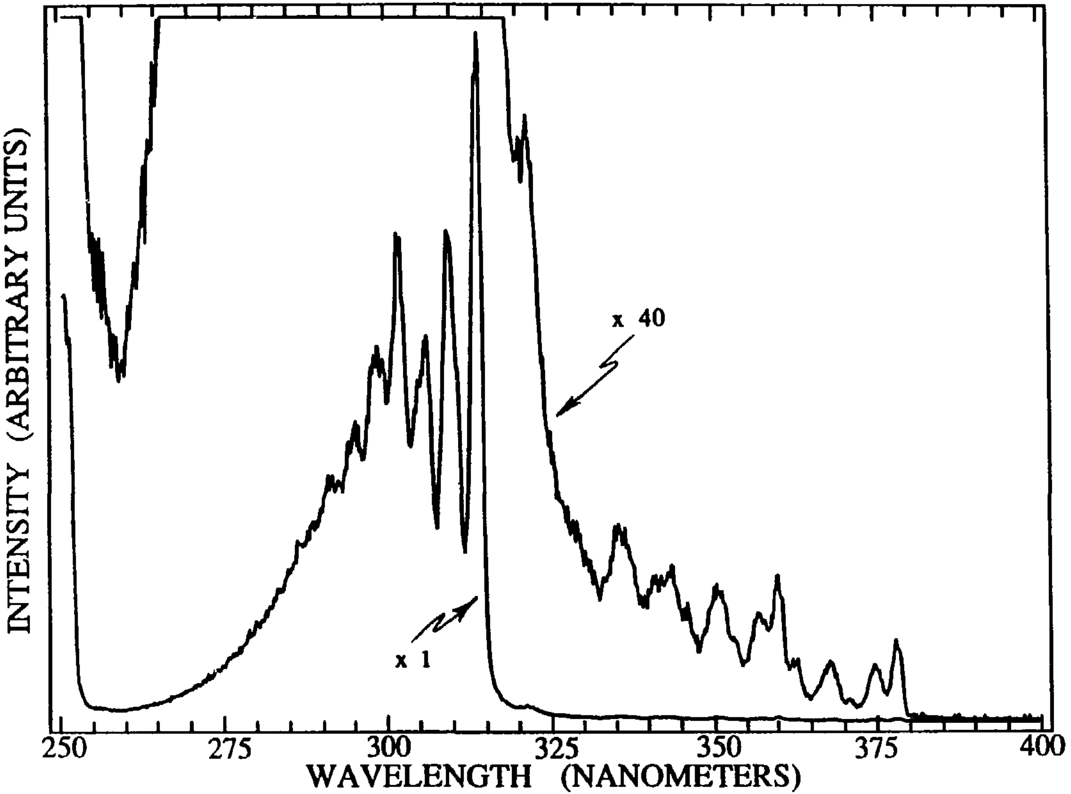
INTENSITY (ARBITRARY UNITS)
x 40
x 1
250
275
300
325
350
375
400
WAVELENGTH (NANOMETERS)

Figure 7. Emission spectrum of OHBA-F (generated by 10 minutes photolysis with the spectrometer lamp source at 335 nm) in 12K Ar, with excitation at 302 nm, 0.2 nm resolution. Peak maxima and peak-to-peak distances in wavenumbers are marked for the primary vibrational progression.

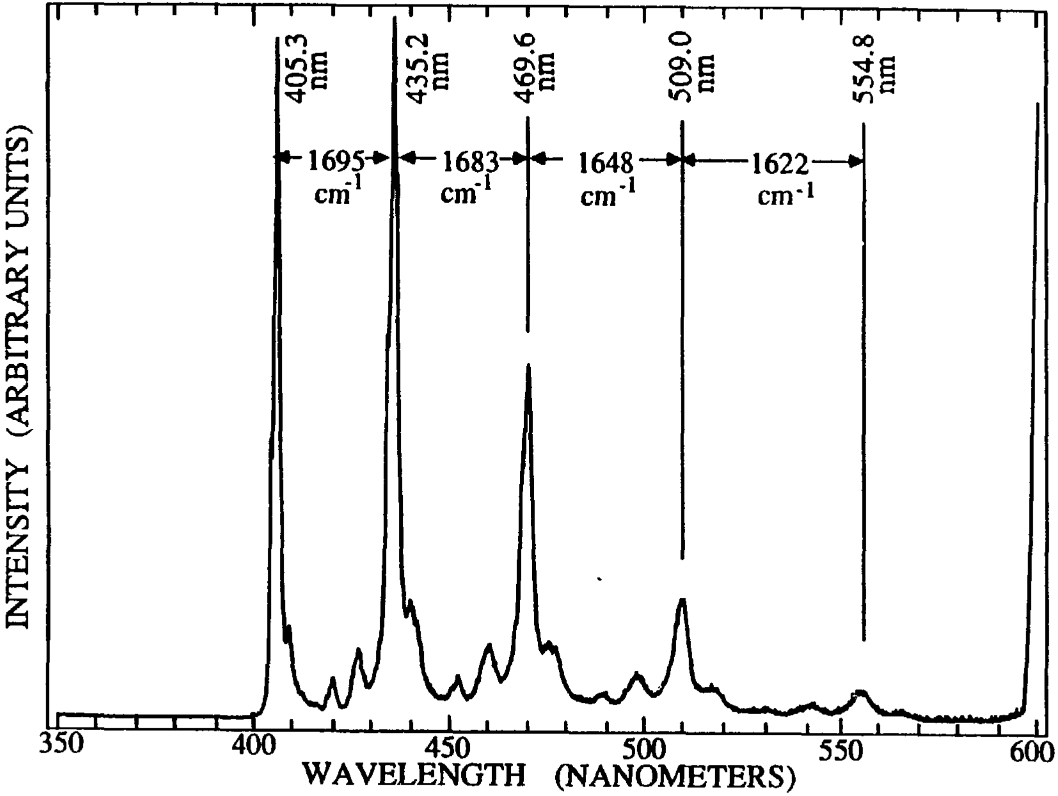
INTENSITY (ARBITRARY UNITS)
WAVELENGTH (NANOMETERS)
350
400
450
500
550
600
405.3 nm
435.2 nm
469.6 nm
509.0 nm
554.8 nm
1695 cm-1
1683 cm-1
1648 cm-1
1622 cm-1

and xenon matrices, along with those of another strong absorption band located between 220 and 250 nm, referred to as S_3 and attributable to a π,π^* transition by its intensity.

As the vibrational structure is of interest in determining chromophores and vibrational frequencies, the peak maxima, and their distance from the appropriate S_1, S_2, or T_1 0-0 peaks, are given in Table IV. A slight splitting is apparent in the 405 and 435 nm peaks of the emission spectrum, and is presumably again due to the proposed site splittings detected in the infrared spectrum.

Wavelength Dependence of the Photolysis Quantum Yield for OHBA-C and OHBA-F

The photolysis quantum yield Φ is defined as the number of excited molecules which subsequently go on to form products, per number of excited molecules. In the case of photoisomerization of OHBA-C to OHBA-F, this is then equal to the number of OHBA-F molecules formed per number of photons absorbed by OHBA-C. It has been proposed that the energy of an excited state barrier to reaction can be determined from the wavelength dependence of the photolysis quantum yield, in that the quantum yield Φ can be sensitive to a new route to reaction accessed with photolysis energies greater than that of the excited state barrier. The wavelength dependence of Φ is determined from the electronic absorption spectrum of the parent compound and the rates of disappearance of the parent compound with incident photons (of a particular wavelength) as follows.

Defining I_0 as the incident photon flux (with units of photons area^{-1} time^{-1}) and I as the transmitted photon flux, the number of photons absorbed in time t is then equal to $\Delta(I_0\text{-}I)$ if no light is scattered. Defining C as the amount of OHBA-C in the area of the photolysis beam,

Table IV. Vibrational Features in Excitation and Emission Spectra of OHBA-F in Ar

S_1 Excitation		S_2 Excitation		T_1 Emission	
nm	cm^{-1}*	nm	cm^{-1}*	nm	cm^{-1}*
377.8	0	313.6	0	(403.9)	(-85)
374.4	240	308.8	496	405.3	0
370.6	514	305.8	813	408.6	199
367.6	734	301.2	1313	419.8	852
362.4	1125	298.2	1647	426.2	1210
359.8	1324	294.8	2033	(433.5)	(1605)
356.6	1573	290.6	2524	435.2	1695
353.0	1859			439.5	1920
350.2	2086			451.7	2534
345.8	2449			459.6	2915
343.4	2651			469.6	3378
341.0	2856			475.2	3629
335.2	3364			476.6	3691
321.2	4664			488.6	4206
				497.5	4572
				509.0	5027
				516.7	5319
				541.5	6206
				554.8	6318

---

* These values represent the peak-to-peak distance in energy from the assigned 0-0 transition peak. Those values marked with parentheses are the minor component of a split peak.

$$\Phi = -\Delta C/\Delta(I_0-I). \qquad \text{(Eq. 1)}$$

$(I_0 - I)$ is not however known unless either the reaction is followed in the UV, or one has accurate knowledge of the relative UV and IR extinction coefficients. Since it is highly desirable to monitor the reaction by IR spectroscopy where there is both good separation of product and reactant absorption bands, and no chance of photolysis with the probe light, an expression for Φ in terms of the measurable quantity I_0 is needed.

Beer's Law states that

$$I = I_0\exp(-\varepsilon C) \qquad \text{(Eq. 2)}$$

Expansion of the exponential in a Taylor's series yields the relation

$$I = I_0(1 - \varepsilon C + (\varepsilon C)^2/2! + \ldots) \qquad \text{(Eq. 3)}$$

which for small εC can be approximated by

$$I \sim I_0 - I_0\varepsilon C \qquad \text{(Eq. 4)}$$

Rearrangement of Eq. 4 yields

$$I_0 - I \sim I_0\varepsilon C, \qquad \text{(Eq. 5)}$$

which upon differentiation by I_0 has the form

$$d(I_0-I)/dI_0 \sim \varepsilon C + I_0\varepsilon(dC/dI_0). \qquad \text{(Eq. 6)}$$

Assuming that only a small fraction of the incident light results in reaction, the latter term can be disregarded, such that

$$d(I_0-I)/dI_0 \sim \varepsilon C. \qquad \text{(Eq. 7)}$$

Multiplication of Eq. 1 by Eq. 7 yields

$$\Phi\varepsilon C \sim (-\Delta C/\Delta(I_0-I))(d(I_0-I)/dI_0), \qquad \text{(Eq. 8)}$$

which in the limit of small photolysis times is equivalent to the relation

$$\Phi\varepsilon C \sim -dC/dI_0. \qquad \text{(Eq. 9)}$$

$\Phi\varepsilon$ can then be treated as a first order rate constant k for optically thin samples with modest reaction quantum yields, determinable with knowledge of I_0 and C.

Precise concentration and sample thicknesses are very difficult to determine for matrices deposited by condensing a gas phase sample onto an optical window, such that C and ε are usually not known for these matrix samples. However, the wavelength dependence of ε can easily be determined from a UV absorption spectrum. Likewise, while C may not be known absolutely, it is proportional to heights and areas of IR absorption bands. Thus, the quantum yields at one wavelength relative to that at another wavelength can be obtained much more readily than can the absolute quantum yields, and serve the purpose of mapping out excited state barriers well.

For a simple non-reversible reaction, the quantum yield at one photolysis wavelength λ_1 relative to the quantum yield at another wavelength λ_2, Φ_1/Φ_2, is then $(k_1/\varepsilon_1)/(k_2/\varepsilon_2)$ with the above approximations. The rate constants $k(\lambda)$ are evaluated from the first order decays $\alpha H = \alpha H_0 \exp(-kI_0)$ at the two different wavelengths, where α is a proportionality constant relating a chosen IR absorption H (in this case, the 1673 cm^{-1} carbonyl stretch peak height), to C, the actual number density of OHBA-C in the photolysis beam path.

The approximation in the Taylor expansion has an inherent error of 20% at .20 absorbance in the customary base ten units. Thus, either the absorption of the sample must be known at all times, or the sample must be optically thin at the wavelength of photolysis. Due to the large absorption coefficient of the carbonyl stretch motion of OHBA-C (see Figure 1), the relatively low UV extinction coefficient of OHBA-C (the extinction coefficient of OHBA-C in decane is ~3600 $M^{-1}cm^{-1}$ at 330 nm), and the high sensitivity of the FTIR technique, it was generally possible to keep optical densities at less than 0.1 at the wavelength of photolysis. Errors from the approximation that $I_0(dC/dI_0)$ is small relative to C are less easily quantified, but have the effect of elevating the calculated relative quantum yield at wavelengths where the absolute quantum yield is high. One can correct for the fraction of incident light scattered by comparing the light attenuation in a sample matrix to a similarly deposited matrix of the pure host material.

This method of determining the wavelength dependence of reaction quantum yields is somewhat more complicated for a reversible reaction, in that dC/dI_0 is in this case proportional to $(-k_fC + k_rF)$, and $C-C_{ss} = (C_0-C_{ss})\exp(-(k_f+k_r)I_0)$, where F is the amount of the non-hydrogen-bonded form (proportional to the height of the 1701 cm^{-1} carbonyl stretch absorption), C_{ss} is the amount of starting material at steady state, and k_f and k_r are the rate constants for the forward and reverse reactions, respectively. k_f can however be obtained by evaluating dC/dI_0 at the start of photolysis, when F is equal to zero.

Figure 8 is a plot of the diminishing height of the 1673 cm^{-1} parent absorption with incident micromoles of 320 nm photons, along with the best single exponential fit. With the approximations that the deposition area is four times the 1" photolysis area, the UV absorbance of this .05 mmole sample is 0.10 at the photolysis wavelength, and the concentration of the matrix is the 460:1 Ar:OHBA calculated from the vapor pressures, the absolute quantum yield calculated from this exponential curve is 0.17. While this value could be low or high by factors of three or more, it provides an indication that this reaction is indeed quite facile.

Photolysis curves such as that of Figure 8 were generated at a number of different wavelengths throughout the absorption region of OHBA-C, and the corresponding values for k_f evaluated. The rate constants derived from the zero-time slopes measured at the various photolysis wavelengths $(k_f(\lambda))$,

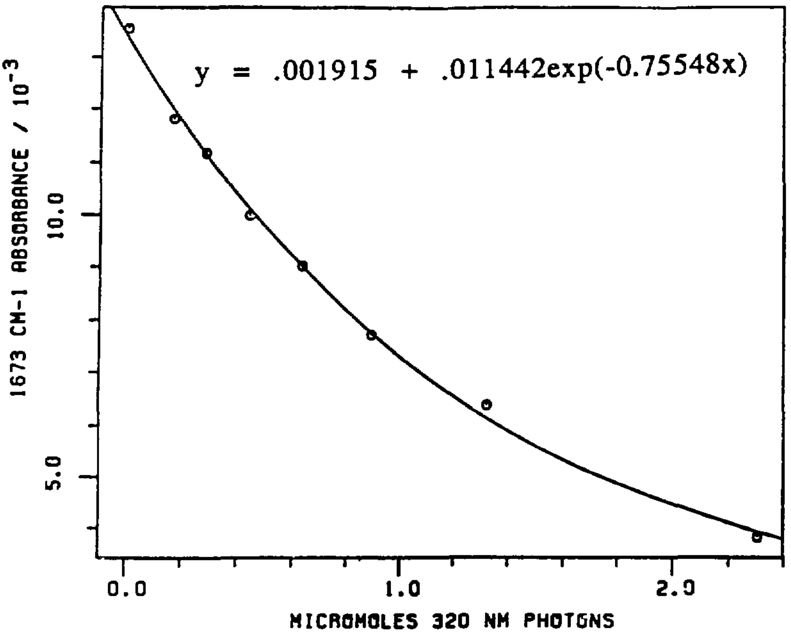

Figure 8. Sample photolysis curve, showing diminution of 1673 cm^{-1} peak height of OHBA-C with incident micromoles of 320 nm photons. Also shown is the best single exponential fit. Sample consisted of 0.05 mmole ~460:1 Ar:OHBA mixture deposited onto 12K CsI substrate.

the absorbances from Figure 3, and the resulting quantum yields relative to that measured at 320 nm are given in Table V. These data are represented by the solid triangles in Figure 9, which is a plot of $(k_{f(\lambda)}/\varepsilon_{C(\lambda)})/(k_{f320nm}/\varepsilon_{C(320nm)})$, and shows that the quantum yield appears to be independent of wavelength up to about 310 nm, 5590 cm^{-1} above the S_1 0-0 energy, with a 23% increase in the quantum yield detectable by 295 nm, 7230 cm^{-1} above the S_1 0-0 energy and a 112% increase detectable by 285 nm, 8420 cm^{-1} above the S_1 0-0 energy.

Included in Table V are uncertainties in the values for k_f and the absorbance in Figure 3. The uncertainty in k_f is estimated to be approximately ± 6%, based on the reproducibility at 325 nm (these two experiments were completed several days apart, with extensive use of the laser and realignment of the beam in between) and the deviation in the values for the relative quantum yields between 300 and 325 nm. The uncertainty in the absorbance in Figure 3 is estimated to be ± .005 at the shorter wavelengths, a result of both noise and a low amplitude interference fringe detectable in the visible region.

Values for $(\varepsilon_{C(\lambda)})/(\varepsilon_{(320nm)})$ were evaluated from a hand-smoothed, expanded version of Figure 3, and thus include the assumption that the argon matrix scattering can be compensated for by subtracting from the OHBA in argon absorption spectrum the "absorption" of a similarly deposited sample of pure argon. Lower error bars in Figure 9 were calculated using a difference absorption spectrum of OHBA-C in argon minus a bare window spectrum. Thus, these lower values reflect an assumption that all the light attenuation of a matrix of OHBA-C in argon is from absorption by the OHBA-C. This leads to larger values for the extinction coefficients, and hence smaller values for $(k_{f(\lambda)}/\varepsilon_{C(\lambda)})/(k_{f(320nm)}/\varepsilon_{C(320nm)})$, with a proportionately greater

Table V. Wavelength Dependence of Reaction Quantum Yield: OHBA-C → OHBA-F

$\lambda_{photolysis}$ (nm)	k_f (μmole photons)$^{-1}$	$A_{Figure\ 3}$	k_f/A	$(k_f/A)/(k_{f320}/A_{320})$
285.0	.120 ± .007*	.021 ± .005	5.71	2.12 ± .6
290.0	.169 ± .01	.039 ± .005	4.33	1.61 ± .3
295.0	.209 ± .01	.063 ± .005	3.32	1.23 ± .2
300.0	.243 ± .01	.090 ± .005	2.70	1.00 ± .1
305.0	.349 ± .02	.125 ± .005	2.79	1.04 ± .1
314.0	.544 ± .03	.196 ± .005	2.77	1.03 ± .09
320.0	.646 ± .04	.233 ± .005	2.69	(1.00)
325.0	.685 ± .04	.253 ± .005	2.71	1.01 ± .08
325.0	.632 ± .04	.253 ± .005	2.50	0.92 ± .07
366.9	.0035 ± .0002	.0015 ± .001	2.33	0.87 ± .06

* ± 6% of the k_f value

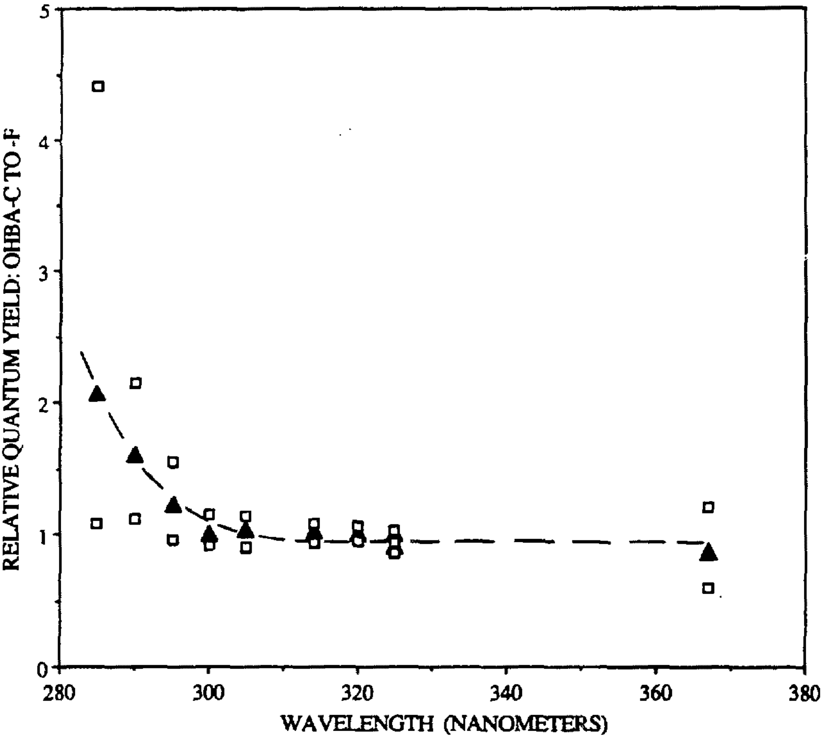

Figure 9. Plot of $(k_{f(\lambda)}/\varepsilon_{C(\lambda)})/(k_{f(320nm)}/\varepsilon_{C(320nm)})$ versus wavelength for the photolysis of OHBA-C to OHBA-F in argon matrix, yielding the wavelength dependence of the quantum yield for this reaction. The values indicated by solid triangles were calculated with a correction for scattering of the argon matrix as noted in the text. Also included are upper and lower bounds (open squares) at each photolysis wavelength obtained by substituting the lower and upper bounds for the UV absorbance coefficient, as discussed in the text.

effect at the shorter wavelengths where the extinction coefficients are smaller.

The upper bounds in Figure 9 were obtained by assuming that the contribution of scattering to the relative extinction coefficients obtained from Figure 3 is not fully accounted for by the subtraction of a matrix spectrum of argon, but rather that the guest molecule also introduces imperfections to the matrix which increase scattering, and furthermore, that the guest molecule scatters light itself. Thus, the baseline for these upper bounds was taken as a straight line drawn between the absorbance at 270 nm and at 375 nm in Figure 3. The UV spectrum of 12K Ar served to ensure that the straight line approximation was valid over this wavelength region. The additional assumption was made that the apparent rate constants are decreased in proportion to the fraction of light which is scattered, and that this fraction can be determined by comparison of the attenuation of the pure argon matrix to the amount of attenuation attributable to the absorption of OHBA-C in Figure 3 (with the 270-375 nm straight line baseline). Assignment of the higher baseline and consideration of the percentage of incident light available for absorption have the effect of increasing the calculated relative quantum yields at the shorter wavelengths.

The wavelength dependence of the quantum yield for the reverse reaction of generating OHBA-C from OHBA-F can be determined in a similar manner. This has been done for a few wavelengths by photolyzing OHBA-C in argon with 325 nm laser light or with the 1000 W Hg-Xe lamp to give >97% OHBA-F. The photolysis of OHBA-F was then followed by monitoring the disappearance of its 1701 cm^{-1} carbonyl stretch peak. Values for the measured rate constants and the absorbances are given in Table VI, along with the quantum yield obtained by division of these two numbers.

Table VI. Wavelength Dependence of Reaction Quantum Yield:
OHBA-F → OHBA-C

$\lambda_{photolysis}$ (nm)	k_r (μmole photons)$^{-1}$	$A_{Figure\ 5}$	k_r/A	$(k_r/A)/(k_{r313.6}/A_{313.6})$
285.0	.141	.120	1.17	1.62
309.4	.217	.389	.558	.773
313.6	.411	.569	.722	(1.00)
314.0	.304	.548	.555	.768
377.8	.000919	.00148#	.621#	.859#

\# This absorbance value was obtained by comparison of the excitation intensities at 377.8 and 295.0 nm in Figure 6 with the absorption at 295.0 nm in Figure 5.

Absorbances were obtained from the absorption spectrum of Figure 5, with the exception of the absorbance of the 377.8 nm S_1 0-0 peak, for which the value was determined by comparing the phosphorescence excitation peak heights at that wavelength and at 295 nm in Figure 6 to the absorption at 295 nm in Figure 5. The quantum yields are normalized to that at 313.6 nm, and are plotted in Figure 10 as a function of wavelength, showing an apparent increase in the quantum yield at the shorter wavelengths.

Relative Quantum Yields - Forward and Reverse Reactions

It is of course desirable to know also the quantum yield for the forward reaction at a particular wavelength relative to that for the reverse reaction at the same wavelength. These values can be obtained from the amounts of OHBA-F and OHBA-C at steady state. Given that

$$\frac{dC}{dI_0} = \frac{-\Phi_{C\rightarrow F}(I_0-I)\,\varepsilon_C\,C}{\varepsilon_C\,C+\varepsilon_F\,F} + \frac{\Phi_{F\rightarrow C}\,(I_0-I)\cdot\varepsilon_F F}{\varepsilon_C\,C+\varepsilon_F F}$$

is equal to zero at steady state, the ratio $\Phi_{C\rightarrow F}/\Phi_{F\rightarrow C}$ is obtained as $\varepsilon_F F/\varepsilon_C C$ at steady state, where F/C is the ratio of the steady state populations of OHBA-F and OHBA-C.

The ratios of the forward and reverse reaction quantum yields in argon matrix are given in Table VIIa as a function of wavelength. The relative steady state populations were obtained from the areas or peak heights of the 1701 and 1673 cm^{-1} carbonyl stretch peaks, times a conversion factor obtained from difference spectra at somewhat shorter photolysis times. This conversion factor, which is the ratio of the extinction coefficients for the two IR peaks, is 1.63 by area, and ranged from 2.28 to 2.79 by height depending on the wavelength of photolysis (due to the site splitting), with OHBA-F having the larger extinction coefficient, in both height and area. It is usually best to determine infrared absorptions from

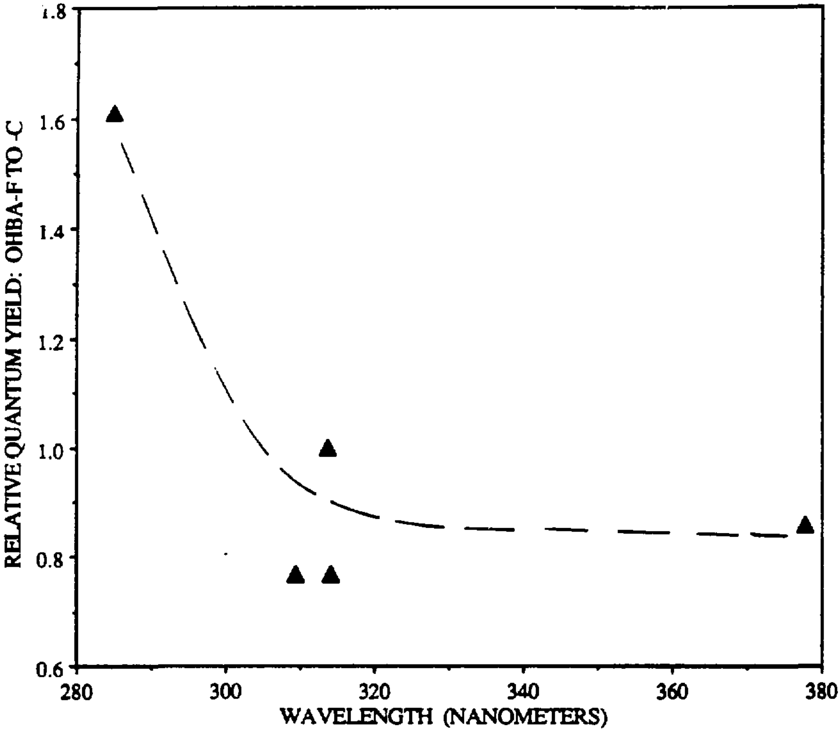

Figure 10. Plot of $(k_{r(\lambda)}/\varepsilon_{F(\lambda)})/(k_{r(313.6nm)}/\varepsilon_{F(313.6nm)}$ versus wavelength for the photolysis of OHBA-F to OHBA-C in argon matrix, yielding the wavelength dependence of the quantum yield for this reaction.

Table VIIa. Ratio of Reaction Quantum Yield:
OHBA-C→OHBA-F/OHBA-F→OHBA-C in Argon

Wavelength (nanometers)	F_{ss}/C_{ss}	A_F/A_C	$F_{ss}\varepsilon_F/C_{ss}\varepsilon_C$ (Φ ratio)	Method, Conversion Factor Used
280.0	1.35	.067/.0115	7.86 ± 4*	Area, 1.63
280.0	1.41	.067/.0115	8.19 ± 4	Area, 1.63
280.0	1.20	.067/.0115	7.00 ± 4	Height, 2.48
285.0	1.38	.120/.021	7.91 ± 2	Area, 1.63
285.0	1.19	.120/.021	6.79 ± 2	Height, 2.41
287.0	1.30	.135/.029	6.05 ± 1	Area, 1.63
289.0	1.35	.152/.035	5.86 ± 1	Area, 1.63
290.0	1.27	.170/.039	5.54 ± .9	Height, 2.28
291.0	1.16	.194/.044	5.12 ± .7	Area, 1.63
291.0	1.34	.194/.044	5.93 ± .8	Area, 1.63
291.0	1.44	.194/.044	6.33 ± .8	Area, 1.63
293.0	1.39	.188/.052	5.05 ± .7	Area, 1.63
295.0	1.45	.235/.063	5.42 ± .5	Area, 1.63
297.0	1.66	.245/.074	5.53 ± .5	Area, 1.63
300.0	2.06	.270/.090	6.18 ± .4	Height, 2.62
305.0	2.44	.271/.125	5.30 ± .3	Height, 2.57
309.0	2.01	.358/.151	4.76 ± .2	Area, 1.63
309.0	2.01	.358/.151	4.76 ± .2	Area, 1.63
314.0	1.98	.548/.196	5.54 ± .2	Area, 1.63
314.0	1.98	.548/.196	5.55 ± .2	Height, 2.79

* These uncertainties are obtained by consideration of the ±.05 uncertainty in the absorbance values only.

Table VIIb. Ratio of Reaction Quantum Yield:
OHBA-C→OHBA-F/OHBA-F→OHBA-C in Xenon

Wavelength (nanometers)	F_{ss}/C_{ss}	A_F/A_C	$F_{ss}\varepsilon_F/C_{ss}\varepsilon_C$ (Φ ratio)	Method, Conversion Factor Used
285.0	.815	.044/.009	5.34 ± 3#	Height, 3.22
292.0	1.82	.097/.021	6.02 ± 1	Height, 3.22
296.0	1.43	.125/.034	5.23 ± .8	Height, 3.22
310.7	2.32	.208/.097	4.98 ± .3	Height, 3.22
318.7	1.87	.377/.145	4.86 ± .2	Height, 3.22

These uncertainties were obtained by consideration of an estimated ±.04 uncertainty in the absorbance values only.

areas, so as to avoid the problems of site splittings and/or annealing. However, it is difficult to accurately determine a baseline over the longer frequency ranges necessary for determining peak areas for samples where the amplitude of the interference fringe (the spacing of which was on the order of 100 cm^{-1}) is larger relative to the peak heights. Therefore, population ratios in the thinner samples were determined from peak heights. The ratios $\varepsilon_F/\varepsilon_C$ at the different wavelengths were obtained from the absorbances in the two UV spectra of Figures 3 and 5, which are spectra of the same matrix before and after photolysis with the 7-60 filtered Hg-Xe lamp. The uncertainty in the quantum yield ratios stemming from consideration of the .005 unit uncertainty in the absorbances is also given in Table VII.

Figure 11 is a graph of these quantum yield ratios, showing that at the longer wavelengths the quantum yield for the forward reaction is about five times that for the reverse process, whereas at wavelengths shorter than about 300 nm the forward reaction begins to dominate even more, although the increase in the ratio is within the limits of the absorbance-imposed uncertainties. The dashed line represents an average for these ratios, and places the discontinuity at about 293 nm, a somewhat shorter wavelength than that obtained for the wavelength dependence of the forward reaction's quantum yield.

Ratios of the forward reaction quantum yield to the reverse reaction quantum yield should be independent of whether they are determined from zero-time photolysis slopes or from steady state populations. Because the absorption coefficients used for determining the relative quantum yields from the zero-time slopes in the two directions are from the same matrix, division of the k_f/A values in Table V by the k_r/A values in Table VI yields

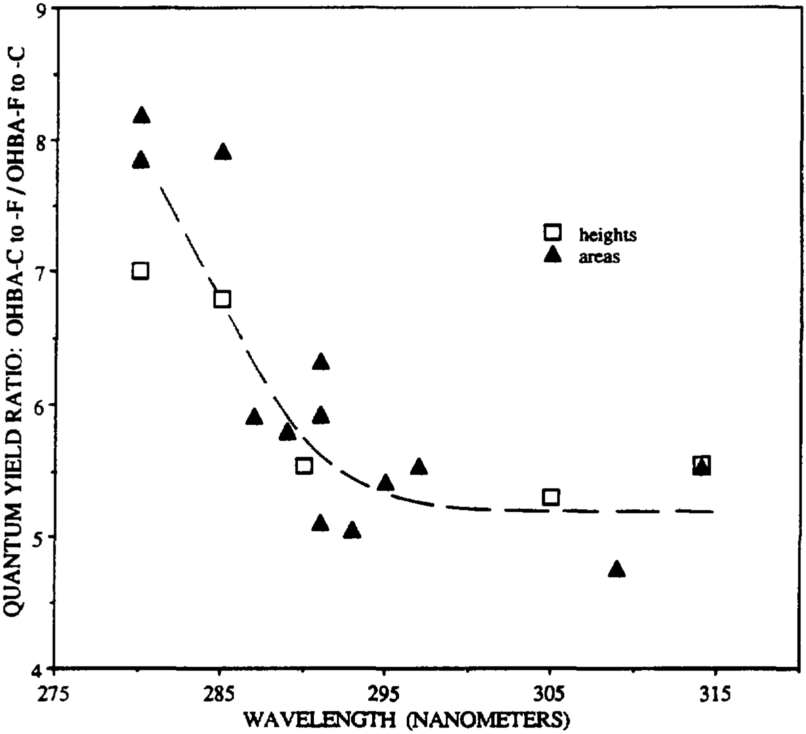

Figure 11. Plot of $\varepsilon_F F/\varepsilon_C C$ versus wavelength for the steady-state populations of OHBA-C and OHBA-F after photolysis at these wavelengths in argon matrices, yielding the quantum yield ratio for the reactions OHBA-C→ OHBA-F / OHBA-F→OHBA-C as a function of wavelength.

the ratios of the quantum yields for the forward and reverse reactions. The ratio determined in this manner at 314 nm (5.0) agrees well with that determined from the steady state values (5.5). The same calculation at 285 nm yields 4.9 as the ratio from the zero-time slope rate constants, while that obtained from the steady state populations is significantly greater at 7.3 ± 0.6. The discrepancy at the shorter wavelength is perhaps an indication that the true curve shape of the wavelength dependence of the quantum yield for the photolysis of OHBA-C to OHBA-F may lie closer to the upper bounds in Figure 9 rather than to the lower bounds.

The equivalent study of the relative quantum yields for the forward and reverse reactions in xenon matrices (Table VIIb) produced essentially the same factor of five ratio obtained at the longer wavelengths in argon, as shown in Figure 12. Due to the manner in which the steady state populations were obtained, these results rely on a value for the ratios of the carbonyl stretch IR extinction (by height) coefficients obtained upon photolysis at 318.7 nm.

ΔH for the Reaction OHBA-C → OHBA-F

Figure 13 is a UV absorption spectrum of 2.75 x 10^{-4} M (22°C) OHBA in n-decane at 20.2, 68.2, and 96.5°C, corrected for the change in density with temperature by the 216 nm absorption of n-decane at those temperatures. There is a slight change in the wavelength of maximum absorption with temperature, the peak occurring at shorter wavelengths at higher temperatures as overall intensity is lost from the OHBA-C dominated region between 300 and 355 nm and is gained in the region where OHBA-F strongly absorbs (290-315 nm, see Figures 3 and 5). The exception is at very long wavelengths, between 355 and 380 nm, where the the higher temperature solutions have greater absorption, presumably due to population of higher

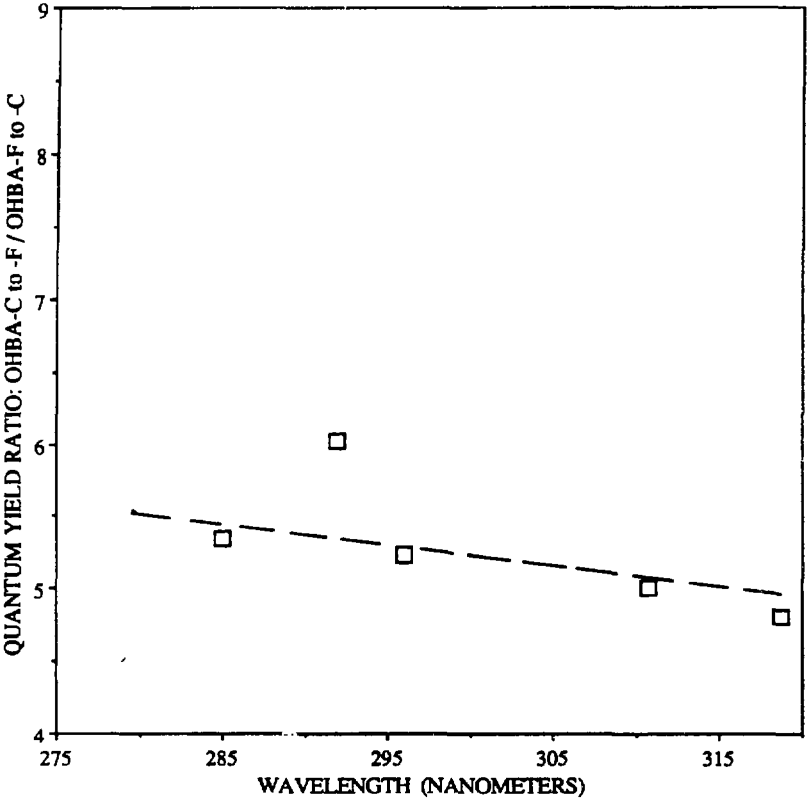

Figure 12. Plot of $\varepsilon_F F/\varepsilon_C C$ versus wavelength for the steady-state populations of OHBA-C and OHBA-F after extended photolysis in xenon matrices, yielding the quantum yield ratio for the reactions OHBA-C→OHBA-F / OHBA-F→OHBA-C as a function of wavelength.

Figure 13. UV absorption of OHBA in n-decane at 293.3 and 369.6K, corrected for the change in density with temperature such that both spectra correspond to concentrations of 6.9×10^{-3} M, assuming Beer's law behavior.

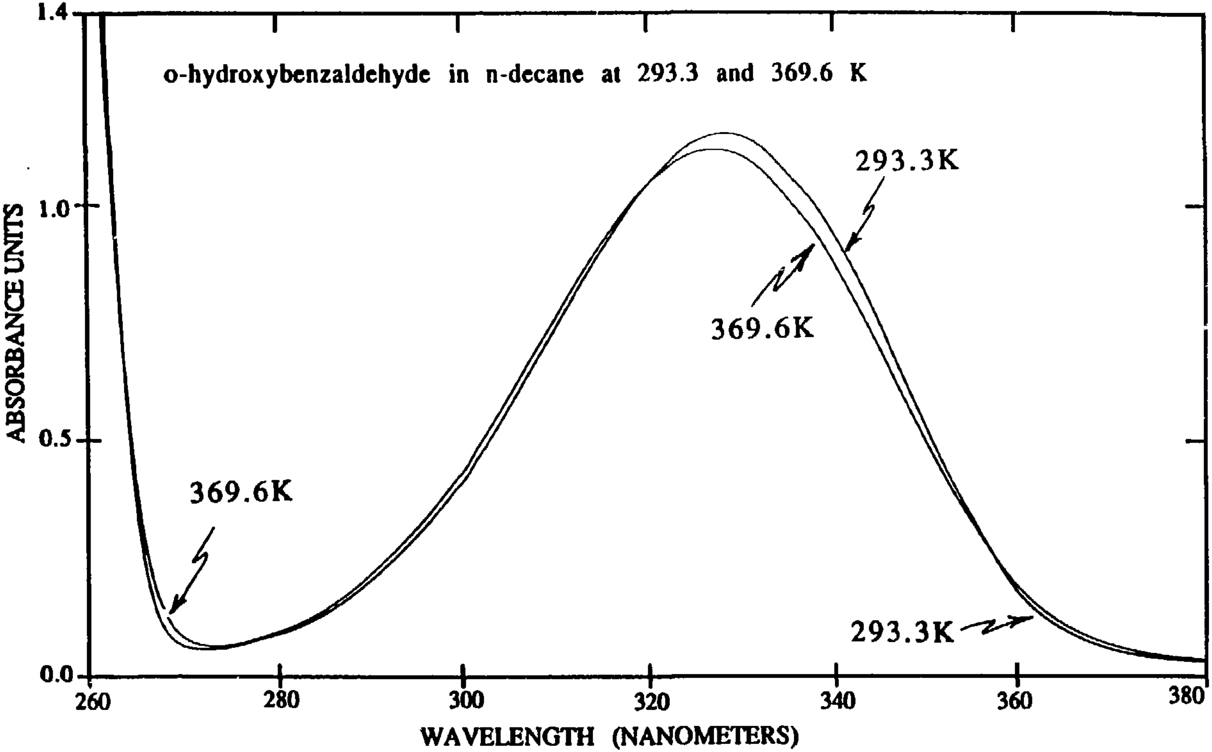
o-hydroxybenzaldehyde in n-decane at 293.3 and 369.6 K
293.3K
369.6K
369.6K
293.3K
ABSORBANCE UNITS
1.4
1.0
0.5
0.0
260
280
300
320
340
360
380
WAVELENGTH (NANOMETERS)

vibrational levels in the ground state.

If one assumes that the loss of intensity in the region between 320 and 350 nm is entirely due to conversion of OHBA-C to OHBA-F, one can calculate equilibrium constants, and thus enthalpies and entropies of reaction. 340 nm was chosen as the wavelength to evaluate the loss of OHBA-C, since it is midway between the far red edge and the region where OHBA-F would start to absorb strongly. Assuming that the population of OHBA-F at 20.2 degrees is zero, any loss in intensity at 340 nm is due to the formation of OHBA-F, such that the equilibrium constant K is equal to $(1-A_T/A_{20.2})/(A_T/A_{20.2})$, where A_T and $A_{20.2}$ refer to the density corrected 340 nm absorption at the higher temperature and 20.2°C, respectively. A plot 1/T vs lnK yielded a ΔH value of 5.75 kcal/mole and a ΔS value of 10.37 e.u.. However, these values imply a population at 20.2°C of .96% OHBA-F. Iteration until the equilibrium value calculated from ΔH and ΔS coincided with that assumed in determining those values resulted in a calculated enthalpy change of 3.0 kcal mole^{-1} and an entropy difference of 3.9 e.u., which corresponds to a ΔG value of 1.85 kcal/mole and a 4.0% population of OHBA-F at 20.2°C. This calculation was somewhat sensitive to the wavelength chosen to evaluate the change in absorbance, in that the equivalent iterative process at 350 nm yielded a ΔH value of 2.4 kcal mole^{-1}, a ΔS value of 2.5 e.u, and a ΔG value of 1.65 kcal/mole at 20.2°C.

METHYL SALICYLATE

Ground States of Methyl Salicylate

Figure 14 is an FTIR difference spectrum of methyl salicylate (negative features) and its photolysis product (positive features) in xenon matrix after photolysis at 325 nm. Frequencies of these absorptions are

Figure 14. FTIR difference spectrum of MS-C (negative features) and its photolysis product (positive features) in 12K xenon matrix after 2.5 hours photolysis with 6 mWatt 325 nm light. The frequencies of the carbonyl and OH stretch absorptions are noted.

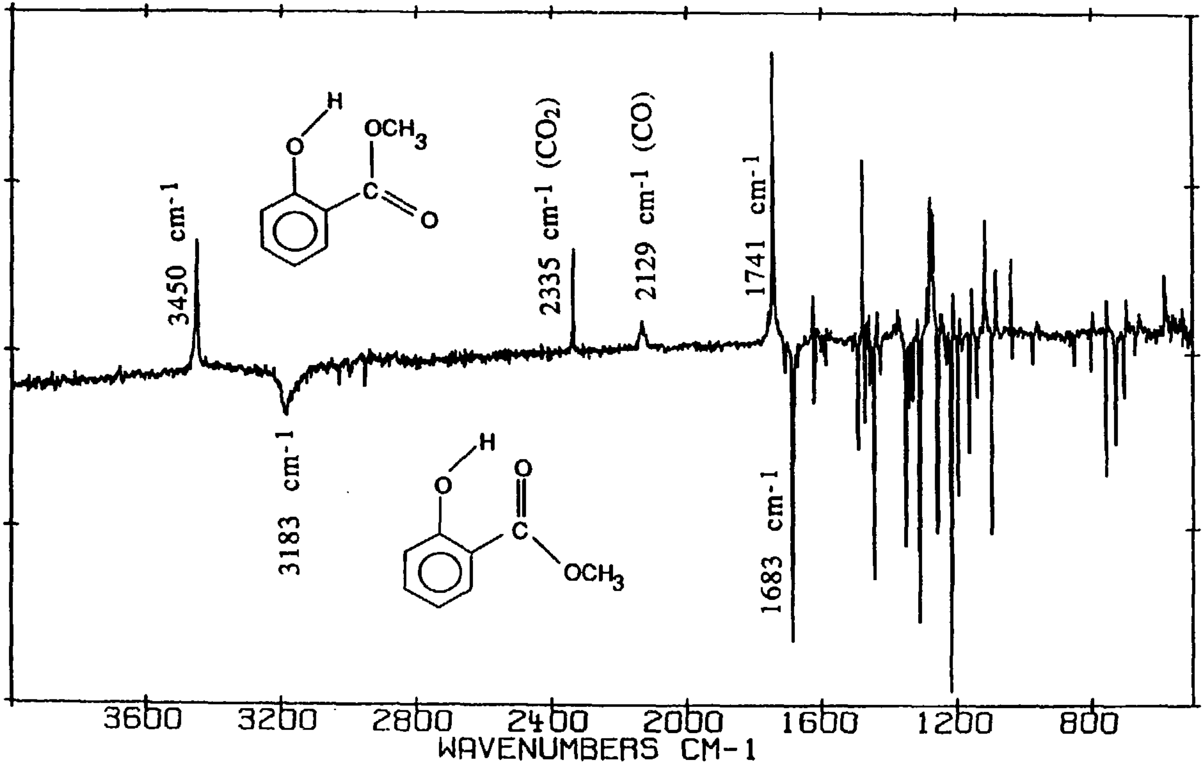
3450 cm-1
3183 cm-1
2335 cm-1 (CO2)
2129 cm-1 (CO)
1741 cm-1
1683 cm-1
OCH3
H
O
C
O
3600
3200
2800
2400
2000
1600
1200
800
WAVENUMBERS CM-1

given in Table VIII, along with approximate relative intensities. Indicated on Figure 14 are the carbonyl stretch frequencies of the starting material (1683 cm^{-1}) and the product (1741 cm^{-1}), along with those of the O-H stretch motions at 3183 cm^{-1} and 3450 cm^{-1}, respectively. The identity of the O-H stretch absorbances were confirmed by deuteration of the phenolic proton, which shifted the bands to 2377 and 2554 cm^{-1}, a difference of factors of 1.34 and 1.35, respectively. Identification of the photolysis product as MS-E is based on the relatively low O-H stretch frequency for the product, which, unlike OHBA-F, is significantly shifted from the 3630 cm^{-1} absorption of free phenol, implying that there is a weaker hydrogen bond still present. While MS-E has previously been proposed as the UV fluorescent form of methyl salicylate, based on an ~3450 cm^{-1} shoulder detected in liquid film IR spectra[18], Figure 14 and Table VIII present the first complete vibrational spectrum of this species.

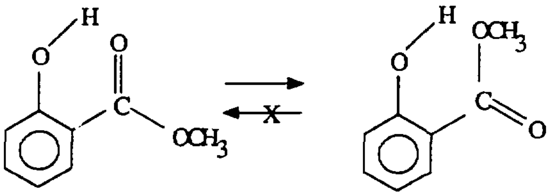

MS-C **MS-E**

UV Absorption and Emission Spectra of MS-C

The UV absorption of MS-C in xenon (Figure 15) has much more structure than that of OHBA-C. Wavelengths of these vibrational features are given in Table IXa. Such vibrational features have been observed before in neon matrix[19], along with a very low intensity feature, identified as the 0-0 transition, located at 333.7 nm, 708 cm^{-1} from the first reasonably

Table VIII. Infrared Absorptions (cm^{-1}) of MS-C and It's Photoproduct MS-E in 12K Xe Matrix

MS-C	rel. int.	MS-E	rel. int.
3183.1	vs	3450.5	vs
1705.0	w	1754.4	w
1682.8	vs	1741.4	vs
1668.3	sh,w	1736.3	sh,m
1620.1	m	1623.3	m
1615.8	m	1477.1	s
1599.9	sh,vw	1461.5	vw
1594.3	w	1457.0	w
1590.0	sh,vw	1382.4	sh,vw
1584.4	m	1379.3	w
1505.8	m	1372.3	w
1489.9	m	1365.0	w
1482.2	m	1313.9	sh,vw
1469.2	m	1284.5	m
1455.4	w	1276.8	m
1450.4	sh,vw	1270.5	d,m
1441.7	vs	1268.0	
1433.3	sh,w	1246.4	sh,w
1422.4	w	1209.5	sh,m
1346.7	s	1188.6	sh,vw
1336.2	m	1156.3?	sh,w
1326.5	m	1152.9	m
1307.2	vs	1113.4	s
1255.8	d,s	1080.3	m
1254.1		1035.5	m
1229.1	w	961.2	vw
1215.1	d,vs	864.3	sh,vw
1211.9		797.3	w
1193.9	m	755.8?	m
1182.3	m	694.8	w
1161.3	m	580.3	m
1156.3?	sh,w	528.4	w
1137.7	w		
1131.4	vw		
1092.6	m		
1030.9	w		
971.4	w		
862.4	vw		
850.8	w		
800.7	w		
755.8	s		
726.4	m		
701.3	m		
668.5	vw		
525.8	vw		

Figure 15. 12K UV absorption spectrum of MS-C in xenon, 0.6 mmoles of an ~1:700 MS-C:Xe matrix, resolution 0.2 nm. **Insert:** Spectrum of MS-C in 4.2K neon, showing low intensity long wavelength features (from ref.[19])

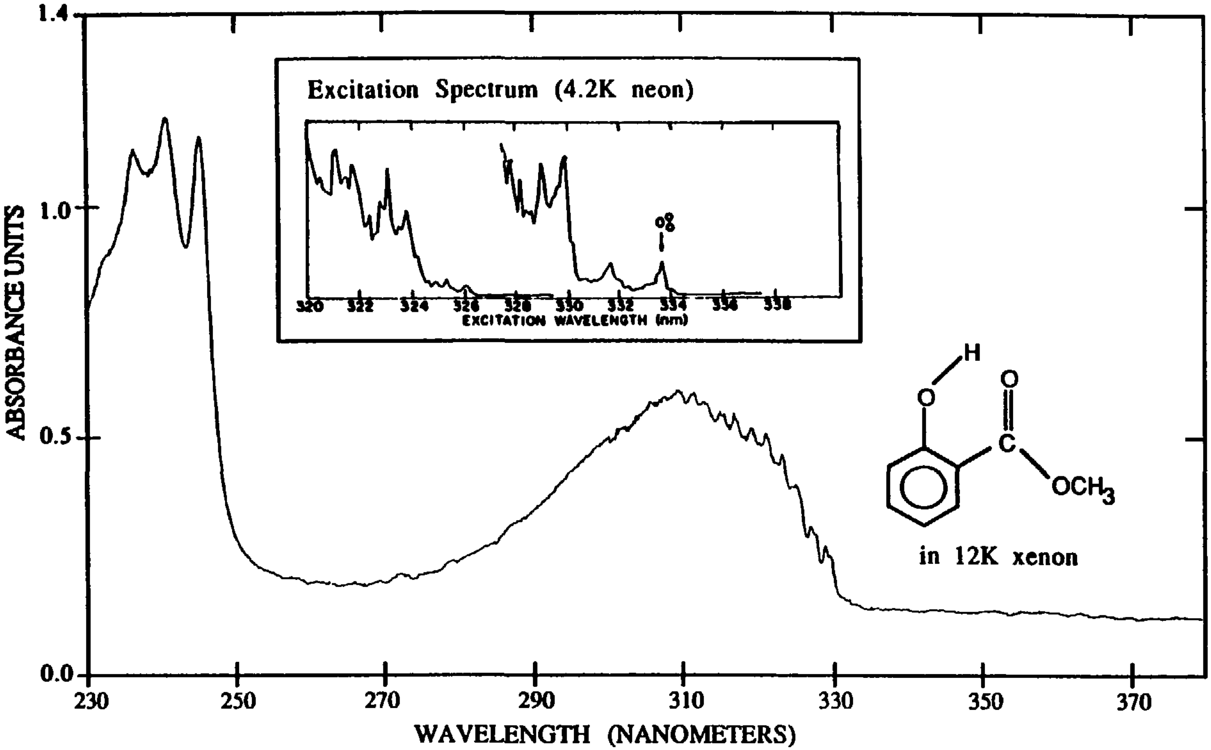
Excitation Spectrum (4.2K neon)
320
322
324
326
328
330
332
334
336
338
EXCITATION WAVELENGTH (nm)
0-0
in 12K xenon
H
O
O
C
OCH3
1.4
1.0
0.5
0.0
ABSORBANCE UNITS
230
250
270
290
310
330
350
370
WAVELENGTH (NANOMETERS)

Table IXa. Vibrational Features in Singlet Absorption (Xenon Matrix) and Emission (SF_6 Matrix) of MS-C

Absorption		Emission	
nm	cm^{-1}*	nm	cm^{-1}*
(336.7)#	0	(332)	0
329.6	640	414.5	5995
328.9	704.3	424.0	6535
326.9	890	428.5	6783
323.2	1240	437.5	7263
321.1	1443	454.5	8118
319.2	1628	464.5	8592
316.8	1856		
314.9	2056		
312.7	2279		
311.3	2423		
309.1	2652		

Table IXb. Vibrational Features in Fluorescence Excitation and Emission of MS-E in SF_6 Matrix and Phosphorescence in Xe Matrix

Fluorescence Excitation		Fluorescence Emission		Phosphorescence	
nm	cm^{-1}*	nm	cm^{-1}*	nm	cm^{-1}*
311.4	0	312.0	0	371.0	0
		313.8	184	379.0	784
308.2	333	315.4	345	383.0	1327
306.8	481	317.4	545	389.5	1590
304.8	695			395.0	1638
303.8	803	320.2	821	403.0	2140
299.2	1309	325.2	1301	408.0	2444
296.6	1602	328.2	1582	416.0	2916
		339.0	2553	421.5	3229
				437.0	4071
				470.0	5678

* These values represent the peak-to-peak distance in energy from the assigned 0-0 transition peak.

\# This value is obtained by comparison of the absorption spectrum in xenon with that reported in neon matrix[19], and the 0-0 energy obtained from the overlap of absorption and emission spectra in xenon matrix, assuming that the 328.9 nm feature in the absorption spectrum is equivalent to the first major feature in the neon absorption spectrum.

intense transition at 326.0 nm (see Figure 15 inset). Such a long wavelength low intensity band is not easily discerned in Figure 15, but the 0-0 transition in xenon, as identified by the crossing point of the excitation and emission spectra in that matrix, is located at 337 nm, 731 cm^{-1} from the first intense peak of the absorption spectrum. Thus, the 0-0 peak has been assigned at 336.7 nm in xenon, 708 cm^{-1} to the red of the first observable feature at 328.9 nm in Figure 15. Peak-to-peak distances of the vibrational features in Figure 15 from this assigned 0-0 are given in Table IX. Some caution must be taken in interpreting vibrational spacings based on this assignment though, as the relative intensities of the neon matrix spectrum suggest that the 323.8 nm feature in that matrix could also reasonably correspond to the 329.6 nm feature in xenon, shifting the 0-0 transition in xenon to 339.8 nm. This value is however somewhat in conflict with that determined from the (albeit lower resolution of 1 nm) excitation and emission spectra of MS-C in xenon.

These vibrational features are not detectable in the excitation spectrum of MS-C in SF_6 (Figure 16, Curve A) at the resolution of 1 nanometer, although the emission spectrum pictured in Figure 16, Curve B does have a little structure, tabulated in Table IXa. The emission of MS-C consists mainly of fluorescence, with a measured lifetime of 11.0 ± 1.5 nsec in SF_6, 10.5 ± 1.5 nsec in argon, and 3.0 ± 1.0 nsec in xenon. The lifetimes measured for MS-C have such large associated uncertainties because fitting of the decay curves required at least two and usually three components, with the middle and major component accounting for at most 92% of the fitted decay curve. As matrices for the nanosecond lifetimes were from mixtures with an M:R of 800:1, the short and long-lived components were probably not a result of multimers, but rather reflect different sites, the increased importance of scattering and impurities with lower emission quantum

Figure 16. Curve A: 12K excitation spectrum of MS-C in SF_6, monitoring emission at 475 nm with an excitation resolution of 1 nm. **Curve B:** 12K emission spectrum of MS-C in SF_6 with excitation at 320 nm, emission resolution 1 nm.

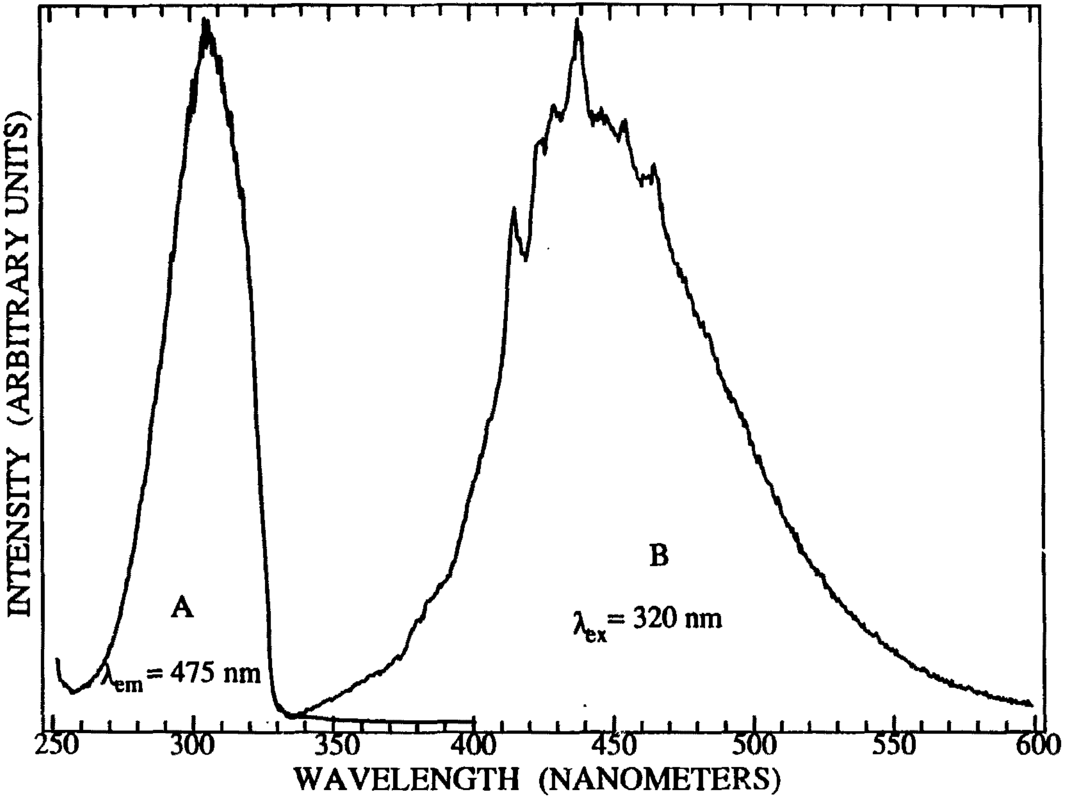
INTENSITY (ARBITRARY UNITS)
A
λ_{em} = 475 nm
B
λ_{ex} = 320 nm
250
300
350
400
450
500
550
600
WAVELENGTH (NANOMETERS)

yields, and/or the possible existence of a small amount of underlying phosphorescence. The value of 10.5 ± 1 nsec in argon matrix is however in good agreement with the 12 ± 2 nsec MS-C lifetime measured in neon matrix[19] Steady-state excitation and emission spectra of MS-C were recorded in argon, xenon, and SF_6 matrices. The crossing points for the fluorescence excitation and emission spectra define the $S_0 \rightarrow S_1$ 0-0 wavelengths, and are given for these three matrices in Table Xa.

UV, Excitation, and Emission Spectra of MS-E

The absorption spectrum of the photoproduct MS-E in xenon shown in Figure 17 is much less distinctly structured than that of OHBA-F, although it is not clear how much of this is due to the greater difficulty in making non-scattering xenon matrices. The features are, however, mimicked in the fluorescence excitation spectrum of MS-E in SF_6 (Figure 18, Curve A), blue-shifted by about 5 nm. Figure 18, Curve B is the fluorescence spectrum of MS-E, which appears to have the "mirror image" structure of the excitation spectrum. This emission is identifiable as fluorescence by the overlap of the longest wavelength excitation and shortest wavelength emission bands, and has been previously been observed in solution phase[20]. The measured lifetime of the ~1% MS-E UV-emitting component of a sample of methyl salicylate in acetonitrile is 1 nsec at 298K. An attempt was made to measure the lifetime of this fluorescence in 12K SF_6, but was unsuccessful due to the low emission intensity combined with the difficulty in obtaining a completely photolyzed matrix. Accurate values of the 0-0 energies are obtained from the excitation and emission spectra, and are given in Table Xb for both xenon and SF_6 matrices.

The entire emission spectrum of a partially (~50%) photolyzed matrix of MS-C in SF_6 is shown in Figure 19, Curve B, the long wavelength emission

TABLE Xa. 0-0 Transition Energies of MS-C

Matrix	T_1		S_1		S_2		S_3	
	nm	cm^{-1}	nm	cm^{-1}	nm	cm^{-1}	nm	cm^{-1}
Argon	n.a.		335*	29850*	n.a.		n.d.	
Xenon	n.a.		337*	29670*	n.a.		252	39680
SF_6	n.a.		332*	30120*	n.a.		n.d.	

TABLE Xb. 0-0 Transition Energies of MS-E

Matrix	T_1		S_1		S_2		S_3	
	nm	cm^{-1}	nm	cm^{-1}	nm	cm^{-1}	nm	cm^{-1}
Xenon	370.0	27030	317.3	31510	n.a.		246	40650
SF_6	367.6	27200	311.7*	32080	n.a.		n.d.	

* Values marked with asterisks represent crossing point between excitation and emission spectra, all others are the wavelength or frequency at half height of the leading peak in structured excitation, emission, or absorption spectra.

Figure 17. 12K UV absorption spectrum of partially photolyzed matrix of MS-C in xenon of Figure 15, showing growth of new structured features belonging to the product MS-E. Photolysis was with an average of 6 mWatts of power for 29 hours at 320 nm, while the resolution of the spectrometer was 0.2 nm.

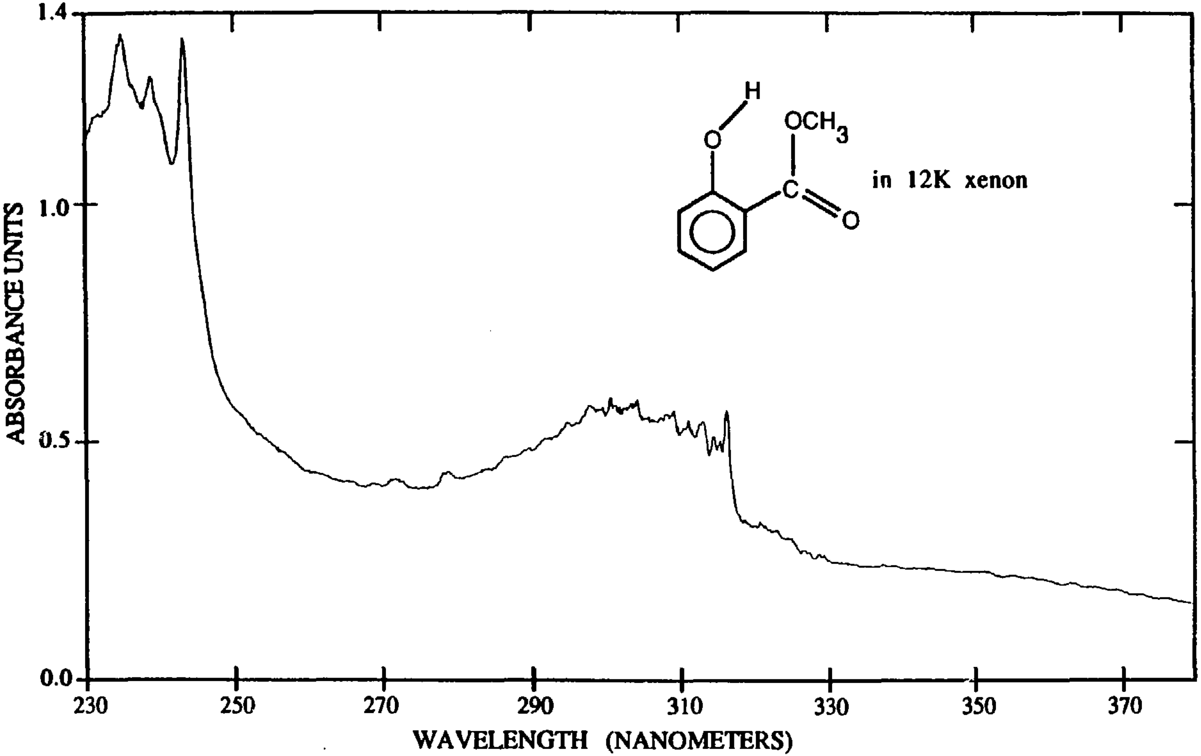

1.4
1.0
0.5
0.0
ABSORBANCE UNITS
230
250
270
290
310
330
350
370
WAVELENGTH (NANOMETERS)
H
O
OCH3
C
O
in 12K xenon

Figure 18. Curve A: 12K fluorescence excitation spectrum of MS-E in SF_6, monitoring emission at 340 nm, excitation resolution 0.4 nm. **Curve B:** 12K fluorescence spectrum of MS-E in SF_6 with excitation at 290 nm, emission resolution 0.4 nm.

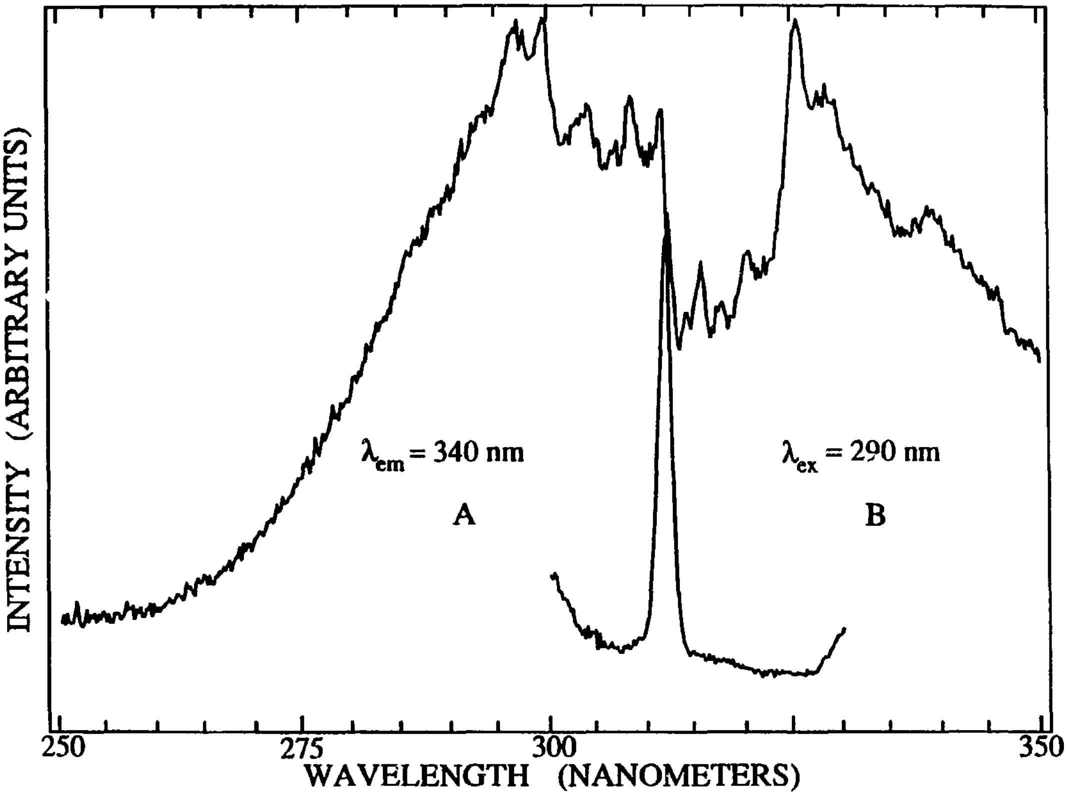
INTENSITY (ARBITRARY UNITS)
WAVELENGTH (NANOMETERS)
250
275
300
350
λ_{em} = 340 nm
A
λ_{ex} = 290 nm
B

Figure 19. Curve A: 12K phosphorescence excitation (λ_{em} = 392 nm) and **Curve B:** emission spectrum (λ_{ex} = 290 nm) of a partially photolyzed (about 50%) matrix of MS-C in SF_6. Structured features marked with asterisks in the emission spectrum are due to impurities from a previous experiment, while the band near 320 nm marked with an "X" in the excitation spectrum is due to excitation of residual MS-C which emits at 392 nm. The feature marked with a "√" is due to an impurity on the BaF_2 window, present prior to deposition.

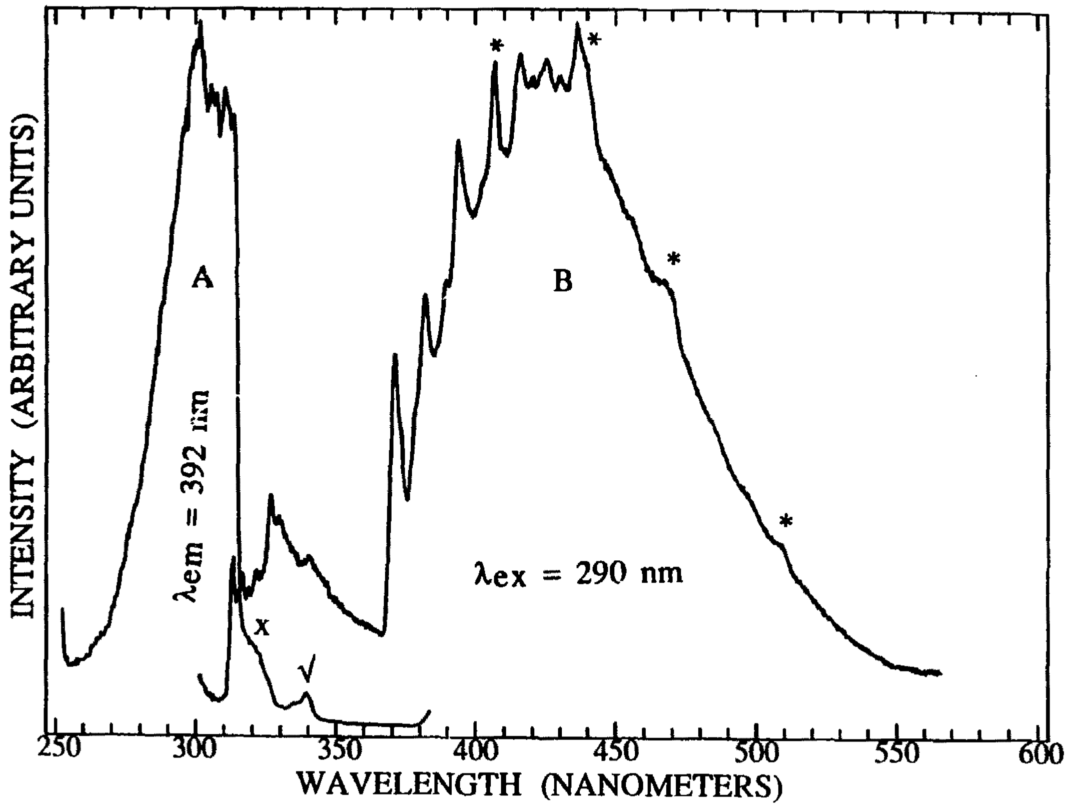
INTENSITY (ARBITRARY UNITS)
A
B
*
*
*
*
λem = 392 nm
λex = 290 nm
x
√
250
300
350
400
450
500
550
600
WAVELENGTH (NANOMETERS)

consisting mainly of a combination of residual MS-C fluorescence, and MS-E phosphorescence with a measured lifetime of 2.3 ± .2 seconds at 369 and 392 nm. With excitation of a partially photolyzed SF_6 matrix at 290 nm the emission at 475 nm consists of fluorescence from the residual MS-C and two sources of phosphorescence. The bulk of the phosphorescence (~70%) at 475 nm has the 2.3 second lifetime, while the second component has a lifetime of about 1 second. This shorter lived phosphorescent component detectable at the longer wavelengths is not present in the initially deposited MS-C matrices (>99% of the long wavelength emission decays within 0.2 seconds of closing the shutter), and it is still present with excitation at 330 nm, beyond the 0-0 energy of MS-E. Therefore it must originate from a second photolysis product of MS-C. As both CO and CO_2 are produced during photolysis of MS-C (see Figure 14), it may be a companion elimination product that is responsible for this second phosphorescence. Figure 19, Curve A is an excitation spectrum of mainly MS-E, monitoring emission at 392 nm. The low intensity feature at longer wavelength is due to excitation of the 392 nm fluorescence of the residual MS-C.

Due to the enhancement of spin-orbit coupling in heavy atom matrices, fluorescence is almost entirely quenched in xenon matrix. Thus, the emission spectrum of MS-E in xenon shown in Figure 20, Curve B has almost none of the UV fluorescence seen in solution phase and SF_6 matrix. Table IXb lists the energy differences between the 0-0 transitions and the peak maxima for the phosphorescence of Figure 20, Curve B and the fluorescence excitation and emission of Figure 18.

Photolysis of Methyl Salicylate

The rate of photolysis of MS-C to MS-E appeared to be matrix dependent, being fastest in xenon and SF_6, with increasingly slower rates in

Figure 20. Curve A: 12K excitation (λ_{em}=396 nm) and **Curve B:** emission (λ_{ex}=285 nm) of MS-E in xenon, resolution of 1 nm. As in Figure 18, feature marked with an "X" is due to residual MS-C, while that marked with a "√" is due to an impurity present before deposition.

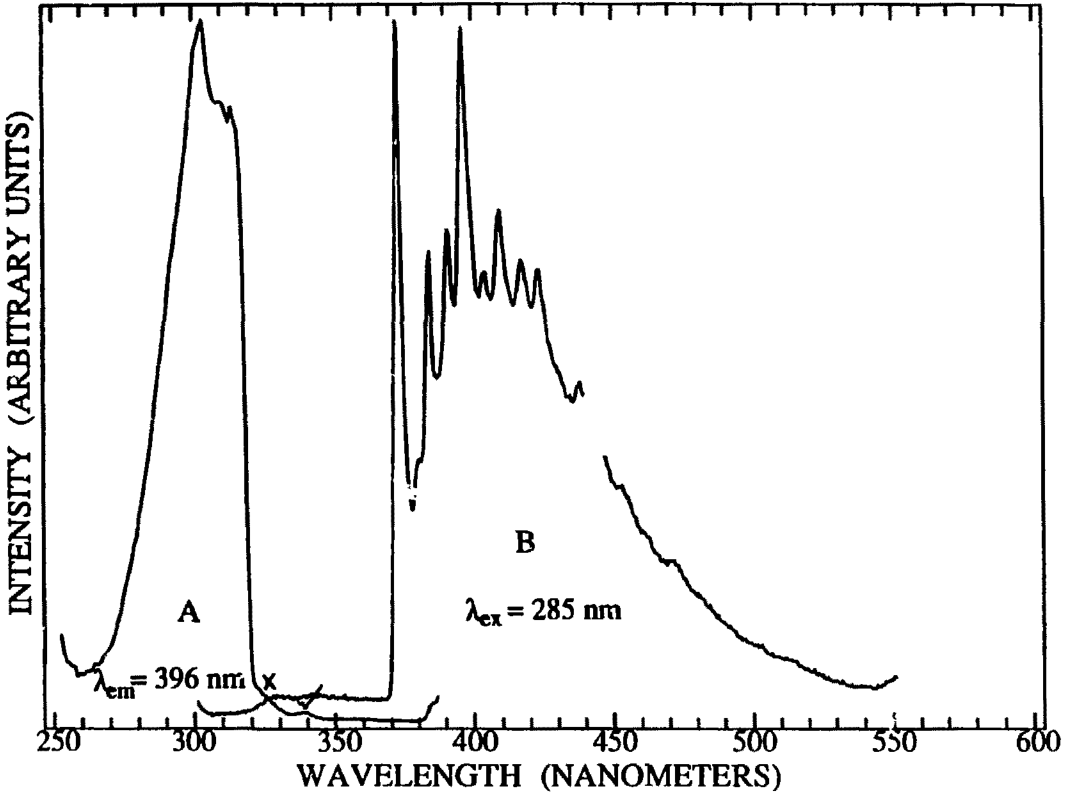
INTENSITY (ARBITRARY UNITS)
A
λ_{em}= 396 nm
x
B
λ_{ex} = 285 nm
250
300
350
400
450
500
550
600
WAVELENGTH (NANOMETERS)

krypton and argon, in the approximate ratio 15:15:10:1. Even in the faster matrices, these rates were slower than those for the photolysis of OHBA-C by two orders of magnitude or so. Photolysis at 320 nm required 8 hours of photolysis (5 mWatts power) to photolyze 75% of a sample of MS-C in xenon. Although photolysis of MS-C could be effected in the smaller cage size matrices of argon and krypton, the infrared absorption bands of difference spectra following photolysis were broad, suggesting that those molecules which do r[illegible] in these matrices are not isolated, but rather share a site with a second guest molecule and thus are in a larger cage site. In fact, in the time it took to photolyze away 10% of the carbonyl stretch absorbance at the frequency corresponding to isolated MS-C molecules, 90% of the carbonyl stretch band corresponding to non-isolated MS-C molecules disappeared. The broad absorption bands of the difference spectra are centered at the frequencies of the isolated MS-C and MS-E, so probably correspond to those molecules which share a matrix cage site with another guest molecule but are positioned such that there are no intermolecular hydrogen-bonding interactions.

Photolysis of MS-C in xenon matrix proceeds from wavelengths at least as long as 332.5 nm, and from 333 nm in SF_6, albeit slowly. Photolysis at all wavelengths produced small amounts of CO_2 and CO, identified in Figure 14 by the stretches at 2335 and 2129 cm^{-1}, respectively.

Attempts to photolytically regenerate MS-C from matrices photolyzed at 320 nm to produce a mixture with >90% MS-E were unsuccessful in both xenon and SF_6 matrices at wavelengths between 280 and 310 nm. Figure 21 is an SF_6 FTIR difference spectrum after photolysis for 4 hours (6 mWatts power) at 280 nm. There are no positive features attributable to the recovery of MS-C. Rather, it appears that MS-E reacts with SF_6 upon

Figure 21. FTIR difference spectrum of MS-E in 12K SF_6 and its photolysis products after 4 hours photolysis at 280 nm with 6 mWatts of power. Regions marked with an asterisk (*) are ones of intense absorption by the matrix SF_6, such that subtraction is not reliable in this region.

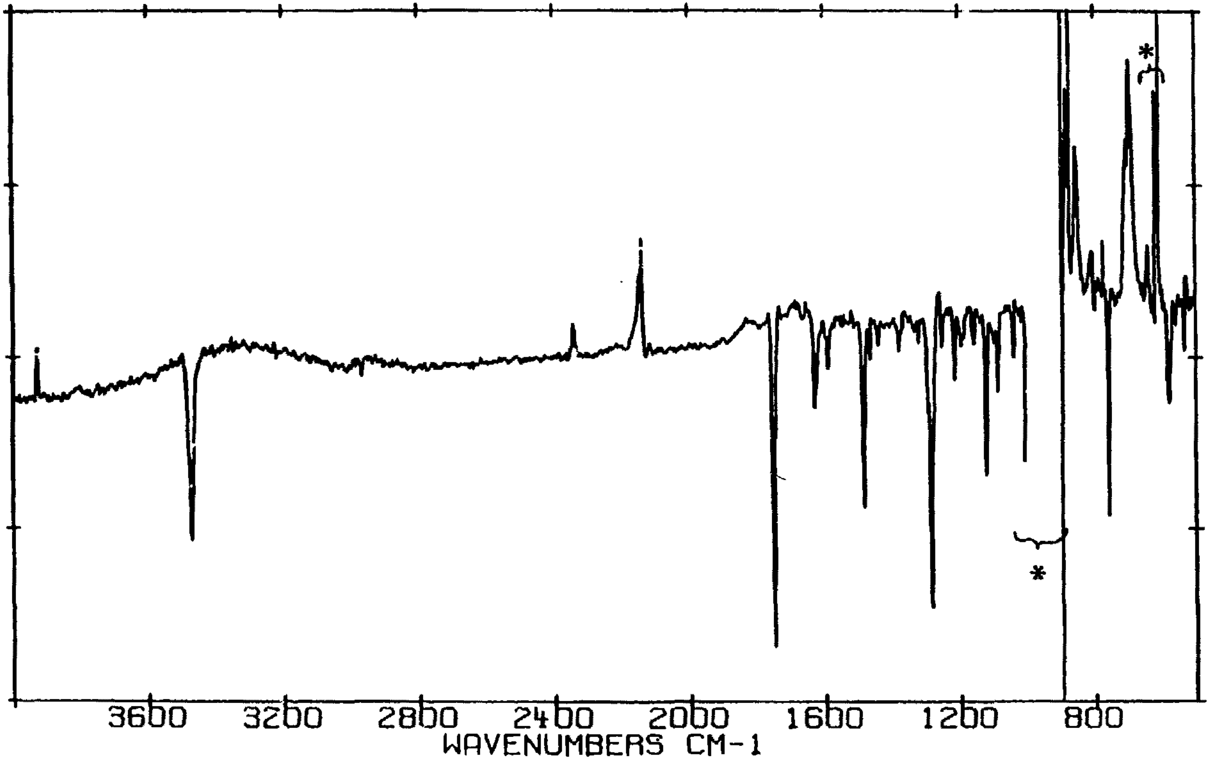

*
*
3600
3200
2800
2400
2000
1600
1200
800
WAVENUMBERS CM-1

photolysis, in that there is a small absorption feature at 3930 cm^{-1}, in the absorption region of HF. Other positive features in this difference spectrum include absorptions attributed to CO and CO_2, and a large, broad, unidentified feature at 690 cm^{-1}. Subtraction is unreliable in the spectral regions where the host SF_6 matrix absorbs strongly. These regions are marked with asterisks in Figure 21.

The analogous experiment in xenon (7 hours, 6 mWatts power) produced only CO and CO_2 product peaks. A search for non-hydrogen-bonded phenolic substances, expected upon elimination of CO or CO_2 and identifiable by a peak near 3630 cm^{-1}, was unsuccessful in both these matrices.

CHAPTER IV. DISCUSSION OF OHBA AND MS RESULTS

o-HYDROXYBENZALDEHYDE

Ground States, 0-0 Energies and ΔH

Figure 22 is a summary of the 0-0 energy levels measured for OHBA in argon matrix. The 0-0 energies of the excited states form a basis for further discussion of barriers, reaction pathways, and the major coordinates of distortion in the excited states. The singlet surfaces are depicted with two minima along the reaction coordinate, the reasoning being that the fluorescence from OHBA-C's S_1 state is indicative of a minimum in S_1 above the ground state, while the vibrational structure present in the excitation spectra of OHBA-F is indicative of bound potentials in both the S_1 and S_2 states of that conformer. Ground state energies for the two forms, OHBA-C and OHBA-F, are offset by the value for ΔH, which, as discussed below, is estimated at 3.5 kcal/mole.

While a complicated reaction pathway involving proton transfer, rotation, and back transfer could conceivably be invoked, the reaction coordinate between OHBA-C from OHBA-F is most simply described by two angles of quasi-disrotatory rotation of the aldehydic and hydroxyl groups. For equal and opposite rotations this reaction coordinate can be described by a single angle Θ. The quasi-disrotatory reaction pathway is proposed because the hydrogen bond would be expected to be maintained for small (bound state) Θ, coupling rotation of the hydroxyl and aldehydic moieties and discouraging quasi-conrotatory motion. Whether or not the saddlepoint of the reaction surface corresponds to perpendicular orientation of both groups is certainly debatable. The rotations could be staggered, and could even be staggered different amounts at the saddle points of the three singlet surfaces. Thus, the reaction coordinate is not rigorously defined for this

Figure 22. Summary of 0-0 energies obtained for OHBA-C and OHBA-F in 12K argon matrix by absorption, excitation and emission spectroscopies.

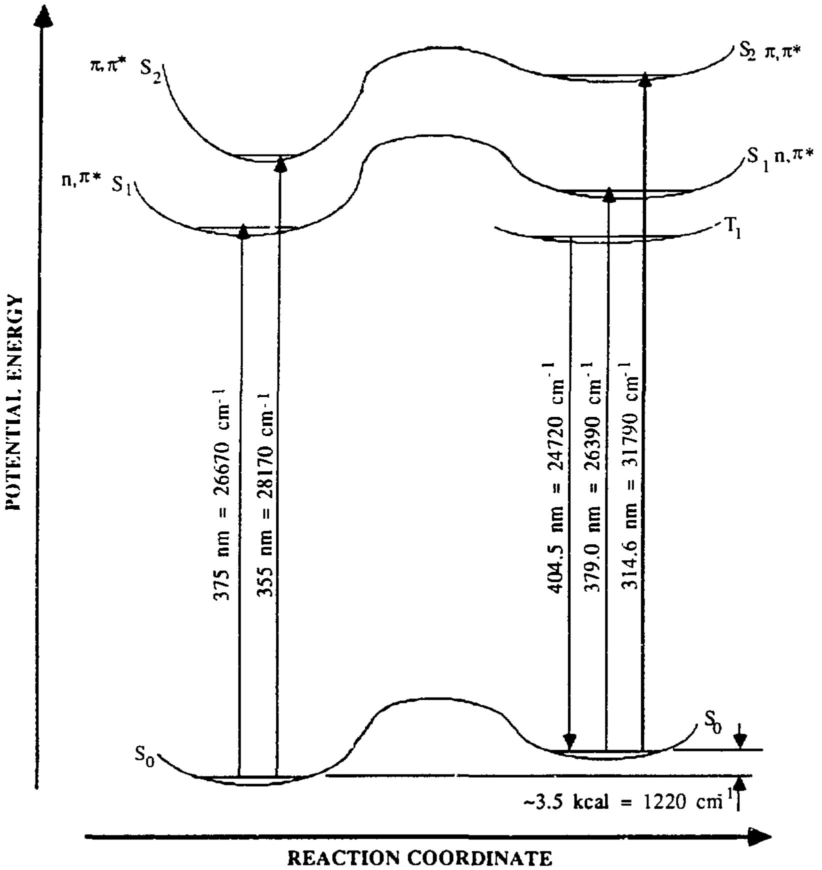
POTENTIAL ENERGY
π,π* S2
n,π* S1
S0
S2 π,π*
S1 n,π*
T1
S0
375 nm = 26670 cm-1
355 nm = 28170 cm-1
404.5 nm = 24720 cm-1
379.0 nm = 26390 cm-1
314.6 nm = 31790 cm-1
~3.5 kcal = 1220 cm-1
REACTION COORDINATE

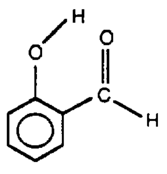
OHBA-C

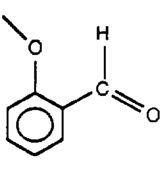
OHBA-F

system.

The 3.0 kcal/mole solution-phase UV measurement of ΔH in n-decane (Chapter III) has a sizable degree of uncertainty associated with it since it was calculated with the assumptions that there is no absorption of OHBA-F at 340 nm and that the absorption spectrum of OHBA-C is temperature-invariant. The first assumption is quite reasonable since the matrix phosphorescence excitation spectrum (Figure 6) shows that at wavelengths longer than 315 nm OHBA-F's absorption is more than 40 times weaker than in the region between 300 and 315 nm. The second assumption is less reasonable however, in that an increase in absorption at the long wavelength edge of both the S_1 and S_3 absorption systems of OHBA-C is detected at the higher temperatures.

When ground state activation energies to isomerization are sufficiently high and cooling is sufficiently rapid, the distribution of the isomers in the cryogenic rare gas matrix is determined by the equilibrium distribution in the vapor phase. This has been shown to be the case for deposition of 1,2-difluoroethane onto a 12K CsI window, which has a 2 kcal barrier to formation of the most stable rotamer[21]. Since the ground state barrier to formation of OHBA-C from OHBA-F is expected to be as high or higher than the 7.9 kcal barrier to rotation of the aldehyde group in benzaldehyde[12], none of the OHBA-F present in the room temperature vapor should convert to OHBA-C upon condensation onto the 12K CsI window. However, the deposition argon matrix IR spectrum indicates that less than 1% OHBA-F is deposited on a CsI window at 12K from the room temperature vapor phase, while the 3.0 kcal value for calculated for ΔH and the 3.9 e.u. value calculated for ΔS imply a room temperature concentration of 4% OHBA-F. Thus, there is cause to search the literature for evidence to support or refute the 3 kcal/mole measurement of ΔH.

ΔH has previously been measured by ultrasonic relaxation techniques at 2.3 ± 0.7 kcal[22], although this measurement was with neat samples, where there is opportunity for formation of intermolecular hydrogen-bonds. A number of estimates of ΔH based on indirect methods also exist. Work by Schaefer[23] places the hydrogen-bond energy of OHBA-C at 7.2 kcal, from a correlation of OH NMR frequency shifts and OH torsional frequencies of substituted phenols with known hydrogen-bond energies. Further theoretical work[24] estimates the energy difference between OHBA-C and OHBA-F at 5.6 kcal, less than the strength of the hydrogen-bond, since rupture of the hydrogen-bond allows for strengthening of the other bonds (demonstrated by an increase in the carbonyl stretching frequency from 1673 to 1701 cm^{-1}), while rotation of both the phenolic and aldehydic groups results in a less crowded conformation. Pictured below, along with OHBA-F, is the rotamer of OHBA-C formed upon cleavage of the hydrogen-bond and rotation of only the phenolic group. The oxygen-oxygen distance in this form and the phenolic oxygen-aldehydic proton distance in OHBA-F are both around 2.6 Å[24]. As the van der Waals radii of oxygen and hydrogen are 1.4 and 1.2 Å, respectively, OHBA-F is sterically preferable to a conformation with adjacent oxygen atoms.

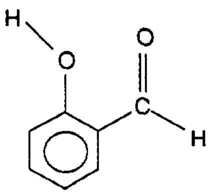

phenolic rotation only

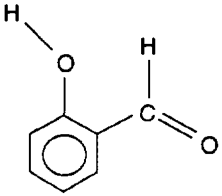

OHBA-F

The most stable conformation of o-fluorobenzaldehyde is one in which the interaction between the aldehydic proton and the fluorine is maximized[13]. This interaction is reflected in its relatively high aldehydic stretch (2881.3, 2771.3 cm^{-1}) and in-plane bend (1402.2 cm^{-1}) frequencies, higher than those of benzaldehyde (2827, 2744 cm^{-1}; and 1388.9 cm^{-1}, respectively), or those of OHBA-C (2850, 2751 cm^{-1}; and 1386.7 cm^{-1}, respectively).[10] Such an interaction is also apparent from the IR spectrum of OHBA-F, whose aldehydic C-H stretch (2884, 2771 cm^{-1}) and in-plane bend (1401.7 cm^{-1}) frequencies are similarly high. This positive interaction (perhaps electrostatic in nature) between the aldehydic proton and the phenolic oxygen, apparently not considered in the calculations by Schaefer et al.[24], is consistent with a lower value for ΔH than the 5.6 kcal suggested by them. In any case, all spectroscopic data and calculations are in accordance with the assignment of the non-hydrogen-bonded photolysis product of OHBA-C as OHBA-F.

Tabei et al.[25] estimate the stabilization due to an internal hydrogen-bond in OHBA-C-like structures at 3.4-3.6 kcal/mole. They measured the temperature dependence of NMR line widths and line shapes for 4-methyl 2,6-diformyl phenol (MDP, pictured below), and from these data calculated a ΔF^* of 11.3±0.1 kcal/mole at 223K for the internal rotations of MDP to MDP'.

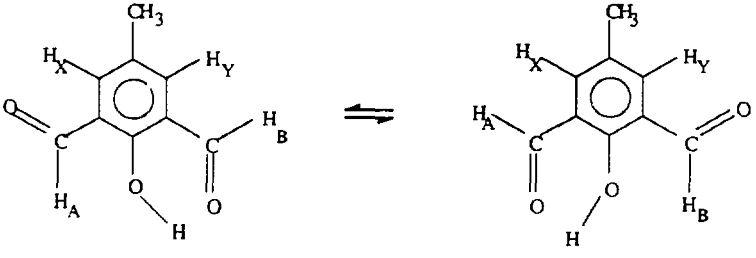

MDP MDP'

Subtraction of a ΔF^* value of 7.9 kcal/mole for the rotation of benzaldehyde[12] yields a hydrogen-bond stabilization energy of 3.4-3.6 kcal/mole. Assuming small and similar values of ΔS* for MDP and benzaldehyde (that for MDP was calculated to be 3.6 ± 2.0 e.u.), and a negligible difference between ΔF and ΔG in solution phase, 3.5 kcal/mole is then a reasonable estimate of ΔH for OHBA-C and OHBA-F. Further work[26] measuring the temperature dependence of NMR line shapes of 2,6-dihydroxybenzaldehyde yielded an estimate of 2.1 kcal/mole as the enthalpy of formation for a hydrogen bond between a phenolic proton and an adjacent formyl carboxyl group, but this measurement is probably low since the solvent was diethyl ether, which is both polar and capable of forming hydrogen bonds with phenol.

The above examples indicate that values for the intramolecular hydrogen bond strength in OHBA-C might reasonably lie anywhere between 2.0 and 5.6 kcal. With the choice of a median value, and consideration of a possible aldehydic proton interaction along with the more favorable geometry and increased strength of the carbonyl bond in OHBA-F, the enthalpy difference between OHBA-C and OHBA-F is estimated to be 3.5 kcal/mole, close to the value determined experimentally by UV. Clearly, a sound determination of ΔH is in order, as it is certainly conceivable that ΔH could be as high as the 5.6 kcal estimated by Schaefer et al.[24] or as low as the 3.0 kcal measured by UV spectroscopy.

Excited State Barriers

The abrupt loss of vibrational structure in an excitation or absorption spectrum at higher excitation energies is one indication of the end of the bound region of the excited state potential well. The phosphorescence excitation spectrum of OHBA-F (Figure 6) displays sharp well-defined structure near both the S_1 and S_2 0-0 transitions, which dies away at higher excitation energies. While the shape of the S_1 377.8, 374.4 nm doublet is cleanly repeated 1324 cm^{-1} higher in energy at 359.8, 356.6 nm, the third member of this progression at 343.4, 341.0 nm is more diffuse. No fourth member is detectable at all. Thus, an unbound region of the potential well is first indicated by 343.4 nm, 7.8 kcal above the S_1 0-0 energy.

The next point of discussion is whether this threshold to an unbound portion of the potential surface corresponds to the barrier energy in the OHBA-F → OHBA-C S_1 reaction coordinate, which has been discussed previously in terms of concerted, quasi-disrotatory motion of the aldehydic and hydroxyl groups. The only unimolecular reactions accessible at energies lower than the dissociation energy of one of the sigma bonds are ones of internal rotation, of which only one combination forms the reaction coordinate leading to OHBA-C. However, since free rotation of only one or the other of the aldehydic or hydroxyl groups results in electrostatically repulsive interactions the rotations must be coupled in a quasi-disrotatory manner, the same motion proposed for the reaction coordinate. Thus, the energy of the onset of the less structured portion of the S_1 excitation is proposed to correspond to the barrier to formation of OHBA-C on the S_1 surface.

The 7.8 kcal barrier value is very close to the 7-8 kcal barrier proposed for the ground state[25,12]. The ground state barrier to formation of OHBA-C from OHBA-F is thought to be derived mainly from the energy required to take the phenolic and aldehydic groups out of conjugation with the π system, leading one to think that it would be lowered in the excited state where the net number of π bonding electrons is decreased. However, as n,π^* excitation lowers the net π bonding electrons only a fraction, from eight to seven, this effect should be fairly small.

Excitation into the S_2 π,π^* state lowers the net number of π bonding electrons from eight to six, leading one to expect a smaller barrier in the S_2 excited state than in S_1. This is borne out by the excitation spectrum (Figure 6), which shows an abrupt decrease in vibrational structure at 301.8 nm, only 1400 cm^{-1} (4.0 kcal) above the S_2 0-0 energy.

The vibrational structure in the phosphorescence spectrum (Figure 7) does not however provide such a clear indication of the end of the bound region in the ground state potential. The ~1700 cm^{-1} progression extends to vibrational levels 19 kcal above the ground state energy, well above the experimentally determined ground state barrier to reaction of 7-8 kcal. Furthermore, only a modest increase in the FWHM of these peaks is detected with increasing emission wavelength (103, 148, 159, and 189 cm^{-1} for the 405.3, 435.2, 469.6, and 509.0 cm^{-1} peaks, respectively). As is discussed later in this chapter, this progression corresponds to motion in the carbonyl stretch coordinate. A better indication of the end of the bound region might then come from examination of the structure in a lower frequency torsional mode characteristic of the reaction coordinate.

A low frequency mode is detectable in the spectrum of Figure 7, with peaks located 199, 225, 251, and 292 cm^{-1} above the dominant 1700 cm^{-1} progression peaks (Table IV). While the first members at 408.6 and 439.5 nm are quite sharp, the third member at 475.2 nm, into a vibrational state 10.5 kcal above the ground state energy, is less so. However, it is unclear at this resolution whether the breadth of the longer wavelength peaks stems from emission into a vibrational state which is, or is coupled strongly to, unbound vibration in the reaction coordinate, or whether the increasing breadth arises from emission into increasing numbers of vibrational states of the low frequency mode.

The 7.8 and 4.0 kcal barriers proposed for the formation of OHBA-C from OHBA-F in S_1 and S_2, respectively, imply barrier heights for the reverse process. Assuming a 3.5 kcal value for ΔH, the corresponding S_1 and S_2 barriers to formation of OHBA-F from OHBA-C are 10.6 and 17.7 kcal, respectively. While the S_1 barrier is again comparable to the proposed ground state barrier, the S_2 barrier is considerably higher. An explanation for this lies in the excited states proposed for OHBA-C.

Both proton transfer[27] and hydrogen-atom transfer[16] structures have been suggested for the S_1 states of molecules such as o-hydroxybenzaldehyde and methyl salicylate. The bond distributions for OHBA-C proton and hydrogen-atom transfer excited states are given below.

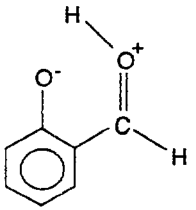

Proton Transfer

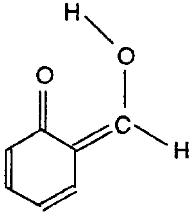

Hydrogen Transfer

These two structures should be spectroscopically distinguishable rather than simply resonance structures of each other. The structure of the hydrogen-atom transfer state includes both keto-enol and o-quinonemethide moieties, for which many examples of stable molecules are known. The zwitterionic proton transfer state, with retention of its aromatic character, is also expected to have a potential minimum associated with it.

Nishiya et al.[16] interpret the structure in the excitation spectrum of the closely related o-hydroxyacetophenone as confirmation of π,π^* excitation to a keto-enol state. They cite in particular a 1607 cm^{-1} feature, which they attribute to π,π^* excitation of a ring-CO stretch with considerable double bond character. One however expects an n,π^* state to be more efficient at hydrogen abstraction, due to the single electron left adjacent to the hydrogen in a non-bonding orbital[28], while excitation of a carbonyl π electron to a π,π^* state, with the concomitant increase in basicity of the carbonyl group, facilitates formation of the zwitterionic, proton transfer state.

Large enthalpies of formation have been measured for hydrogen-bonds in species such as the acetic acid - potassium acetate dimer, in which the acid proton is strongly hydrogen bonded to an oxygen with a formal negative charge. Hydrogen bonds of this type have enthalpies in the range 11-15 kcal/mole[29]. The enthalpy of formation of the hydrogen-bond in OHBA-C's proposed proton transfer π,π^* state might be expected to be just as great, since there is a formal negative charge on the accepting oxygen and a formal positive charge on the donating oxygen. Such an 11-15 kcal intramolecular hydrogen bond would greatly stabilize the π,π^* proton transfer state relative to the transition state. On the other hand, the hydrogen-atom transfer state would be stabilized by an intramolecular hydrogen bond of only a few kcal, and destabilized by a loss in aromaticity. Thus, while the barrier to formation of OHBA-F from OHBA-C on the S_1 n,π^* surface would be expected to be lower than the ground state barrier, a large barrier on the S_2 π,π^* surface is consistent with the proposed strongly hydrogen-bonded S_2 proton transfer state, which is in turn consistent with accepted notions about excited state basicities.

A map of the reaction coordinates of OHBA-C and OHBA-F derived from this examination of OHBA-F's excitation spectra is presented in Figure 23. The proposed excited state barriers provide a guide for interpretation of a

Figure 23. Map of the first four electronic states of OHBA-C and OHBA-F derived from absorption, excitation and emission spectra in 12K argon matrix.

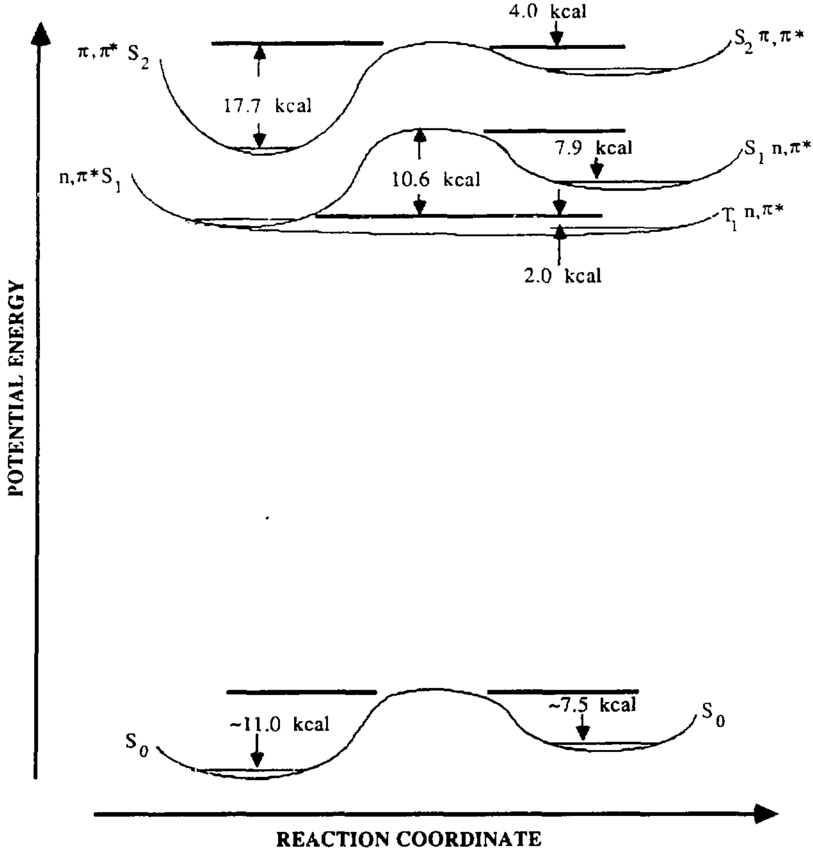
4.0 kcal
π, π* S₂
S₂ π, π*
17.7 kcal
7.9 kcal
S₁ n, π*
n, π* S₁
10.6 kcal
T₁ n, π*
2.0 kcal
POTENTIAL ENERGY
~11.0 kcal
~7.5 kcal
S₀
S₀
REACTION COORDINATE

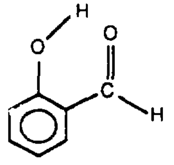
H
O
O
C
H

OHBA-C

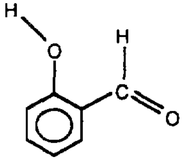
H
O
H
C
O

OHBA-F

wavelength dependence of the reaction quantum yield.

A modest increase in the quantum yield for photolysis of OHBA-C to OHBA-F at higher energies is indicated in Figure 9, provided that the smaller values for the extinction coefficients are used in calculating the relative quantum yields. As it seems entirely reasonable to exclude from the absorption coefficients that portion of the light attenuation due to scattering by the argon, discussion will rely on the median values, connected by the dashed line in Figure 9, which indicate an increase in the quantum yield by about 310 nm, and certainly by 295 nm.

If the 295-310 nm discontinuity in the wavelength dependence of the reaction quantum yield indicates the height of the barrier to reaction on the S_1 surface, it is somewhat at odds with the 10.6 kcal barrier determined from the vibrational structure in OHBA-F's excitation spectrum, in that 310 nm is 16.0 kcal above the 0-0 energy of OHBA-C's S_1 state. One source of this 5.4 kcal discrepancy might lie in the ΔH required to determine OHBA-C barriers from OHBA-F spectra. Use of the 5.6 kcal ΔH value, that calculated by Schaefer et al.[24], lowers this discrepancy to 3.3 kcal.

Another source of the 5.4 kcal discrepancy in the barrier measurements could be the quantum yields themselves, which do have considerable associated uncertainty (particularly at the shorter wavelengths) as given in Table V. While a wavelength dependence of the reaction quantum yield is retained within the assumptions about scattering and the uncertainty of the measurements, the precise energy of the discontinuity is uncertain. Another concern is that the quantum yields might appear higher at wavelengths where the UV extinction coefficient is low and it is easier to maintain a lower optical density. This concern does not however appear to be realized, as the measurement of the ratio of quantum yields (Figure 11), which does not depend on the optical density at the photolysis wavelength, also appears to have a wavelength dependence.

The decrease in vibrational structure in Figure 6 is also an uncertain measure of the excited state potential well depth, in that the persistence, or absence, of vibrational structure is determined by both the lifetime of the excited vibronic state and by Franck-Condon factors. Poor Franck-Condon overlap, or merely a very congested spectrum, could produce a barrier estimate too low in energy. On the other hand, while intramolecular vibrational redistribution is thought to be facile at energies where there is a sufficient density of states (30 states/cm^{-1} has been suggested as being "sufficient"[30]), vibrational structure can persist at excitation energies above a reaction barrier if the vibrational mode involved in the chromophore couples poorly to other modes. This may provide the explanation for the persistence of the 734 + n1300 cm^{-1} progression, which continues well above what seems to be a reasonable barrier in the S_1 state of OHBA-F.

In a similar vein, RRK theory predicts that the probability of a reaction is dependent on excess energy.[31] For a system of S classical oscillators with energy E, the probability P that a particular oscillator will have sufficient energy for reaction (E > E_0, the threshold energy), is given by the relation $P = (E - E_0/E)^{S-1}$. Accordingly, increases in the quantum yield at the threshold to the new reaction pathway will be very small, a problem exacerbated in the case of OHBA by the already sizable quantum yield obtained below the S_1 barrier. Thus, the discontinuity in the wavelength dependence of the reaction quantum yield in Figure 9 may actually occur at a considerably longer wavelength than 310 nm, perhaps even as long as 320 nm. With a ΔH value of 5.6 kcal and a 320 nm threshold, the S_1 barrier is calculated to lie 341 nm above OHBA-F's ground state energy, in reasonable agreement with the diminution in the vibrational structure in OHBA-F's S_1 excitation spectrum.

There are alternate explanations for a wavelength dependence of the reaction quantum yield of OHBA-C. It is possible that internal conversion and/or intersystem crossing is more effective with excitation to higher vibrational states in S_1. This phenomenon has been observed previously under collisionless gas phase conditions, where rates of non-radiative decay from S_1 for such molecules as benzene[32] and napthalenes[33] are wavelength dependent. This phenomenon is thought to arise from the increased coupling to non-radiative states at higher excitation energies, provided both by anharmonicity in the higher states and the better Franck-Condon overlap for displaced potential wells at higher vibrational levels. As excitation to a point below the S_1 barrier provides a route to reaction which must occur on a lower energy surface, such as a triplet state or the ground state, more efficient transfer to the triplet or vibrationally excited levels of the ground state might result in a higher reaction quantum yield.

Another possibility is that a higher energy absorption system, such as a triplet state, another n,π^* state, or even the S_2 state, provides a reaction surfaces. If the discontinuity in the wavelength dependence of the quantum yield is actually at 295 nm and the correct ΔH value is 3.0 kcal, an S_2 barrier 304.4 nm above OHBA-F's ground state is implied, somewhat lower in energy than that indicated by the excitation spectra, but not entirely out of bounds.

Unfortunately, it was not possible to accurately confirm the energy of the proposed higher energy reaction route by measuring the wavelength dependence of the reaction quantum yield for the photolysis of OHBA-F to OHBA-C. Due to the smaller quantum yield for this reaction, it was necessary to determine rate constants for this reaction at those wavelengths where OHBA-F absorbs significantly more than OHBA-C. This restriction adds uncertainty in the region between 300 and 315 nm, due to the large extinction coefficients at the maxima of the spiked features in OHBA-F's absorption spectrum (see Figure 5). Further uncertainty in the reaction quantum yield for the reverse process arises from the difficulty in accurately measuring absorption coefficients of spiked features, and the complication that the two or more matrix cage sites have somewhat resolved UV absorption peaks. The problem of the partially resolved UV absorptions for the different sites is illustrated by the 50% higher quantum yield calculated for photolysis at 313.6 nm than at 314.0 nm (see Figure 10). Due to the very low absorption intensity of OHBA-F at wavelengths longer than 315 nm, and the sizable absorption coefficient of OHBA-C up to 355 nm, it was not possible to measure the wavelength dependence of the reverse reaction quantum yield between the wavelengths 315 and 355 nm.

In conclusion,

a) The excitation, absorption, and time-resolved emission spectra of OHBA-C and OHBA-F are consistent with an n,π^* S_1 surface and a π,π^* S_2 surface. The reaction coordinate connecting these conformers is represented best by a double well potential.

b) The vibrational structure in OHBA-F's S_1 and S_2 excitation spectrum, the 0-0 transition energies, and the enthalpy of reaction are consistent with an n,π^* hydrogen-atom transfer state of OHBA-C, and an S_2 π,π^* proton transfer state with a large barrier to formation of OHBA-F. The energies of the proposed excited state barriers are summarized in Figure 23.

c) A wavelength dependence of the quantum yield for formation of OHBA-F from OHBA-C is detected, within the assumption that scattering of argon contributes to the light attenuation in an argon:OHBA-C matrix. Sizable uncertainties, particularly in the extinction coefficient at short wavelengths, make identification of the wavelength onset of the proposed high energy reaction pathway uncertain. Precise determination of the barrier to the higher energy reaction route is further hampered by the sizable (~0.2) quantum yield for the reaction upon excitation near the S_1 0-0 energy. Without a more precise value for the energy of this barrier, it is difficult to identify the nature of the apparent high energy reaction route, but one involving reaction over the S_1 barrier is favored.

Reaction Pathways Below the S_1 Barrier

As mentioned previously, photolysis of OHBA-C proceeds at wavelengths at least as long as 371.1 nm, only .8 kcal above the assigned S_1 0-0 energy. In the reverse direction, regeneration of OHBA-C from OHBA-F can be achieved at the maximum of the S_1 0-0 peak at 377.8 nm. Thus, reaction pathways exist below the S_1 surface.

One source of information on the low energy reaction pathways is the ratio of the forward and reverse reaction quantum yields pictured in Figure 11. The five-fold greater efficiency of the forward reaction at the longer wavelengths is compatible with two possibilities. The first is that reaction proceeds in the excited vibrational states of the ground state manifold, with the ratio of the quantum yields for the two reactions determined at least in part by the quantum yields for emission, which produces vibrationally cool, unreactive ground state molecules. The fluorescence of OHBA-C has a measured quantum yield of 0.024 in 77K 3-methyl pentane[34], and can only be expected to be higher the cryogenic rare gas matrix environment. OHBA-F's phosphorescence quantum yield is approximately 11 times greater than the OHBA'-C's fluorescence quantum yield. Thus, upon excitation to OHBA-C's

S_1 state internal conversion will occur as much as 97.6 percent of the time, whereas excitation to OHBA-F's S_1 state will result in internal conversion at most 73.6 percent of the time, thereby favoring the reaction of OHBA-C to OHBA-F.

Another alternative is that the triplet surface is involved in the low energy reaction pathway. Although Figure 12 does not indicate any enhancement of the forward reaction relative to the reverse reaction in the triplet-directing xenon matrix, there is also no change in the fluorescence lifetime of OHBA-C in xenon from the 0.9 nsec lifetime in argon. This indicates that transfer from OHBA-C's S_1 surface to the triplet surface may already be extremely efficient. There is however no evidence for phosphorescence from OHBA-C, whereas OHBA-F phosphorescences strongly. Consistent with these data then is a triplet state that is close in energy to OHBA-C's S_1 state, promoting efficient intersystem crossing, and on which there is little or no barrier to formation of the T_1 state with the nuclear geometry of OHBA-F. This is energetically possible since, assuming a 3.5 kcal enthalpy difference between OHBA-C and OHBA-F, OHBA-C's S_1 state, 375 nm above its ground state, lies 2.0 kcal above OHBA-F's T_1 state, which is in turn 405.3 nm above its ground state. A five-fold difference in the reaction quantum yields might then result from a low-barrier triplet forward reaction dominating over a high-barrier ground state reverse reaction.

One further note is that Nagaoka et al.[34] have measured the temperature dependence of the non-radiative decay rates for OHBA-C, and have calculated a 1.7 ± 0.3 kcal (590 cm^{-1}) activation energy to a non-radiative decay channel above the fluorescent S_1 0-0 state. While no wavelength dependence of the reaction quantum yield was detected in this region, this proposed non-radiative decay channel may also be one of efficient reaction.

Distortion and Displacement in the Excited States of OHBA

The vibrational modes which contribute to better Franck-Condon and/or symmetry overlap can be determined from vibrational structure in absorption, excitation and emission structure, while the degree of displacement along a particular coordinate can be determined from the Franck-Condon maximum. As each excited state has its own characteristic bonding and distortion, they will be discussed individually, beginning with the T_1 state of OHBA-F, which presents the most easily interpreted, and thus most illustrative, case.

OHBA-F, T_1. The most striking aspect of the phosphorescence spectrum of OHBA-F (Figure 7) is the series of sharp spikes with maxima at 405.3, 435.2, 469.6, 509.0 and 554.8 nm, spaced progressively 1695, 1683, 1648 and 1622 cm^{-1} apart, each with an uncertainty of ± 10 cm^{-1}. Assuming that the shortest wavelength transition corresponds to emission into the $v = 0$ state, subsequent features reflect emission into the $v = 1, 2, 3,$ and 4 levels of the ground state. This progression can then be readily associated with the 1701 cm^{-1} $v = 0 \rightarrow v = 1$ carbonyl stretch absorption detected in the IR spectrum.

The areas of the peaks are in the ratio of approximately 1.0: 3.0: 2.0: 1.0: 0.4, in order of increasing wavelength. The area of integration for each of the peaks includes the entire band in the wavelength region between the intensity minima to the immediate left and right of the peak in Figure 7. For example, the 435.2 peak was integrated between the wavelengths 428.7 and 438.7 nm. The combined area of the carbonyl progression peaks accounts for approximately 56% of the total integrated phosphorescence intensity. Thus, the carbonyl group is the major component of the chromophore for this n,π* transition.

A dominant carbonyl stretch vibrational progression is considered to be typical for an n,π* transition in benzaldehydes[34]. Assignment of the carbonyl group as the major component of the n,π* chromophore must however be consistent with the observed Franck-Condon maximum into the v = 1 state. The Franck-Condon principal states that the relative intensity of a transition between two vibrational states is essentially proportional to the overlap between the wavefunctions of those states. The overlap is called the Franck-Condon factor, and can be expressed mathematically as $|\int\psi^*_{vib'}\psi_{vib}dR|^2$. The wavefunctions of vibrational states are to a good approximation those of an harmonic oscillator, particularly in the lower vibrational states. The form of these harmonic oscillator wavefunctions is well known[35]. The Franck-Condon factors can then easily be determined for emission from the v' = 0 state of an harmonic oscillator potential of force constant k' and displacement b to the v = 0, 1, and 2 states of an harmonic oscillator potential of force constant f. These three Franck-Condon factors were determined for a number of values of b, with the following assumptions and approximations:

a) The "carbonyl stretch" normal mode is approximated as that of a diatomic, with a reduced mass of (12 + 16/12 x 16 = 6.857 g/mole).

b) The force constant k of the ground state potential is characterized by the 1701 cm^{-1} stretch frequency and the reduced mass, while the force constant of the excited state is characterized by the 6.857 g/mole reduced mass and a 1324 cm^{-1} carbonyl stretch vibrational frequency. The T_1 stretch frequency is an approximation based on the vibrational progression in the $S_0 \rightarrow S_1$ excitation spectrum (see below). This value is slightly higher than the 1312 cm-1 frequency determined for the n,π* T_1 state of benzaldehyde in methylcyclohexane.[36]

Franck-Condon factors with b, the displacement of the excited state potential, set to 0.10 Å were calculated to be 0.218, 0.289, and 0.231 for emission from the v' = 0 state into the v = 0, 1, and 2 states, respectively. The analogous values with b set to 0.09 Å were calculated to be 0.291, 0.312, and 0.210; while those calculated with b set to 0.11 Å are 0.158, 0.254, and 0.237. Franck-Condon factors with larger values of b favored emission into the v = 2 state, while lower values of b favored emission into the v = 0 state, as expected. The closest correspondence between the Franck-Condon factors and the 1.0: 3.0: 2.0 intensity ratio for emission into the v = 0, 1, and 2 states of the carbonyl stretch mode is with an excited state displacement of approximately 0.11 Å in that mode. The average length of a non-hydrogen-bonded aldehyde carbonyl bond is approximately 1.22 Å[37], so the calculated carbonyl bond length of OHBA-F in its T_1 state is ~1.33 Å, which is midway between the C=O double bond length and an average alcoholic C-O single bond length of 1.43 Å[37]. Thus, an emission maximum into the carbonyl stretch v = 1 ground state of OHBA-F is consistent with an n,π* T_1 state in which the bond order of the carbonyl is reduced from two nearly to one and a half, corresponding to promotion of a non-bonding electron into an anti-bonding orbital centered on the carbonyl group.

There is however intensity (approximately ~44% of the total emission intensity) for emission into excited vibrational states of modes other than the carbonyl stretch, indicative of some participation by the remainder of the π* system in the chromophore. Built onto the carbonyl stretch progression are secondary peaks which can be grouped by their patterns of intensity and frequency location (see Table IV and Figure 7). The lowest frequency secondary progression appears 199, 225, 251, and 292 cm^{-1} from the v = 0, 1, 2, and 3 peaks, respectively, and may be associated with a torsional mode. The next major features occur 852, 839 and 828 cm^{-1} from the v = 0, 1, and 2 carbonyl peaks, respectively, and can be associated with the 846 cm^{-1} infrared absorption, which has been assigned as an aromatic C-H out of plane bend strongly coupled to the aldehyde C-H out of plane motion[38]. Finally, there is a series of peaks located 1210, 1220, 1194, and 1179 cm^{-1} from the v = 0, 1, 2 and 3 peaks, which can be associated with either the 1211 cm^{-1} OH in-plane bend or the 1244 cm^{-1} phenolic C-O stretch.

OHBA-F, S_1. Absorption into the S_1 state of OHBA-F has been identified as an n,π* transition by its low extinction coefficient. A repeating pattern (see Figure 6) of doublets is observed at 377.8, 374.4 nm; 359.8, 356.6 nm; and 343.4, 341.0 nm (see Table IV and Figure 6). The 1324 and 1353 cm^{-1} distance between the long wavelength peaks in the doublets can be assigned to the excited state carbonyl stretch frequency in light of the pattern observed in the companion T_1 n,π* transition, and the similar excited state frequencies observed for benzaldehyde.[36] The considerable intensity of the shorter wavelength peaks of the doublets (374.4, 356.6, and 341.0 nm; 240, 249 and 205 cm^{-1} higher than the 377.8, 359.8 and 343.4 nm peaks, respectively) indicates considerable participation of the rest of the π system in the chromophore. The other major progression is a series of peaks at 367.6, 350.2, 335.2 and 321.2 nm, located 734, 762, 687 and (687 + 1300) cm^{-1}, respectively, above the primary carbonyl progression peaks. Without isotopic substitution these progressions cannot be assigned with confidence, but the 240 cm^{-1} progression may be an aldehyde group wag mode, which has a frequency of 247 cm^{-1} in the S_1 n,π* state of benzaldehyde[36], or an O-H torsional mode, as ground state O-H torsional modes of non-hydrogen-bonded substituted phenols are in the region of 300 cm^{-1}.[39] The 734 cm^{-1} progression may then correspond to the 844 cm^{-1} out of plane C-H combination band detected in the phosphorescence spectrum.

OHBA-F, S_2. The S_2 transition of OHBA-F, identified as π,π* by its extinction coefficient which is similar to the 3600 M^{-1}cm^{-1} value for OHBA-C (Figure 5), also has clearly defined vibrational structure. Identification of its π,π* character is furthered by the large (520 cm^{-1}) shift in the 0-0 transition in xenon matrix, as compared to the 80 and 40 cm^{-1} shifts observed for the T_1 and S_1 states, respectively. The xenon matrix, with its greater polarizability, tends to stabilize the more polar excited state formed upon excitation of an electron to the more diffuse π,π* orbital, thereby yielding a red-shifted transition.[15] There is however no easily identifiable repeating pattern in the vibrational structure of OHBA-F's S_2 absorption, as the spectrum becomes very congested 1400 cm^{-1} above the assigned 0-0 peak. The 305.8 nm absorption, 813 cm^{-1} above the 0-0 transition, may be repeated 834 cm^{-1} higher at 298.2 nm. Likewise, the 301.2 nm absorption, 1313 cm^{-1} above the 0-0 energy, may be repeated 1211 cm^{-1} higher at 290.6 nm. The 1313 cm^{-1} vibration could be associated with π,π* excitation of the carbonyl with somewhat greater participation of the rest of the π system than in S_1, and the 813 cm^{-1} may be associated with the 846 cm^{-1} feature observed in the phosphorescence spectrum. Again, more definite assignment awaits detailed work with isotopic substitution.

OHBA-C. In contrast to the excitation and emission spectra of OHBA-F, those of OHBA-C are almost entirely lacking in vibrational structure and have very low intensity in the region of the 0-0 energy. By way of another comparison, benzaldehyde has a prominent 0-0 absorption band at 371.5 nm[40], and displays highly structured emission from both its S_1 and T_1 n,π* states. The lack of observable structure in the emission spectrum in argon matrix can be accounted for by the large changes in geometry suggested for the excited state, which tends to blur vibrational structure due to the increased density of states, while the π,π^* proton transfer state proposed for S_2 might be expected to have even less structure, in that charge transfer states are typically broad and featureless. Vibrational structure has however been detected in excitation and absorption spectra of the closely related molecule o-hydroxyacetophenone.

METHYL SALICYLATE

0-0 Energies and Ground States of MS-C and MS-E

Figure 24 is a summary of the 0-0 energies measured for MS in SF_6 matrix, as presented in Table Xa. In this instance the reaction coordinate is most easily described by an angle of ester rotation Θ, although any rotation of this group would presumably also result in motion of the hydroxyl group coupled to it by the intramolecular hydrogen-bond. The fluorescence of each of the two forms is an indication of two minima in S_1, and hence a barrier in this state. The 0-0 transitions of the two forms are offset by the ground state ΔH value, which has been estimated at 2.5 ± 0.6 kcal/mole[41] from the reservoir temperature dependence of the two fluorescence intensities in free jet expansions. Others have measured ΔH as high as 4.0 kcal/mole from the fluorescence intensities in static methyl salicylate gas.[42] The lower enthalpy change seems more reasonable in comparison to that for OHBA, as a weaker but still significant hydrogen bond is formed in MS-E, indicated by the 3450 cm^{-1} OH stretch.

Excited State Barriers

Due to the non-reversibility and the slow photolysis rate for MS, it was

Figure 24. Summary of 0-0 energies obtained for MS-C and MS-E in 12K SF_6 matrix by absorption, excitation, and emission spectroscopy.

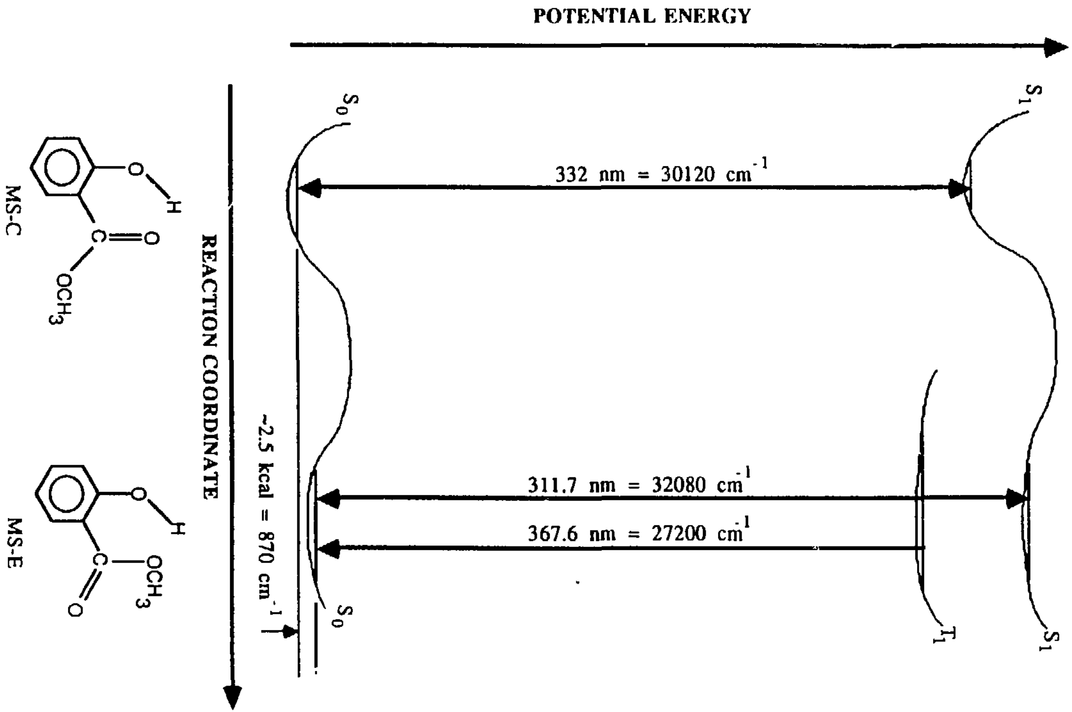
POTENTIAL ENERGY
REACTION COORDINATE
S_0
S_1
S_0
T_1
S_1
332 nm = 30120 cm^{-1}
311.7 nm = 32080 cm^{-1}
367.6 nm = 27200 cm^{-1}
~2.5 kcal = 870 cm^{-1}
MS-C
MS-E
O
H
C
OCH$_3$

not possible to measure the wavelength dependence of the photolysis quantum yield in the same manner as for OHBA, other than to note that photolysis of MS-C did proceed upon excitation at 333 nm in SF_6, at the long wavelength edge of the S_1 0-0 transition where there is presumably also some overlap with a triplet state. However, examination of the vibrational structure in the excitation and absorption spectra can once again provide an indication of an excited state barrier.

The vibrational structure in the S_1 absorption spectrum of MS-C in xenon (Figure 14) is well-defined only up to 309.1 nm, 7.6 kcal above the 0-0 transition wavelength. This energy does not correspond to the height of the barrier on the S_1 surface, as it is 5.1 kcal below the S_1 0-0 energy of MS-E. Thus, any information on the S_1 barrier in methyl salicylate must come from the excitation and absorption spectra of MS-E. Previous workers[43,27] have noted an onset to a non-radiative decay channel in MS-C, located 1300 cm^{-1} above the S_1 0-0 energy, higher in energy than that proposed for OHBA-C[34]. This non-radiative decay channel has the effect of both rapidly blurring the vibrational structure, and of lowering the lifetime in jets from the 12 nsec lifetime at excess energies up to 1300 cm^{-1}, to 160 psec with 1800 cm^{-1} of excess energy. It has been proposed that this non-radiative decay channel is perhaps intersystem crossing to a triplet state.

The fluorescence excitation spectrum of MS-E in SF_6 has vibrational structure which abruptly ends 1610 cm^{-1}, or 4.6 kcal, above its 0-0 transition wavelength. Addition of the 1610 cm^{-1} to the 32080 cm^{-1} $S_0 \rightarrow S_1$ 0-0 energy and the 870 cm^{-1} ΔH value leads to placement of the S_1 barrier to reaction at 34560 cm^{-1} above MS-C's ground state, or 4440 cm^{-1} (12.7 kcal) above MS-C's S_1 0-0 energy. Again, the assumption implicit is that the loss of vibrational structure in MS-E's absorption spectrum indicates the S_1 barrier to formation of MS-C, rather than to unbound motion in another coordinate. Rotation of the hydroxyl group alone must be considered an energetically accessible motion. However, hydroxyl torsion results in repulsive interaction between the ether and phenol oxygen non-bonding electrons, so rotation of the ester group is again implicated.

The S_1 states of both MS-C and MS-E are π,π^*, judging from the extinction coefficients and from the significantly shortened fluorescence lifetime of MS-C in xenon. The S_1 state of MS-C might then be expected to resemble the S_2, π,π^* proton-transfer state of OHBA-C. The zwitterionic excited state would have a strong hydrogen-bond, and thus a large barrier to formation of MS-E on the S_1 surface. The 12.7 kcal barrier proposed here is compatible with this. The significant difference between this and the 17.7 kcal proposed for OHBA-F's S_2 barrier may be a result of the electronic differences between esters and aldehydes. One additional contrast between the π,π^* S_2 state of OHBA-C and the π,π^* S_1 state of MS-C is that vibrational structure is present in the absorption spectrum of MS-C. It was argued that no vibrational structure is expected with a charge-transfer state, so that of MS-C's S_1 transition provides an interesting point of discussion.

The 4.6 kcal excited state barrier to formation of S_1 MS-C is consistent with the 5.5 kcal/mole ground state barrier for the conversion of MS-E to MS-C, measured by ultrasonic absorption and sound velocity dispersion techniques[22], and very close to the 4.0 kcal barrier determined for the analogous process in the S_2 state of OHBA-F. The conclusion from these data is that there is little if any hydrogen-bonding in the excited state of MS-E. This is not too surprising, since π,π^* excitation increases the basicity of a carbonyl oxygen and decreases the basicity of the methoxy group. Thus, the already weak hydrogen-bond present in the ground state of MS-E is diminished in the excited state, and can not be expected to take on the charge transfer character evident in MS-C and OHBA-C's S_2 states. This analysis is confirmed by the the fluorescence excitation and emission spectra of MS-E, which display strong 0-0 transitions, consistent with an excited state structurally similar to the ground state. A spectroscopically generated map of the lowest energy electronic states of MS-C is presented in Figure 25.

Reaction Pathways Below the S_1 Barrier

Since photolysis of MS-C proceeds with excitation at the S_1 0-0 energy, as with OHBA-C, a ground state or triplet state is again implicated. It is difficult to ascertain which of these two possible states forms the reaction pathways without more precise measurements of the reaction rates in different matrices. Clearly, the size of the matrix cage is important, as the reaction proceeds more rapidly in SF_6 than in argon. SF_6 has a van der Waals radius of about 3.0 Å (the sum of an S-F bond (1.58 Å[44]) plus the 1.4 Å van der Waals radius of fluorine[45]), which is significantly larger than argon, whose van der Waals radius is 1.9 Å.[45] This clouds the issue of whether or not a triplet state is involved, since the heavy atom matrix of xenon, in which photolysis also appears to be faster, also has a larger cage size than argon. Xenon's van der Waals radius is 2.2 Å. One might expect, if it is only a cage size effect, that MS-C would photolyze much more rapidly in SF_6 than in xenon, but as the photolysis rates are comparable, the triplet state is tentatively implicated. Resolution of this issue demands careful kinetics studies in which the UV absorption is known and the scattering of the highly polarizable xenon is controlled. However, as with OHBA-C, there is no detectable phosphorescence of MS-C, and the T_1 state of the product MS-E is lower in energy by 5.9 kcal than the S_1 state of MS-C. Thus, as with reaction from OHBA-C, reaction on a low barrier triplet surface is

Figure 25. Map of the lower energy electronic states of MS-C and MS-E derived from absorption, excitation and emission spectra in 12K SF_6 matrix.

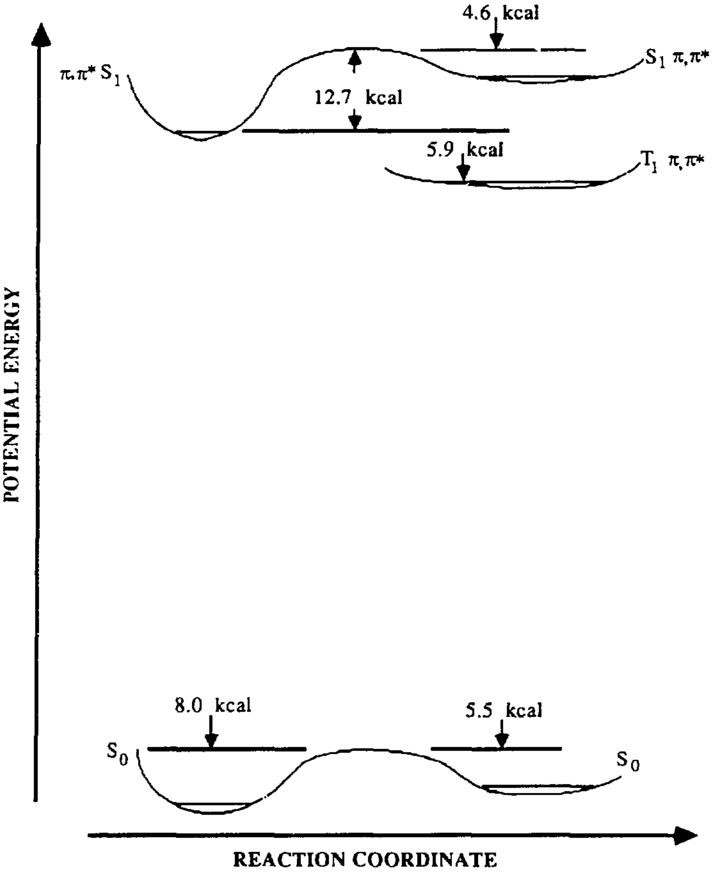
4.6 kcal
S1 π,π*
π,π* S1
12.7 kcal
5.9 kcal
T1 π,π*
POTENTIAL ENERGY
8.0 kcal
5.5 kcal
S0
S0
REACTION COORDINATE

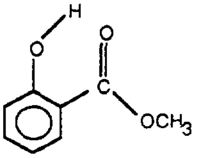
H
O
O
C
OCH3

MS-C

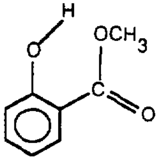
H
O
OCH3
C
O

MS-F

energetically feasible.

Curiously, the reverse photolysis from MS-E to MS-C, unlike that for OHBA-F to OHBA-C, is not readily effected. It has previously been noted that MS efficiently converts electronic energy into vibrational energy, making it useful as a fiber and polymer protection agent[18]. Conceivably, the 0.5 to 1.0 mWatt powers used to photolyze MS-E were too great, and resulted in local heating induced sample sublimation. Loss of SF_6 matrix material was in fact apparent with some attempts at the reverse photolysis.

This does not however account for the appearance of CO and CO_2 with the photolysis of MS-C and MS-E. Further work with the wavelength and matrix dependence of the formation of CO and CO_2, and with photolysis powers at low levels so as to trap the other products, is required to resolve these issues.

Distortion and Displacement in the Excited States of MS

Vibrational structure of MS-C and MS-E's electronic spectra is quite different from that of OHBA-C and OHBA-F's. Again, each excited state will be discussed separately.

MS-E T_1. The phosphorescence spectrum of MS-E (Figure 19, Curve B and Table IXb) is much more congested than that of OHBA-F, and furthermore has a very different lifetime (2.3 seconds in SF_6, versus the 2.1 msec for OHBA-F in argon). As π,π^* states generally have less localized excitation and longer phosphorescence lifetimes than n,π^* states[15], the T_1 state of MS-E can be assigned as a π,π^* state with confidence.

Since few of the IR bands of MS-E (Table VIII) have been assigned at this point, it is difficult to identify all the peaks in the phosphorescence spectrum. However, the peak at 379.0 nm, 784 cm^{-1} above the 0-0 energy, may correspond to the 797.3 cm^{-1} ground state vibrational absorption, and furthermore may be part of a progression including the 389.5 nm band located 806 cm^{-1} higher still in energy. Like the 846 cm^{-1} vibration observed in the phosphorescence spectrum of OHBA-F, the 806 cm^{-1} frequency probably corresponds to a C-H out of plane motion. As the IR spectrum shows no major band near 1327 cm^{-1}, the 383.0 nm feature probably arises from a combination of vibrations, while the 1625 cm^{-1} IR band may easily be associated with the 1638 cm^{-1} peak at 395.0 nm, which is found again 1591 cm^{-1} higher at 421.5 nm. This 1625 cm^{-1} band is probably an aromatic ring stretching motion. These assignments are tentative, but point towards distortions of the entire π system in this T_1 state, consistent with a π,π^* assignment.

MS-E, S_1. The fluorescence emission (Figure 18, Curve B) has no bands which can be easily matched to any absorptions in the IR spectrum, so it must be concluded that the observed structure corresponds to combinations of lower frequency vibrations and internal rotations. The fluorescence excitation spectrum of MS-E (Figure 18, Curve A), with its apparent mirror-image structure, likewise cannot be interpreted at this spectral resolution. In fact, the fluorescence excitation spectrum of MS-E in supersonic jets has previously been observed and its vibrational structure assigned.[41] These workers report a number of bands which correspond to combinations which include one or more of the 144, 172, 180, or 187 cm^{-1} low frequency modes.

MS-C, S_1. A striking aspect of the absorption spectrum of MS-C (Figure 15) is the closely-spaced bands, situated 160-200 cm^{-1} apart. These presumably arise from combinations which include one or more of the 176, 347, 372, and 424 cm-1 bands detected in the gas phase excitation spectrum[41]. The ground state counterparts of such bands do not appear in the emission spectrum 1 nm resolution in SF_6 or xenon, but have been observed as a 180

cm^{-1} series in jet cooled spectra[43]. The major features which appear at the longer wavelengths, and which presumably arise from a combination of vibrational modes, are the same as those found in the jet cooled emission spectra. The extinction coefficient of this absorption, along with the heavy-atom responsive lifetime (10.5 nsec in argon, 3.0 nsec in xenon) indicates a π,π^* state.

In summary, electronic excitation of both MS-C and MS-E appears to activate torsional modes, particularly in the S_1 states. While this makes assignment of the modes active in the chromophore difficult at the resolution available in SF_6 or xenon matrix, it points to the large difference between the S_1 and T_1 states of OHBA and MS. The differences in the singlet and triplet lifetimes and vibrational structure of these two molecules provide *further evidence that* n,π^* *states not only couple more strongly to triplet* surfaces, even in the absence of a spin-orbit coupling matrix such as xenon, but also involve more localized excitation.

CHAPTER V. DMABN AND THE EXTERNAL HEAVY ATOM EFFECT

INTRODUCTION

Atoms of high nuclear charge are known to increase rates of spin-forbidden processes, both as components of the solvent (the external heavy atom effect) and as substituents on the molecule of interest itself (the internal heavy atom effect).[46] A number of studies[4-7] have shown that branching ratios of photochemical reactions in cryogenic rare gas matrices of argon or krypton can be altered by directing reactants to the triplet state with a heavy atom matrix such as xenon. As discussed in the previous chapter, the external heavy atom effect can also be exploited to identify the spin state of a particular reaction pathway, in that enhancement of the reaction rate relative to rates of other decay processes, such as alternate reactions or fluorescence, can serve to identify the triplet nature of a reaction surface.

This work is aimed at quantifying the effects of rare gas external heavy atoms on rates of spin-forbidden processes. While heavy atom effects on fluorescence and phosphorescence yields (Φ_f and Φ_p, respectively), and on phosphorescence lifetimes[47] (τ_T) have been observed before, few attempts have been made to determine the heavy atom effects on individual rate constants. Based on relative fluorescence and phosphorescence yields and singlet and triplet lifetimes of the molecule DMABN, pictured below, isolated in argon, krypton and xenon, the increase in k_{isc} (the rate constant for intersystem crossing to the triplet state), k_p (the rate constant for phosphorescence), and k_{qp} (the rate constant for non-radiative decay from the triplet state) in these rare gas heavy atom matrices is modelled for this compound.

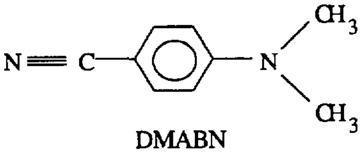

DMABN

An estimate of the effect of a single heavy atom placed in the vicinity of DMABN is obtained from fluorescence and phosphorescence lifetimes of this molecule in argon matrices doped with small amounts of krypton and xenon

The high intensity and well-resolved features of DMABN's fluorescence and phosphorescence make it a suitable subject for a study of the external heavy atom effect. Furthermore, DMABN presents another interesting case for excited state mapping. It has been the focus of much attention since Lippert et al.[48] discovered that it exhibits dual fluorescence in polar room temperature solutions. The long wavelength "anomalous" fluorescence is thought to originate from a state in which the amino methyl groups are twisted from a position syn to the aromatic plane to a position anti, with an accompanying transfer of charge from the amino to the nitrile group.[49] Thus, DMABN, like OHBA and MS, has two minima in its S_1 excited state. The well-resolved fluorescence and phosphorescence spectra obtained in the cryogenic matrices, along with the excited state lifetimes, allow for a discussion of the contours of the excited state potentials of this molecule.

RESULTS

Intensities and Lifetimes in Pure Rare Gas Matrices.

Figure 26 illustrates the increased phosphorescence and the decreased fluorescence observed in the heavy atom matrices of krypton and xenon. The intensity, but not the ratio of fluorescence and phosphorescence, in all three rare gas matrices was highly sensitive to annealing, roughly doubling with the annealing process. Matrices (optically thick at the wavelength of

Figure 26. Emission spectra of DMABN in argon (lower), krypton, and xenon (upper) matrices at 12K (1 nm resolution, λ_{ex}=280 nm).

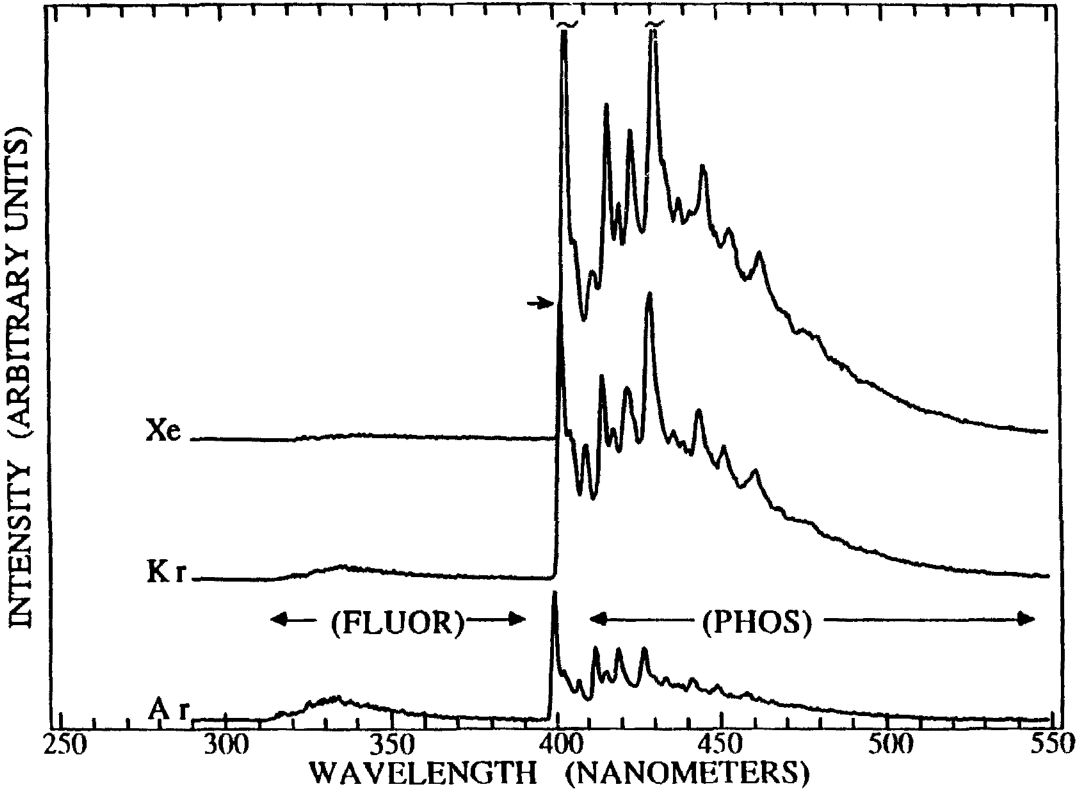
INTENSITY (ARBITRARY UNITS)
Xe
Kr
Ar
(FLUOR)
(PHOS)
250
300
350
400
450
500
550
WAVELENGTH (NANOMETERS)

excitation) were deposited at 12K for argon, 20K for krypton, and 30K for xenon, annealed at a higher temperature for a period of about 15 minutes and then cooled to 12K for recording of emission spectra. The annealing process was repeated, with one to two degree increments in the annealing temperature, until a maximum integrated emission intensity was observed. These maximum annealing temperatures were 38K, 50K, and 70K for Ar, Kr, and Xe matrices, respectively. Beyond this temperature, loss of the matrix, indicated by an increase in pressure, resulted in a change in shape of the emission and an overall loss in intensity as the DMABN ceased to be matrix isolated. Both the shift to longer wavelength (λ_{max} = 380 nm) and the decrease in intensity have been observed for aggregates in the gas phase.[50] Diffusion may occur prior to the loss of the matrix, but it is not thought to play an important role with this large molecule. This view is supported by the observation that the shape of the emission remains quite constant until the matrix gas sublimes.

The fluorescence and phosphorescence quantum yields (Φ_f's and Φ_p's, respectively) listed in Table XI are for such carefully annealed, optically thick matrices, and are given relative to the phosphorescence yield in xenon. The ratios of phosphorescence to fluorescence given in Table XI for the three rare gas matrices are averages from a sampling of more than six matrices. This ratio was independent of optical thickness and sample preparation as long as oxygen was rigorously excluded. Addition of oxygen decreased total emission intensity, with a larger effect on phosphorescence.

Both the singlet and triplet lifetimes decreased in the heavier atom matrices of krypton and xenon. The triplet lifetimes (τ_T) in argon, krypton and xenon are given in Table XI, as well as singlet lifetimes (τ_S) in argon and krypton. The emission intensity was too low and the lifetime too short to

Table XI. Measured emission yields (relative to phosphorescence yield in xenon), ratios of phosphorescence to fluorescence yields, and singlet and triplet lifetimes of DMABN in argon, krypton and xenon.

	Ar	Kr	Xe
Φ_p (relative phosphorescence quantum yield)	.17±.05	.5±.1	(1.00)
Φ_f (relative fluorescence quantum yield)	.035±.005	.020±.003	.011±.003
Φ_p/Φ_f	4.8±.5	25±3	90±20
τ_T (seconds)[a]	3.5±.2	.9±.1	.07±.0
τ_S (nanoseconds)[b]	3.2±.2	1.5±.8	-

(a) Lifetimes determined at several wavelengths throughout the phosphorescence region.

(b) Lifetimes measured by selecting fluorescence emission with a Corning 7-37 filter, which passes light between 310 and 390 nm.

permit a measurement of the singlet lifetime in xenon.

The results of Table XI can be used to calculate the magnitudes of the individual rate constants k_{isc}, k_p and k_{qp}, whose corresponding processes are sketched in Figure 27. k_{isc} is the rate constant for intersystem crossing from S_1 to T_1, k_p is that for phosphorescence from T_1, k_{qp} is that for radiationless decay from T_1, k_f is that for radiative decay from S_1, and k_{qf} is the rate constant for radiationless decay from S_1. Calculation of the rate constants for the spin-forbidden processes is possible with the following four assumptions:

1. The phosphorescence quantum yield in xenon is unity.
2. k_{qf} is small in comparison to k_{isc}.
3. k_f is independent of the matrix.
4. The amount of light absorbed is the same in all three matrices.

These assumptions are justified as follows:

1. The phosphorescence quantum yield of DMABN in polyvinyl alcohol matrices at 80K has been measured at about 0.8,[51] and can be expected to be similarly high in a 12K rare gas matrix.

2. The high ratios of phosphorescence to fluorescence, even in argon, point to k_{isc} playing a large role in relaxation from S_1 in all three matrices.

3. k_f is thought to depend on the refractive index of the medium, but there is no consensus as to the form of this dependence. Various estimates are that k_f is proportional to n, n^2 or n^3,[52] or even $n(n^2+2)^2$.[53] For these calculations only k_{isc} has any explicit dependence on k_f, being directly proportional to k_f. With n equal to 1.27, 1.34, and 1.49 in argon[54], krypton[54], and xenon[53], respectively, the values for k_{isc} given in Table XII would increase by factors of 1.05 and 1.17 in krypton and xenon for an n

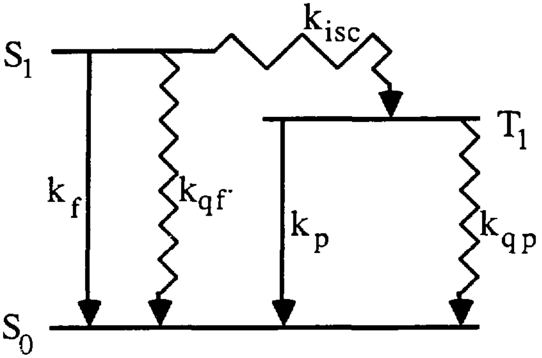

Figure 27. Jablonski diagram illustrating radiative (straight lines) and non-radiative (zigzag lines) processes considered.

Table XII. Calculated values for k_f, k_{isc}, k_p, and k_{qp} in argon, krypton and xenon matrices.

	Ar	Kr	Xe
k_f (second^{-1})	$1.1\pm0.2\times10^{7}$ [a]		
k_{isc} (second^{-1})[b]	$3.0\pm0.2\times10^{8}$	$5.4\pm1.9\times10^{8}$	$9.8\pm4.6\times10^{8}$
$k_{isc}/k_{isc}(Ar)$	(1)	1.8±0.8	3.3±1.8
k_p (second^{-1})	.050±.018	.57±.18	14.4±4.2
$k_p/k_p(Ar)$	(1)	11.4±7.6	290±190
k_{qp} (second^{-1})	.23±.03	.54±.18	(0)
$k_{qp}/k_{qp}(Ar)$	(1)	2.3±1.0	(0)

(a) Uncertainties reflect only those propagated by the measurements listed in Table XI, and do not include the uncertainty from the three assumptions that Φp in xenon is unity, $k_{isc} \sim k_{isc} + k_{qf}$, or that k_f is matrix independent.

(b) Based on the assumption that $(k_{isc} + k_{qf}) \sim k_{isc}$.

dependence, while for an $n(n^2+2)^2$ dependence the calculated value for k_{isc} in krypton and xenon would be higher by factors of 1.16 and 1.60, respectively. The value of k_{isc} calculated for argon matrix has no dependence on n, since for this matrix the singlet lifetime has been measured directly.

4. A UV spectrum of DMABN isolated in xenon at 12K (optically thick at 280 nm) showed that less than 10% of the light attenuation was caused by scattering. Similar optically thick krypton and argon matrices would be expected to scatter even less light.

The calculations of the rate constants proceed as follows: Φ_f, equal to $k_f(k_f + k_{qf} + k_{isc})^{-1}$ and Φ_p, equal to $k_{isc}(k_f + k_{qf} + k_{isc})^{-1} \cdot k_p(k_p + k_{qp})^{-1}$, are measured relative to Φ_p in xenon, which is set at unity. Combining Φ_f with the measured singlet lifetime in argon, equal to $(k_f + k_{qf} + k_{isc})^{-1}$, k_f in argon is obtained as Φ_f/τ_S. The uncertainty in the measured singlet lifetime in krypton is too great to permit a similar calculation of k_f in that matrix, but the nominal value of 1.3×10^7 second^{-1} compares favorably with the value of 1.1×10^7 second^{-1} in argon matrix. Assuming k_f in krypton and xenon is the same as in argon, singlet lifetimes can be calculated as $\Phi_{f(Kr,Xe)} \cdot \tau_{S(Ar)}/\Phi_{f(Ar)}$, which are 1.8 and 1.0 nanoseconds in krypton and xenon, respectively. Again with the assumption that k_f is invariant with the matrix, $(k_{isc} + k_{qf})$ is separable from Φ_f in each of the three matrices.

Since $\Phi_p/\tau_S \cdot k_{isc} = k_p \cdot (k_p + k_{qp})^{-1}$, and $(k_p + k_{qp})^{-1}$ is the measured triplet lifetime, k_p can be calculated if a value of k_{isc} can be obtained. For this calculation, it is assumed that k_{qf} is sufficiently small that $(k_{isc} + k_{qf}) \sim k_{isc}$. The values for k_{isc} given in Table XII are obtained with this assumption. Using these values for k_{isc}, the calculated values for τ_S and the measured values for the phosphorescence quantum yield and lifetime, the values of k_p, and then, k_{qp} given in Table XII are calculated.

Excited State Lifetimes in Mixed Matrices

Both singlet and triplet decay rates of mixed argon:xenon matrices were measured, as well as triplet decay rates of mixed argon:krypton matrices. Argon:(heavy atom) ratios were in the range of 66 to 400, which, assuming 35 nearest neighbor positions around fully isolated DMABN[55], implies that statistically between 60 and 92 percent of the DMABN molecules will have no heavy atom nearest neighbors and virtually all the rest will have only one heavy atom nearest neighbor.

Whereas the decays of DMABN in the pure matrices could be fit with a single exponential decay, the mixed matrices required the addition of a second component to achieve the same level of fit. The mixed matrix decays could be fit as the sum of two exponentials, one with a long lifetime matching that of DMABN in pure argon and the other with a short lifetime intermediate between the lifetime of DMABN in pure argon and that in the pure heavy atom matrix. Average values of the heavy-atom shortened lifetimes are given in Table XIII. The lifetime and coefficient of the second component showed no wavelength dependence throughout the phosphorescence region.

Figure 28 shows a decay and fit parameters for phosphorescence decay of DMABN in a pure Ar matrix (single exponential fit) and in a 203:1 Ar:Xe matrix (double exponential fit). Figures 29A and 29B show a single exponential fit of the fluorescence decay in pure argon matrix and a double exponential fit of a 66:1 Ar:Xe matrix, respectively, along with the instrument response function and weighted residuals.

High Resolution Spectra

The phosphorescence excitation (Curve A, λ_{em} = 427 nm, .4 nm

Table XIII. Lifetimes of fast and slow components of mixed matrix emission decays, and lifetimes in corresponding pure heavy atom (krypton or xenon) and argon matrices.

	fast	pure heavy atom	slow	pure Ar
τ_S, Ar:Xe matrices (nanoseconds)	1.3±0.4	(1.0, calculated)	3.2±0.4	3.2±0.2
τ_T, Ar:Xe matrices (seconds)	0.3±0.1	.07±0.02	3.5±0.3	3.5±0.2
τ_T, Ar:Kr matrices (seconds)	1.3±0.2	0.9±0.1	3.5±0.3	3.5±0.2

Figure 28. Phosphorescence decays of DMABN in argon (lower trace) and 203:1 argon:xenon (upper upper) matrices, λ_{em}=427 nm. Lifetime for single exponential fit of pure argon matrix is 3.62 seconds. Fitted lifetimes and relative coefficients of 203:1 argon:xenon matrix are 3.50 seconds (relative coefficient = 0.88), and 0.42 seconds (relative coefficient = 0.12). Assuming 35 nearest neighbors, DMABN will have 84% with no xenon nearest neighbors, 14% with one, and 2% with two or more.

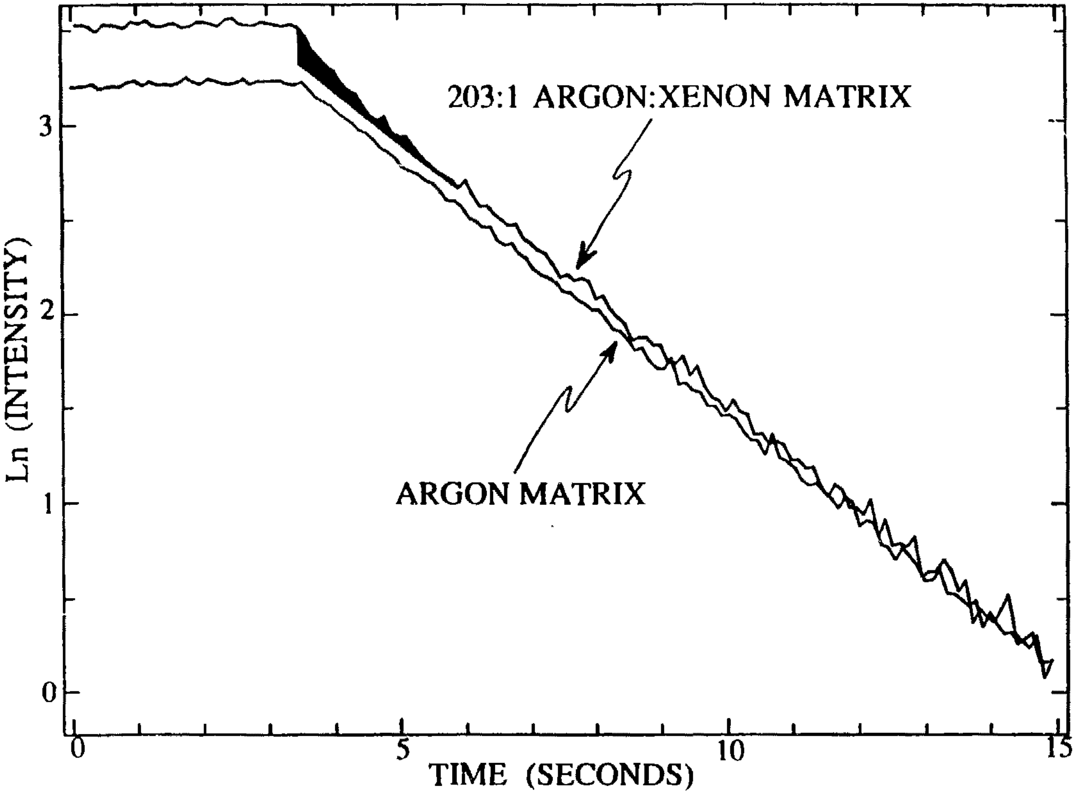

203:1 ARGON:XENON MATRIX
ARGON MATRIX
Ln (INTENSITY)
TIME (SECONDS)
0
1
2
3
0
5
10
15

Figure 29A. Lower: fluorescence decay (310-390 nm), instrument response function, and single exponential fit (τ=3.2 nanoseconds) for DMABN in argon. Upper: weighted residuals ($R\chi^2$ = 3.1).

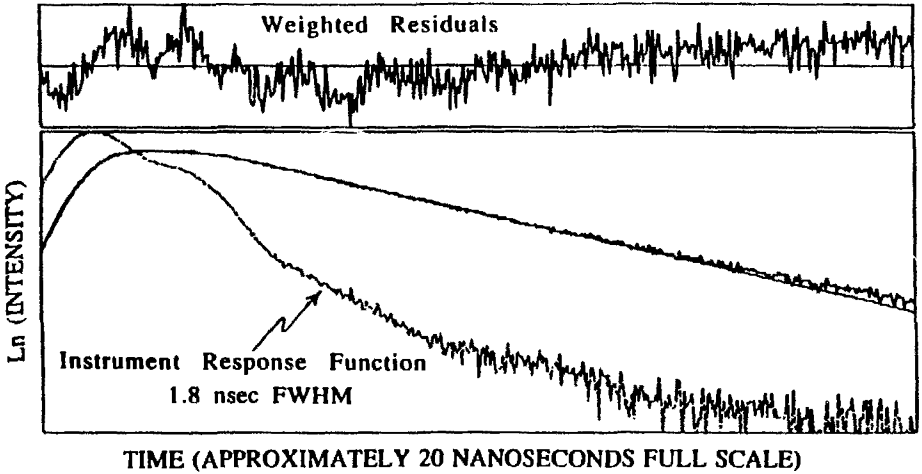
Weighted Residuals
Ln (INTENSITY)
Instrument Response Function
1.8 nsec FWHM
TIME (APPROXIMATELY 20 NANOSECONDS FULL SCALE)

Figure 29B. Lower: fluorescence decay (310-390 nm), instrument response function, and double exponential fit for DMABN in argon:xenon 66:1 matrix. Fitted lifetimes are 3.4 nanoseconds (relative coefficient = 0.51) and 1.2 nanoseconds (relative coefficient = 0.49), respectively. Assuming 35 nearest neighbors, DMABN will have 59% with no xenon nearest neighbors, 31 percent with one, and 10% with two or more. Upper: weighted residuals ($R\chi^2 = 2.4$).

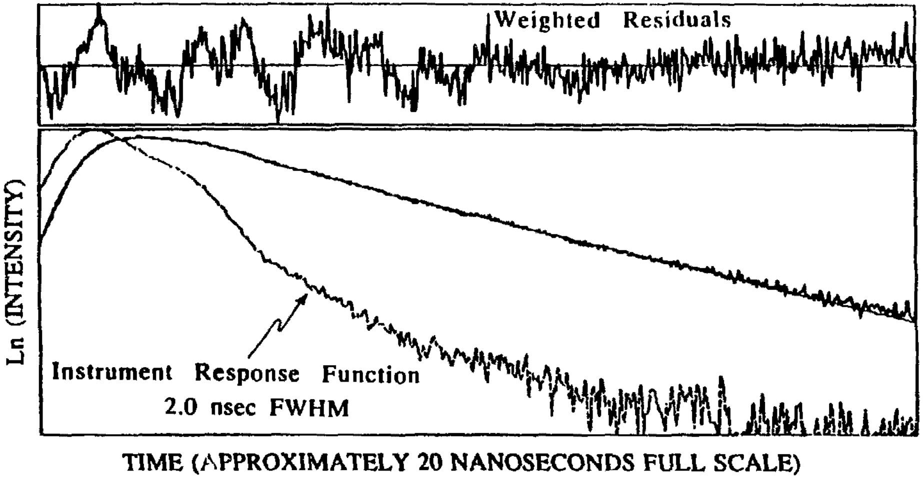
Weighted Residuals
Ln (INTENSITY)
Instrument Response Function
2.0 nsec FWHM
TIME (APPROXIMATELY 20 NANOSECONDS FULL SCALE)

excitation bandpass) and fluorescence emission (Curve B, λ_{ex} = 280 nm, .1 nm emission bandpass) spectra of DMABN in argon are given in Figure 30. Figure 31 is a phosphorescence emission (bandpass = 0.1 nm) spectrum in krypton. Table XIV lists peak maxima in nanometers and peak-to-peak distances from the 0-0 transition in wavenumbers. Table XIVa gives the phosphorescence excitation vibrational progression in argon, Table XIVb the fluorescence emission vibrational progression in argon, and Table XIVc that for the phosphorescence emission in krypton.

Energies of the S_1 and T_1 transitions in argon, krypton, xenon and acetonitrile are given in Table XV. S_1 energies in argon, krypton, and acetonitrile were determined from excitation and emission spectra. The $S_0 \rightarrow S_1$ 0-0 transition energy in xenon matrix was determined from a phosphorescence excitation spectrum. The $S_0 \rightarrow T_1$ 0-0 transition energies in argon, krypton, xenon and acetonitrile matrices listed in Table XV are the frequencies at half height of the leading peaks in the emission spectra.

Polar Matrices

Shown in Figure 32 is the fluorescence excitation and the emission spectrum of DMABN in acetonitrile. A similar spectrum was recorded for DMABN in ammonia. Such virtually structureless spectra were also obtained even with annealing for thirty minutes at half the matrix melting point. The observed single exponential lifetime at both 410 and 440 nanometers was 2.4 seconds in acetonitrile.

Photolysis of DMABN

After one hour of photolysis with an unfiltered 100 watt medium pressure AH4 mercury lamp the steady state emission from DMABN isolated in argon matrix was virtually eliminated, leaving a tiny amount of structureless emission with a maximum of intensity at 420 nm and an

Figure 30. Curve A: Phosphorescence excitation (0.4 nm resolution, λ_{em} = 427 nm), and **Curve B:** fluorescence emission (0.1 nm resolution, λ_{ex} = 284 nm) of DMABN in argon matrix at 12K.

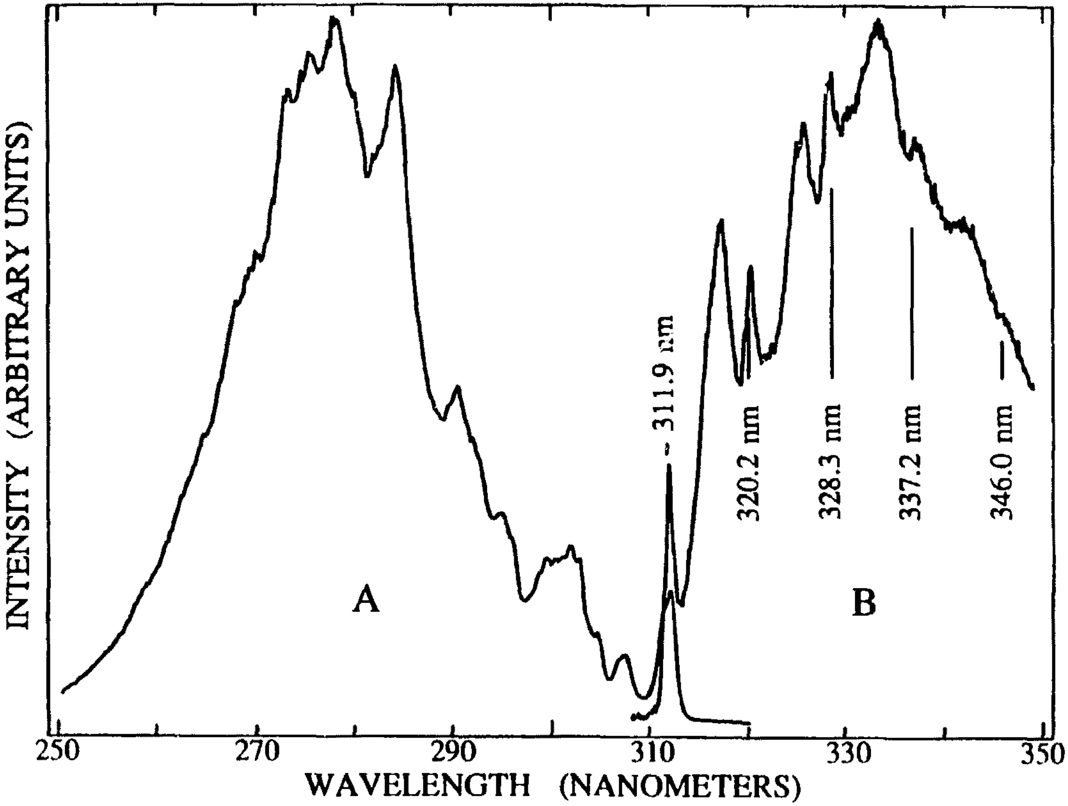
INTENSITY (ARBITRARY UNITS)
~ 311.9 nm
320.2 nm
328.3 nm
337.2 nm
346.0 nm
A
B
250
270
290
310
330
350
WAVELENGTH (NANOMETERS)

Figure 31. Phosphorescence of DMABN in krypton matrix at 12K (0.1 nm resolution, λ_{ex} = 284 nm).

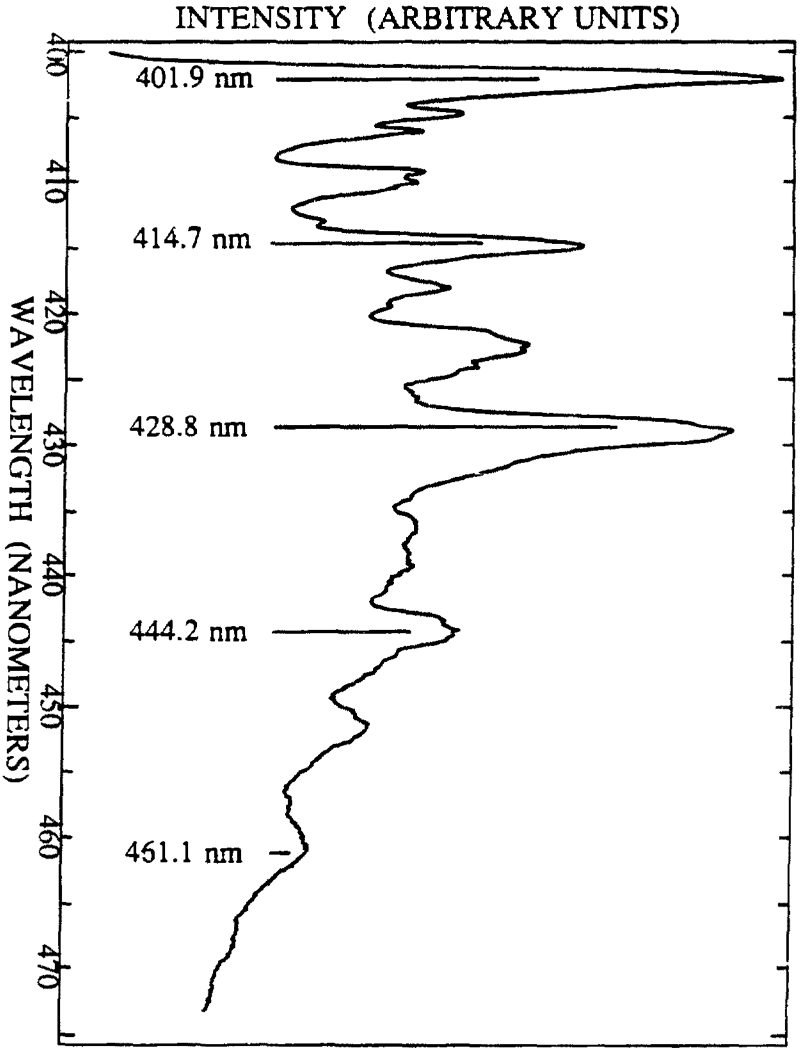
INTENSITY (ARBITRARY UNITS)
WAVELENGTH (NANOMETERS)
400
410
420
430
440
450
460
470
401.9 nm
414.7 nm
428.8 nm
444.2 nm
461.1 nm

Table XIV. Vibrational Progressions of DMABN: (a) phosphorescence excitation in argon (λ_{em} = 427 nm); (b) fluorescence emission in argon (λ_{ex} = 284 nm); and (c) phosphorescence emission in krypton (λ_{ex} = 284 nm).

a		b		c	
nm	cm^{-1}*	nm	cm^{-1}*	nm	cm^{-1}*
312.0	(0)	311.9	(0)	401.9	(0)
307.2	325	317.2	536	404.7	172
301.8	1083	320.2	831	406.0	251
294.6	1893	325.7	1358	409.1	438
290.4	2383	328.3	1602	409.9	486
284.2	3135	333.3	2058	412.9	663
278.2	3894	337.2	2406	414.7	768
275.4	4259	342.0	2822	418.0	958
273.0	4579	346.	3160	419.5	1044
269.6	5041			422.5	1213
				424.0	1297
				426.3	1424
				428.8	1561
				436.1	1951
				439.3	2118
				444.2	2369
				451.1	2714
				461.1	3194
				468.6	3542

*These values represent the peak-to-peak distance in energy from the assigned 0-0 peak.

Table XV. 0-0 Transition Energies of DMABN

Matrix	T_1[a]		S_1	
	nm	cm^{-1}	nm	cm^{-1}
Ar	399.2	25050±30	311.9	32060±20
Kr	401.1	24930±30	314.0	31850±20
Xe	403.1	24810±30	316.3	31610±30
CH_3CN	410.0	24390±50	324.0	30860±50
gas phase[b]			309.9	32265±15

(a) These values represents the frequency at half height of the leading peak.

(b) See ref. [50,56].

Figure 32. Curve A: Fluorescence excitation (1 nm resolution, λ_{em} = 349 nm) and **Curve B:** emission (1 nm resolution, λ_{ex} = 284 nm) of DMABN in acetonitrile matrix at 12K.

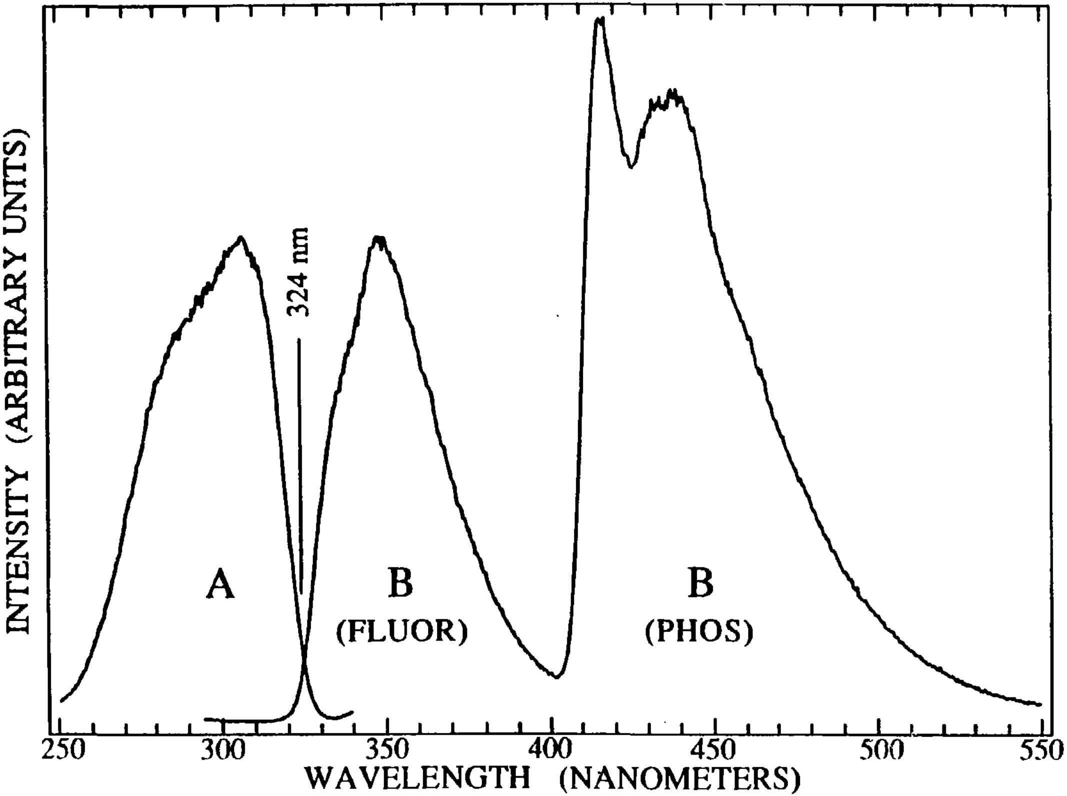
INTENSITY (ARBITRARY UNITS)
324 nm
A
B
(FLUOR)
B
(PHOS)
250
300
350
400
450
500
550
WAVELENGTH (NANOMETERS)

excitation maximum of 340 nm. The fluorimeter source was too weak to produce such a change during the course of the emission studies. Figure 33 is an FTIR difference spectrum of DMABN (negative features) and its photolysis product (positive features, after one hour of photolysis with a 1000 Watt Hg-Xe high pressure lamp through a CsI filter) in argon.

DISCUSSION

Heavy Atom Effects on Rates

The rate constants listed in Table XII reflect a much greater external heavy atom effect on the radiative rate constant k_p than on either of the non-radiative rate constants k_{isc} or k_{qp}. The majority of previous workers also found greater increases in k_p than in k_{qp}[57], both with halogenated solvents and paramagnetic ions, suggesting that the larger susceptibility of radiative transitions to increased spin-orbit coupling may in fact be general for the external heavy atom effect.

However, compared to some previous work, these results show a more pronounced difference in the effect on radiative rates than on non-radiative rates. For example, Siegel and Judeikis[58] measured triplet decays of naphthalene and perdeutero-naphthalene in glassy matrices by a combination of EPR and optical spectroscopies. Comparing naphthalene in glassy ethanol to a glassy 4:1 (by volume) mixture of ethanol with ethyl bromide or propyl bromide, they estimate a factor of five increase in k_p, a factor of 1.5 increase in k_{qp}, and a factor of three increase in k_{isc} in the heavy atom glasses. Why, in the present work, the nonradiative rate constants are relatively less sensitive is an interesting question. It should be noted that the DMABN $T_1 \rightarrow S_0$ 0-0 transition is very intense whereas the $S_1 \rightarrow S_0$ 0-0 transition is quite weak. Hence the T_1 and S_0 molecular

Figure 33. FTIR difference spectrum of DMABN in argon (negative features) and its photolysis product (positive features, one hour photolysis with a 1000 W Hg-Xe lamp through a CsI filter).

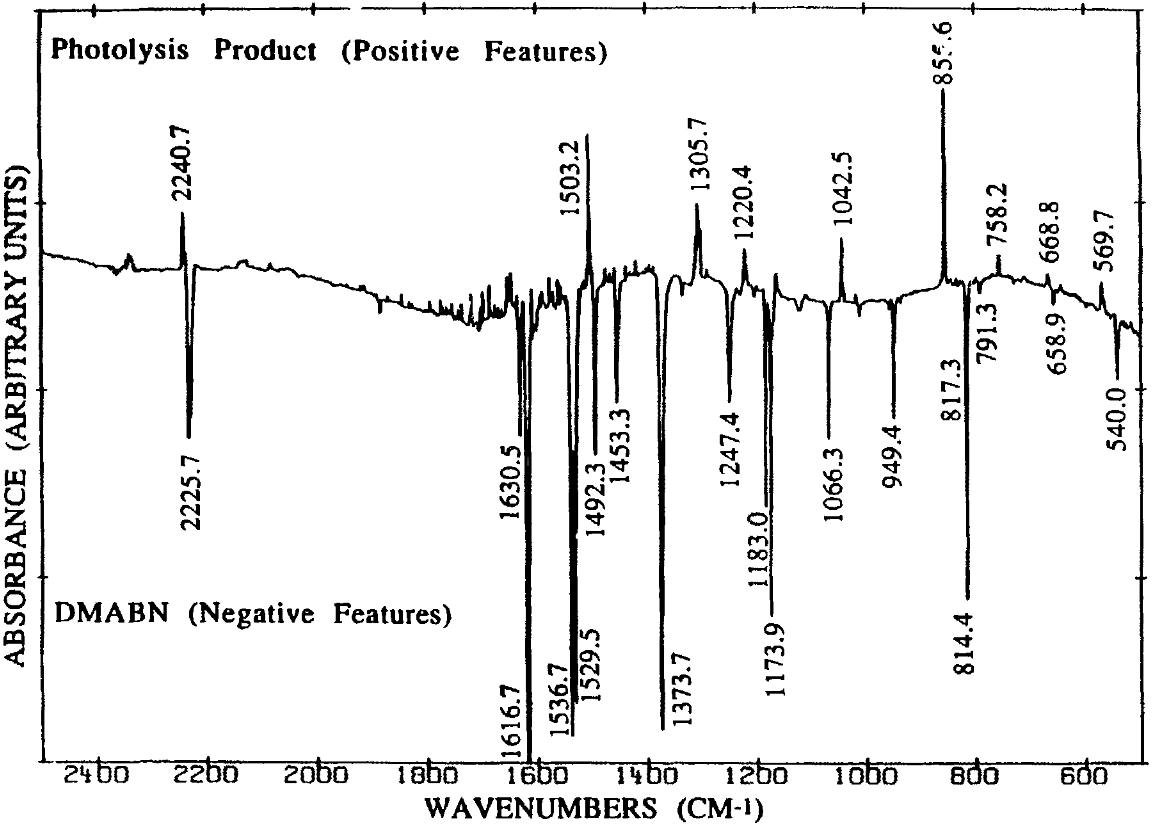
Photolysis Product (Positive Features)
DMABN (Negative Features)
ABSORBANCE (ARBITRARY UNITS)
WAVENUMBERS (CM-1)
2400
2200
2000
1800
1600
1400
1200
1000
800
600
2240.7
2225.7
1630.5
1616.7
1536.7
1529.5
1503.2
1492.3
1453.3
1373.7
1305.7
1247.4
1220.4
1183.0
1173.9
1066.3
1042.5
949.4
855.6
817.3
814.4
791.3
758.2
668.8
658.9
569.7
540.0

conformations are similar whereas S_1 and S_0 are not. This implies that T_1 and S_1 have displaced potential functions, a factor that may play a role in raising the value of k_{isc} in absence of heavy atom perturbation. If k_{isc} is initially high because of favorable Franck-Condon overlap, then any perturbation would be relatively smaller.

Siegel and Judeikis also compared glasses of naphthalene in 4:1 (by volume) ethanol:ethyl bromide to glasses of naphthalene in 4:1 ethanol:ethyl iodide. They found that while the ethyl bromide mixture increased k_p of naphthalene by a factor of five over that in pure ethanol, ethyl iodide increased k_p by a factor of 52. The results presented here are comparable, with xenon having 25 times the effect on k_p as krypton. The spin-orbit coupling factor ξ is expected to have a Z^4/n^3 dependence[59], where Z is the nuclear charge of the perturbing atom and n is its principle quantum number. Thus, bromine would be expected to have an effect similar to krypton, while the effect of iodine would be comparable to xenon's.

The rate constants calculated are consistent with the assumption that Φ_p in xenon is unity. The value for k_f in xenon is less than two percent of that calculated for k_{isc}, supporting the assumption that relaxation from S_1 is predominantly through T_1. The calculations show k_{isc} increasing by a factor of 3.3 in xenon and 1.8 in krypton, while k_{qp} in krypton increases by a factor of 2.3. The assumption that Φ_p in xenon is unity defines k_{qp} in xenon as zero, but if k_{qp} were to increase by approximately the same factor that k_{isc} does, as is the case in krypton, it would still have a value less than ten percent of that of k_p. This does not conflict greatly with the assumption that relaxation from T_1 in xenon is purely radiative.

The results presented here agree qualitatively but not quantitatively with those of Rettig et al.[60] who reported both k_f and quantum yields for DMABN in n-butyl chloride/2-methylbutane glass at 77K. These workers found a value of k_f five times larger than those found in argon and they report a total quantum yield of 1.00 compared to the values of 0.20 in Ar, 0.52 in Kr, and 1.0 in Xe. Furthermore, their ratio of Φ_p/Φ_f is 2.00, whereas larger ratios are found in the rare gas matrices, beginning at 4.8 in Ar (see Table XI). Their glass environment offers the spin-orbit coupling provided by chlorine atoms, so closest correspondence should be expected with the argon matrix results. Most surprising, then, is their reported unit quantum yield for radiation in the 77K glass. This seems contrary to the observation that the emission intensities increased with annealing as the matrix environment changed from amorphous (glassy) to crystalline. There is no ready explanation for this discrepancy. Even so, it can be concluded that if it is assumed that k_{qp} and k_{qf} are negligible, the qualitative result is retained, namely that the radiative rate constant k_p is more susceptible to the heavy atom effect than the nonradiative rate constant k_{isc}.

Mixed Matrices

The placement of a single external heavy atom in a fixed neighboring position of the chromophoric molecule can be compared to the substitution of a heavy atom on the molecule itself. A previous study[61] of halogenated anthracenes indicated that k_{qp} is highly dependent on the type and number of halogen substituents. The results given in Table XIII also show a strong dependence on both type and number: triplet lifetimes are shortened more by xenon than by krypton, and a single heavy atom neighbor has an effect intermediate between pure argon and pure heavy atom matrix.

The internal heavy atom effect is also site-specific[61], being greatest when substitution is at a site active in the chromophore. The relative coefficients of the unperturbed mixed matrix singlet lifetime can give an indication of the degree of site-specificity in the external heavy atom effect. For example, for a statistical 66:1 argon:xenon matrix, with 35 positions able to promote intersystem crossing, 59 percent of the DMABN molecules will have no heavy atom neighbors, and hence will decay with an unperturbed lifetime. On the other hand, if only fifteen positions around DMABN could promote intersystem crossing, 80 percent of the population would decay with the long lifetime. Thus, the long lifetime's coefficient of 0.51 is indicative of a lack of site-specificity within the first shell of neighboring positions. Coefficients for the triplet decays, which are weighted by the phosphorescence yield for the two populations, were too inconsistent to allow a similar calculation.

The singlet decay coefficients can be distorted by scattered excitation light, non-statistical mixtures, and/or a range of heavy-atom shortened lifetimes. Aside from these reservations, we are left with the conclusion that either the external heavy atom effect is not as site-specific as the internal heavy atom effect, or the fluorophore encompasses most of the molecule. The latter suggestion is supported by the high resolution spectra discussed in the next section.

Vibrational Analysis: Excited States of DMABN

The phosphorescence spectrum of DMABN (Figure 31, Table XIVc) shows a prominent set of vibronic transitions spaced 780-820 cm^{-1} apart. The wavelengths of these transitions are labelled in Figure 31 for emphasis. The less resolved phosphorescence excitation spectrum (Figure 30, Curve A and Table XIVa) contains two peaks at 290.4 and 284.2 nm, which are 2383 and 3135 cm^{-1} higher in energy than the 0-0 transition, respectively. These two peaks might be associated with the progression 1561, 2369 and 3194 cm^{-1}

which appears in the phosphorescence spectrum, presuming that the excited state vibrational frequencies differ little from those of the ground state. With an average spacing of 815 cm^{-1}, the phosphorescence progression may derive from the intense 814 cm^{-1} band which appears in the IR spectrum. Para-disubstituted benzenes have C-H out-of-plane deformations in this region.[62] For example, 4-bromochlorobenzene has an intense fundamental at 812 cm^{-1}, corresponding to the symmetric C-H deformation.[63] Gibson et al.[56] also observed this vibrational mode in the fluorescence excitation spectra of jet-cooled DMABN.

The fluorescence spectrum of Figure 30, Curve B (Table XIVb) also shows a set of peaks spaced about 800 cm^{-1} apart, but these transitions are not dominant as in the phosphorescence spectrum. Rather, the first large peak is 536 cm^{-1} away from the 0-0 transition, while the second is (831 + 527 = 1358) cm^{-1} away. The 535 cm^{-1} spacing can readily be associated with a 540 cm^{-1} vibration found in the IR spectrum of Figure 33. Aromatic nitriles have a strong band between 580 and 540 cm^{-1}, which is due to a combination of the out-of-plane aromatic ring-deformation and the in-plane nitrile deformation modes.[64] This mode, active in the fluorophore and involving most of the molecule, may account for the apparent lack of site-specificity in the external heavy atom effect on singlet decays.

The strong transition around 400 nm in the rare gas matrices, which is presumed to be the $S_0 \rightarrow T_1$ 0-0 transition, is indicative of favorable Franck-Condon overlap, i.e. similar geometry, between S_0 and T_1. The phosphorescence 0-0 transition is shifted to only 660 cm^{-1} lower in energy in acetonitrile matrix than in argon matrix. It can be inferred from this that the triplet state is also not particularly polar. On the other hand, the $S_0 \rightarrow S_1$ 0-0 transition is relatively weaker, and is shifted to 1200 cm^{-1} lower in energy in acetonitrile than in argon, indicating a higher degree of polarity and distortion in S_1 relative to S_0 and, hence, relative to T_1. The measured $S_0 \rightarrow S_1$ 0-0 energy (32,060 cm^{-1} in argon) compares favorably with the gas phase value[50,56] of about 32,265 cm^{-1}.

The experiments of Langan et al.[65] are relevant here. They also found for substituted carbenes that the $S_1 \rightarrow T_1$ energy gap decreased in polar solvents and that the change was accompanied by a decrease in k_{isc}. This raises the question of whether the higher dipole moment of DMABN's S_1 state could, through polarizability effects, account for the somewhat smaller $S_1 \rightarrow T_1$ splitting observed in xenon (6800 cm^{-1}) compared to argon (7010 cm^{-1}). If so, this change might be accompanied by a small decrease in k_{isc}, which would imply that the actual spin-orbit coupling effect is slightly larger than reported here.

In summary, the relative fluorescence and phosphorescence yields, and singlet and triplet lifetimes of DMABN isolated in argon, krypton, and xenon matrices have been measured. The quantum yields and lifetimes are consistent with a much greater increase in k_p than in either k_{qp} or k_{isc} in the presence of the external heavy atoms krypton or xenon. Lifetime measurements in mixed matrices of argon doped with krypton or xenon indicate that a single heavy atom neighbor significantly increases rates of spin-forbidden processes.

Charge Transfer State of DMABN

The "anomalous" fluorescence of polar, room-temperature solutions appears around 400-550 nanometers, depending on the solvent, and has an also solvent-dependent fluorescence lifetime of a few nanoseconds. No evidence of this fluorescence in the cryogenic rare gas, or even in the highly polar 12K acetonitrile, matrices is observed. The shape of the phosphorescence spectrum in acetonitrile, closely mimicked in the polar matrices of HBr and HCl, is apparently not indicative of a second fluorescent state or even two triplet states, but rather of inhomogeneous broadening. While the fluorescence spectrum loses all structure in the polar matrices, the phosphorescence spectrum has an intense leading peak approximately ten nanometers wide, followed by one broader peak centered at 338 nm in acetonitrile, 1600 cm^{-1} from the frequency at half height of the leading peak. As there is no indication of a fluorescent species in either of these two phosphorescence bands, and the observed triplet lifetime is the same in both these bands, the weak structure must be a vestige of that observed in the rare gas matrices, inhomogeneously broadened. Further evidence of inhomogeneous broadening is the non-zero excitation and emission intensities observable at wavelengths to the red and blue, respectively, of the S_1 0-0 wavelength (see Figure 32), greater than that expected from the 2 nm bandwidth of the monochromators.

The lack of observable emission from the charge transfer state in rigid, cryogenic matrices is in accordance with the observations of previous workers, who noted that the anomalous fluorescence present at room temperature is replaced by phosphorescence in 80K matrices of both PVA[51] and EPA[66].

It has been suggested that there is no intrinsic barrier to formation of the twisted intramolecular charge transfer state of DMABN, but rather that the viscosity, temperature, and polarity-dependent barrier derives from the barrier to rearrangement of the solvent which stabilizes the highly polar charge transfer state.[67] This could explain the lack of detectable "anomalous" fluorescence in the 12K acetonitrile matrices, even upon excitation at 284 nm, 12.4 kcal above the S_1 0-0 energy. The sizable shift in the S_1 0-0 energy in acetonitrile is an indication that the S_1 state is stabilized more than the ground state by this highly polar matrix. Furthermore, either the ground state and the S_1 state have very similar dipole orientations, or there is sufficient time during the nanosecond lifetime of the S_1 state for rearrangement of the solvent. A requirement for stabilization of the charge-transfer state is that solvent rearrangement be competitive with the lifetime of the vibrationally excited S_1 state, a more stringent requirement. Unless rearrangement proceeds at a rate that is several percent of the rate of vibrational deactivation, no change in the steady state emission spectrum would be observed upon excitation to the higher vibrational levels in the S_1 manifold.

On the other hand, if there is a stable ground state analogue to the charge transfer excited state, its formation would be detectable by ground state infrared spectroscopy even if the rate of the excited state solvent rearrangement is only a fraction of the rate of excited state vibrational deactivation, simply by employing long photolysis times. Although one possibility for the photoproduct (Figure 33) is the ortho-substituted rearrangement product, the fact that long term broad band irradiation bleaches out essentially all the initial DMABN suggests that the product has a very different absorption spectrum from the starting material. The charge transfer state, which is thought to involve twisting of the methyl groups from a position syn to the ring to a position anti to the ring, would be expected to have a very different electronic absorption spectrum, since rotation of the amino group means that the non-bonding electrons of the amino nitrogen are removed from conjugation with the ring. Thus, the possibility remains that the photolytic product is the ground state analogue of the excited state charge transfer conformer.

Heavy Atom Effects: OHBA, MS, and DMABN

One further note, by way of a comparison of the external heavy atom effect on the excited state lifetimes of DMABN, methyl salicylate, and o-hydroxybenzaldehyde, is in order here. The fluorescence lifetimes of DMABN and MS-C were similarly shortened in xenon matrix compared to those in argon matrix: DMABN by a factor of 3.2 and MS-C by a factor of 3.5. On the other hand, OHBA-C's fluorescence lifetime was, within the uncertainty of the measurements, unaffected by the heavy atom matrix. Although a lifetime was not obtained for MS-E's fluorescence, its intensity is severely diminished in xenon matrix compared to the non heavy atom matrix SF_6. Likewise, DMABN's fluorescence intensity was severely diminished in xenon matrix relative to that in argon. On the other hand, OHBA-F has no detectable fluorescence in either argon or xenon matrix. Finally, the vibrationally congested excitation and emission spectra of DMABN and MS-E support assignment of the S_1 states of these molecules as π,π^* with excitation delocalized throughout the π^* system, while OHBA-F's excitation and emission spectra are consistent with assignment of its S_1 state as n,π^*, with excitation centered on the carbonyl group. These lifetimes and state assignments are consistent with the notion that heavy atom matrices dramatically increase highly forbidden rates of intersystem crossing (e.g. from π,π^* states), but have little effect on rates which are already sizable in the absence of heavy atom perturbation (e.g. from n,π^* states). Taking this a step further, the dramatic effects on photochemical branching ratios observed for the photolysis of such compounds as the dichloroethylenes[5,7], for which reaction is thought to proceed from a π,π^* state, would not be expected in the instance of (for example) n,π^* S_1 carbonyl group excitation, with its intrinsically high rate of intersystem crossing.

CHAPTER VI. CONCLUSIONS

It has been shown in the previous chapters that there is much information to be gained about electronic excited states and photochemical reaction pathways (in particular about those of unimolecular, reversible photo-induced rearrangements in cryogenic matrices) from a combination of steady-state and time-resolved spectroscopic techniques. However, results from the more novel technique of determining the energies of excited state barriers by measuring the wavelength dependence of reaction quantum yields are both scarce and tenuous. Since the original goal of this research was to measure excited state barriers by this technique, it is appropriate to examine why such results were not easily forthcoming and which types of systems might yield more definitive results in the future, and to anticipate any sources of ambiguity in interpretation of a positive result.

Not all photochromic systems are expected to have the double well excited state potentials proposed for OHBA and MS. Discussed in this chapter are two alternatives shapes, a single well potential and a triple well potential, both of which can arise from symmetry-imposed interaction of two or more zero-order singlet states. While no wavelength dependence of a quantum yield would be detected for a single well potential, the possibility of a triple well potential must be considered in the interpretation of a detected wavelength dependence. Another point of discussion is the fact that higher electronic states (for example, higher energy triplet states) can provide efficient reaction channels, and therefore larger quantum yields at higher excitation energies, which have nothing to do with reaction over the S_1 barrier.

Even when there is a single barrier on the S_1 surface and no other energetically accessible excited state reaction surfaces, the reaction quantum yield may or may not be sensitive to the barrier, since the rate of reaction over the barrier must be significant relative to the rates of other deactivation (including alternate reaction!) processes. The rates of excited state deactivation processes are discussed, with particular regard to the choice of a molecular system likely to have rate constants appropriate for measuring an excited state barrier. Following these more theoretical considerations is a discussion of practical, experimental aspects, and suggestions of molecular systems for future experiments.

Potential Energy Surfaces

Ground state barriers to reaction have been determined from the wavelength dependence of infrared-induced reaction quantum yields.[1] The major difference between these experiments and the analogous excited state experiments is the plurality of states accessible upon excitation into the S_1 manifold. The interpretation of the results from the study of the wavelength dependence of the reaction quantum yield for the photolysis of OHBA-C illustrates the ensuing complications admirably. Excitation into the minimum of the S_1 state provides access to an efficient ground and/or triplet state reaction route, and any increase in the reaction quantum yield upon excitation to an energy above the S_1 barrier must be measured as an addition to the already large quantum yield for reaction below the S_1 barrier. In the case of OHBA-C, the apparent increase in the quantum yield with the higher photolysis energies is less than the magnitude of the scattering correction used in calculating the relative quantum yields.

A second complication, also a result of the several electronic states accessible upon excitation to S_1, can arise in the interpretation of a reaction quantum yield wavelength dependence. An increase in the reaction quantum yield with higher photolysis energies does not necessarily indicate a reaction along the S_1 surface, but rather may indicate the existence of an efficient channel to a different reaction surface. Methyl salicylate provides an example here. As discussed in Chapter IV, there is a route to non-radiative decay 1300 cm^{-1} above MS-C's S_1 minimum, indicated by the rapid fall-off in fluorescence lifetimes with excitation above this energy in jet-cooled samples[43]. While it is unknown at this point whether this non-radiative decay route is one of reaction, it could well be. It would however be entirely false to interpret this 1300 cm^{-1} energy as the height of the S_1 barrier, as MS-E's S_1 minimum lies 1500 cm^{-1} higher still in energy.

At this juncture a discussion of symmetry is in order, as it, along with bond energies, plays a role in determining the shape of electronic surfaces and barriers on those surfaces. When zero-order electronic states of the same symmetry and spin cross in energy-geometry space, an "avoided crossing" results. Three examples of the effect of mixing on the shape of the singlet surfaces are sketched in Figures 34A, B, and C. The first, Figure 34A, is that proposed for the reaction coordinate of OHBA-C and OHBA-F. The result of the zero-order (dashed lines) ground, S_1, and S_2 states of OHBA-C mixing with the ground, S_1, and S_2 states of OHBA-F, respectively, produce the stack of double-well potentials in the first order approximation (solid lines).

Figure 34B is a sketch of the singlet surfaces proposed[68] for the 9,9' methylene linked dianthracene moiety, and its 9,9';10,10' doubly-linked photoproduct. The symmetry-mandated correlation of the reactant ground state with the product excited state and visa-versa results in a single well potential in the excited state. Evidence for the single minimum comes from measurement of the reaction quantum yields for the forward and reverse reactions, the sum of which roughly equals unity, as well as from detection

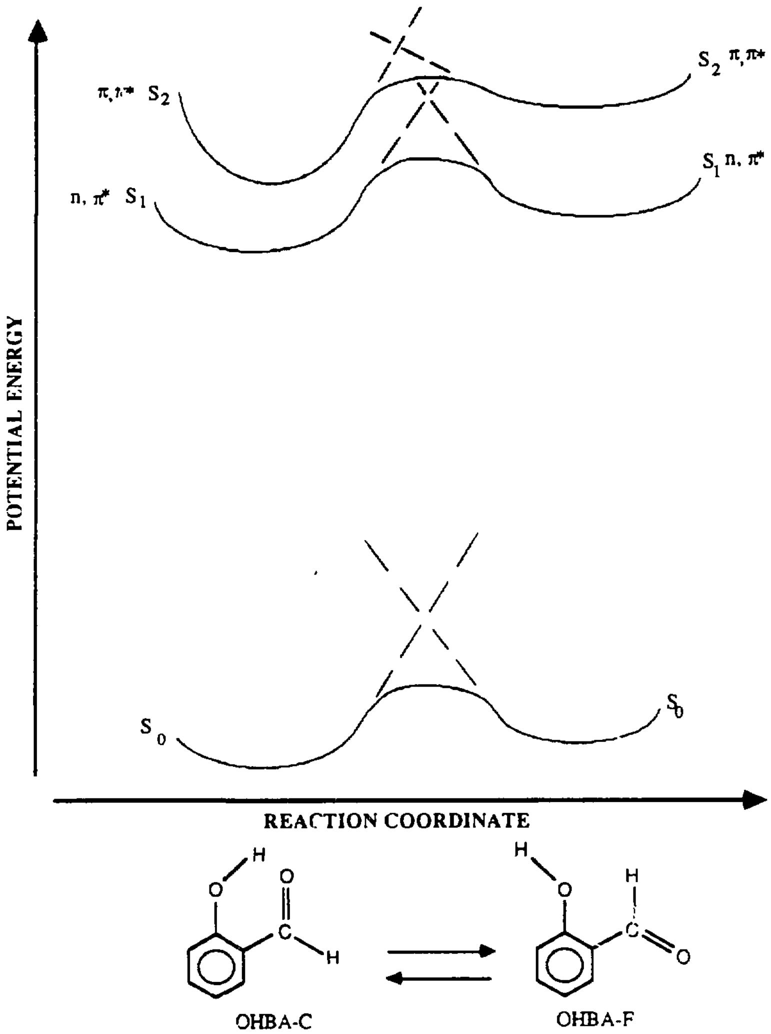

Figure 34A. Sketch of the zero-order (dashed lines) and first-order (solid lines) approximations to the singlet potentials proposed for the reaction coordinate of OHBA-C → OHBA-F.

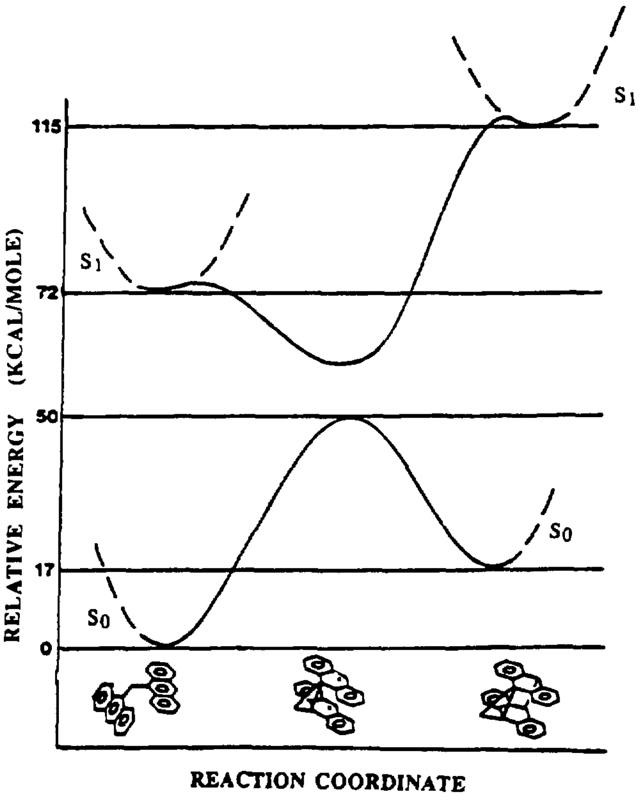

Figure 34B. Sketch of the zero-order (dashed lines) and first-order (solid lines) approximations to the singlet potentials proposed for the reaction coordinate of the 9,9' methylene-linked dianthracene → the 9,9';10,10' doubly linked photoproduct, from Bergmark et al.[68].

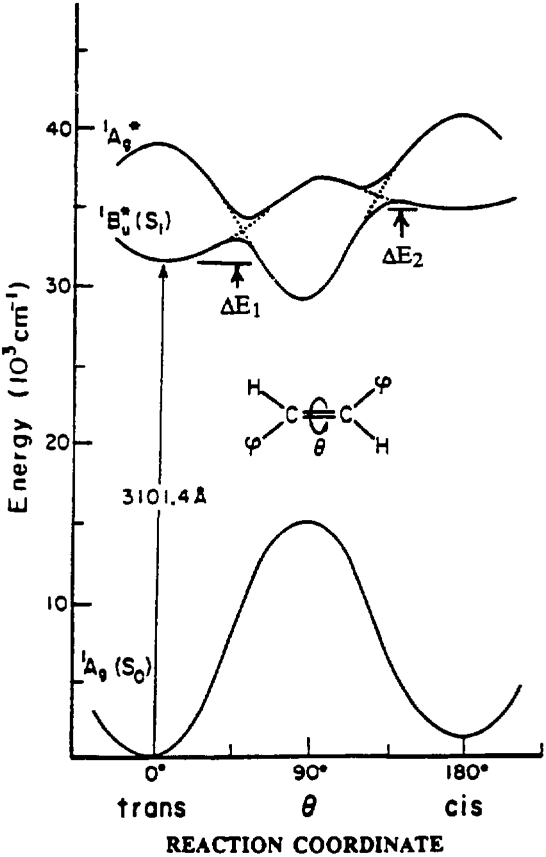

Figure 34C. Sketch of the zero-order (dashed lines) and first-order (solid lines) approximations to the singlet potentials proposed for cis and trans stilbene as a function of ethylene torsional coordinate, from Syage et al.[69]

of a common intermediate upon photolysis in either direction.

It has been hypothesized that all pericyclic, Woodward-Hoffman allowed photochemical processes have a single well S_1 potential[70], with the minimum corresponding to a diradical species. There is however, in the case of the methylene-linked dianthracene of Figure 34B, some retention of the zero-order S_1 excited state, in that a small amount of fluorescence is detectable from the mono-linked anthracene.

A third type of singlet surface, shown in Figure 34C, is proposed for, amongst other substituted ethylene species, cis- and trans-stilbene.[69] From a study of the excitation energy dependence of fluorescence lifetimes in supersonic jets, Syage et al. propose the three-well S_1 potential surface, which is a result of mixing of the zero-order S_1 and S_2 states.

The single well potential (Figure 34B) is distinguishable from a double well potential (Figure 34A) by detection of a common intermediate which decays to ground state species with a branching ratio independent of the side of the potential well from which it originated. Furthermore, the pure S_1 single well potential is a repulsive potential for both the reactant and product, with the result that excitation and absorption spectra have weak 0-0 absorptions and lack vibrational structure. A pure single well potential will also have a reaction quantum yield which is wavelength independent.

Like the double well potential proposed for OHBA and MS, the triple well potential of Figure 34C can exhibit a wavelength dependence of the reaction quantum yields corresponding to detection of the barriers to formation of the middle S_1 well. Both the reactant and the product can exhibit fluorescence with strong 0-0 transitions. Confirmation of the double-well excited state might then rely on measurement of the barrier in both directions, although this requires accurate data on ΔH for the system.

Even then, there could be accidental coincidence of the barriers on the S_1 surface (marked ΔE_1 and ΔE_2 in Figure 34C). The triple well S_1 does however imply a repulsive S_2 potential in zero order. The vibrational structure in OHBA-F's S_2 absorption system, along with the strong 0-0 transition precludes the three well potential as a possibility for the S_1 surface of OHBA.

Thus, although electronic excitation may often be into a state which can be characterized reasonably accurately by the zero-order potential of the chromophore, a description of any reaction coordinate must include more than one zero order potential. These zero order potentials are correlated to form the S_1 reaction surface, whose shape is determined not only by the energies and nuclear geometries of the zero order potentials, but also their symmetries. In some instances, such as those depicted in Figures 34B and C, the resulting S_1 surface may bear little resemblance to the double well potential of the ground state.

Deactivation Within the S_1 Manifold

Under liquid phase conditions, where good coupling of thermal energy to and from the solvent exists, excitation above the S_1 0-0 energy produces a population in S_1 whose vibrational energy is characterized not by the photolysis energy but rather by the Boltzmann distribution mandated by the temperature of the bulk sample. Existence of a wavelength dependence of the reaction quantum yield upon excitation into the S_1 manifold implies that reaction takes place from vibrational states which are not in thermal equilibrium with the bulk sample. In this instance, the initially excited superposition of states, with the nuclear geometry which resembles the ground state of the reactant, evolves into a superposition of states with a nuclear geometry resembling that of the ground state of the product before thermal cooling takes place to the point that the excited state wavefunction has no probability density corresponding to the nuclear geometry of the product. In other words, a wavelength dependence of the quantum yield implies that reaction takes place before the vibrational energy imparted upon excitation to the S_1 state has been thermalized Another way to describe this phenomenon, which is particularly appropriate to the double well description of the S_1 surface proposed for OHBA, has been suggested by H. Frei[71] and is discussed below.

Returning to the zero order description of the S_1 states (Figure 35), a rate of radiationless crossing to the product S_1 state (k_{react}) can be defined. A requirement for photochemistry on an S_1 surface with a barrier is that $1/k_{react}$ at any particular excess energy be comparable to the lifetimes of the vibrationally excited states. The lifetime of the vibrationally hot states is determined by three factors: the temperature of the solvent, the lifetime of the singlet state as a whole (determined by the rates of fluorescence, intersystem crossing, reaction on surfaces other than S_1, and internal conversion to S_0), k_{react}, and the rate of vibrational deactivation (k_{deact}). The first three factors are most important in the high temperature region, where the population in the upper vibrational states of the singlet manifold is controlled by the Boltzmann distribution and the S_1 lifetime. In the low temperature region, applicable to these studies in cryogenic matrices, the lifetime of the vibrationally excited states is governed by k_{deact} and k_{react}, since thermal population of the vibrationally excited states is negligible.

k_{react} will only be non-zero at energies and geometries where there is overlap of the wavefunctions for the two S_1 states, which is tantamount to stating that there is a barrier to reaction roughly defined by the crossing point of the zero-order potential wells. Thus, observation of reaction in the

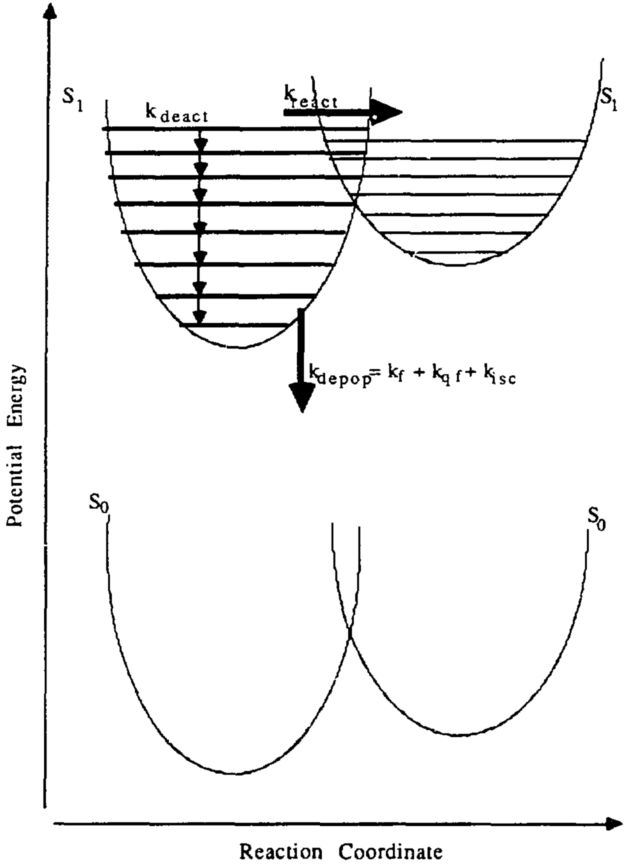

Figure 35. *Sketch showing the rate constants applicable to reaction in the* S_1 states in the zero-order approximation.

S_1 states in cryogenic matrices requires that excitation be to an energy above this barrier, and that crossover to the product S_1 state be effected before cooling to an energy below the barrier is effected. As there is finite wavefunction probability outside the potential wells, the barrier is defined by a smooth surface rather than a cusp, thereby retrieving the first order approximation of Figure 34A.

With the zero-order picture in mind, one can separate the factors that govern the magnitude of k_{deact} and k_{react}. k_{react} is firstly determined by the rate of intramolecular vibrational redistribution (IVR), since initial excitation seldom places all the vibrational energy in the vibrational mode corresponding to the reaction coordinate. k_{IVR} is in turn dependent on the density of states; a function of the total excess energy, the energy of the vibrational modes, and the number of vibrational modes. Also, previous work has shown that IVR can be non-statistical[72], so k_{react} can also depend on whether or not the reaction coordinate is amongst the coordinates which receive the vibrational energy. Secondly, k_{react} is determined by the degree of overlap between the wavefunctions of the two potential wells. Thus, it will be greatest well above the barrier and negligible below the barrier, except in the instance of proton transfer reactions, for which tunneling is thought to be an important mechanism[73]. Thirdly, the number of vibrational modes in the molecule, which is dependent on the size of the molecule, plays a role as the region of overlap in the reaction coordinate may, for a large molecule, be a tiny portion of the total wavefunction of the reactant's S_1 state.

k_{react} is thus difficult to predict. However, a reasonable estimation of the upper limit on k_{react} might be obtained as the rate of vibration in the reaction coordinate. For an excited state vibrational frequency of 1000 cm^{-1}, corresponding to a modest barrier, an upper limit on k_{react} would be on the order of 10^{13} sec^{-1}. This is comparable to the 10^{12} sec^{-1} rate proposed for IVR in the gas phase[72], as determined by line widths of vibrational absorptions, and which is thought to be higher in condensed phase.

As discussed in the review article by Bondybey[72], estimates of k_{deact} can be obtained from fluorescence lifetimes of vibrationally unrelaxed states. Unrelaxed emission has been observed for a number of molecules in cryogenic rare gas matrices from vibrational states with excess energy as high and higher than 2000 cm^{-1}, with lifetimes between 1 and 300 picoseconds, placing k_{deact} in the range of 10^9 to 10^{12} sec^{-1} under these "favorable" conditions.

It has been proposed that k_{deact} is generally lower in rare gas matrices because of the poor coupling between the rare gas matrix and the vibrational modes of the excited molecule. This can largely be attributed to the generally large difference between the vibrational frequencies of the guest molecule (usually 400 - 4000 cm^{-1}) and the vibrational (phonon) modes of the host lattice, which are in the neighborhood of only 50 cm^{-1}. This reasoning breaks down however when the guest molecule has low frequency vibrational modes. Hydrogen-bond stretch frequencies are in the range of 250-50 cm^{-1}, while the bending frequency is usually less than 50 cm^{-1}.[74] Non- or barely hindered internal rotations also have frequencies in this range.

Thus, in this zero-order description of photochemistry on the S_1 surface, it appears that reaction can indeed compete with deactivation, such that excitation with light of an energy higher than that of an excited state barrier can result in reaction above that barrier. Whether this high energy reaction route results in a detectable increase in the quantum yield over that measured with excitation below the barrier depends on the magnitude of the low energy quantum yield, the rate of deactivation, and the rate of reaction. Finally, when a wavelength dependence of a reaction quantum yield is detected, care must be taken in the interpretation, since at least two other electronic states (T_1 and S_0) are energetically accessible upon excitation into S_1.

Experimental Considerations

Measurement of an increase of a few percent of the quantum yield, rather than the orders of magnitude increases observed with the analogous IR photochemistry, requires that each measurement which goes into the quantum yield; the absorption at the wavelength of photolysis, the amount of reactant and product present, and the number of photons impinging on the sample, each have a very low level of uncertainty. The greatest sources of uncertainty in the measurement of the wavelength dependence of the quantum yield for the photolysis of OHBA-C were the small extinction coefficients at the short wavelengths where the reaction quantum yield would be expected to increase, the extent to which light is scattered at these wavelengths, and the actual absorption at the wavelength of photolysis. Little can be done about the first two concerns other than to limit oneself to studies of molecular systems for which the barrier to reaction is much smaller than the bandwidth of the electronic absorption.

With knowledge of the actual absorption one can avoid the optical thinness approximation that the number of photons absorbed is proportional to the extinction coefficient at the wavelength of photolysis. While this is a seemingly good approximation, even the relatively low absorbance of 0.1 results in a 9% underestimation of the quantum yield relative to that observed for a sample with an absorbance of .01, an intolerably large error when one is looking for modest increases in a large quantum yield. The solution to this dilemma is clearly to monitor the extent of photolysis in the UV, such that the actual percentage of incident photons absorbed is known.

It is however highly desirable to monitor the extent of reaction by IR spectroscopy, so that absorption bands of the reactant and product are resolved and the probe source cannot induce reaction. Thus, one solution is to simultaneously monitor the reaction by IR and UV absorption spectroscopies; either by temporarily routing the UV sample beam through the matrix with mirrors so that it is collinear with the IR spectrometer's beam, or by directing the IR beam through the matrix at the UV spectrometer, or even by moving the cryostat between the two spectrometers. Of the three possibilities, the last is probably effected most easily. While the source of the Shimadzu UV2100 spectrometer used in this study is nominally focussed at the center of its sample compartment, the discrepancy in the focussing of the planes of light would be problematic over the ~70 cm required to get the UV sample beam to the IR97 sample beam. On the other hand, once a rare gas matrix is deposited there is no need to have the cryostat connected to a vacuum line, leaving it quite mobile with the addition of good shut-off valves.

An alternative approach is to maintain optically thick matrices. With absorbances at 2.0 at all photolysis wavelengths, there is less than a 1% error in the assumption that all the photolysis light is absorbed. However, optical densities of 2.0 are difficult to maintain for matrix isolated samples with low extinction coefficients. Thus, one might be limited with this approximation to molecules with a π,π^* transition with a reasonably strong 0-0 absorption intensity.

An alternative to simultaneous detection by IR and UV/Vis absorption spectroscopies is to monitor the extent of photolysis by emission spectroscopy. Data analysis is simple provided that either the absorption or the excitation bands of the reactant and product are separated at some wavelength, such that one can monitor either the appearance of the product absorption or emission alone, or the disappearance of the reactant alone. Otherwise, one must resort to separating the contributions of the absorption coefficients, emission quantum yields, and amount of material of the two forms to the observed intensity. This is not however a very demanding limitation, as there is seldom complete overlap of both excitation bands and emission bands for any reactant and product for which there has been a significant change in bonding. A more serious limit is that the reaction quantum yield must be low enough that negligible amounts of photolysis occur while the matrix is being monitored for the extent of reaction. Thus, the photolysis of OHBA-C to OHBA-F is not a suitable candidate for such a study, in that it is not even possible to collect an excitation or emission spectrum of this molecule without detecting phosphorescence from the highly emissive product.

One assumption with this technique is that the emission quantum yield is independent of excitation wavelength. While this may seem like a limitation, the result of any deviation is to magnify any apparent change in reaction quantum yield with wavelength, since reaction will be at the expense of reactant emission.

Another source of uncertainty in the measurements of the wavelength dependence of the reaction quantum yields comes from the photolysis source. While lasers have the distinct advantage of providing a high-flux monochromatic source, great care has to be taken to ensure that the laser photolysis beam is reproducible, not only in shape, size, and placement relative to the IR monitoring area, but also in the distribution of intensity within the beam. This is a serious consideration when working with with the frequency doubled output of an amplified dye laser pumped by a frequency doubled infrared laser source, in that each doubling process is non-linear, depending on the square of the intensity. Thus, any irregularities in beam shape are magnified several times. This is a problem not encountered when measuring reaction quantum yields in solution phase, where one can ensure uniform photolysis simply by stirring.

A way around the problem of spatial irregularities in the photolysis beam shape is to revert to the old-fashioned approach of a broad beam source and a monochromator, although there are disadvantages with this approach too. For one thing there is a drastic decrease in photolysis power with increases in frequency resolution, limiting one to reactions with higher quantum yields. Furthermore, the energy of the excited state barrier cannot be determined with a precision greater than the bandwidth of the photolysis source.

In the instance that a photolysis quantum yield is neither particularly high nor particularly low (and the reactant emits!), the steady-state fluorimeter comes to mind again as a useful instrument for measuring excited state barriers. Light from the fluorimeter source, by way of the excitation monochromator, is very uniform and has a controllable, albeit lower, bandwidth. In the case of a molecule such as OHBA-F, this could turn out to be somewhat of an advantage, since much of the difficulty in measuring the wavelength dependence of the quantum yield for photolysis of OHBA-F to OHBA-C is that the photolysis of one site relative to the other is highly dependent on the photolysis wavelength, and yet the two sites were not fully resolved either in the UV or in the IR. Selection of a bandpass wider than the splitting of the two sites would then result in photolysis of the two sites in a constant mixture, irrespective of the wavelength of photolysis (provided that the reaction quantum yield is the same for the two sites for any given excess energy).

In summary, determination of excited state barriers to reaction by the measurement of quantum yields to reaction in cryogenic matrices is an entirely feasible experiment, although not for all systems. For example, those reactions that proceed with a quantum yield approaching unity upon excitation at the S_1 0-0 energy cannot possibly show an increase in the quantum yield with excitation to higher vibrational levels. Those reactions that have a single well reaction pathway, and hence no excited state barriers to measure, will also not yield any results from such a study.

Of those reactions that do have a reasonably low quantum yield upon excitation to the S_1 0-0 energy, and have a barrier to reaction in the S_1 state, some will produce results more easily, and less ambiguously, than others. Flexibility, both in the photolysis source and in the method of detection, can enhance the likelihood of a successful experiment. The following is a summary of the attributes that might be considered in deciding whether a particular reaction is likely to be a fruitful subject for this experiment, along with suggestions of appropriate molecular systems for study.

Reactions

The first, and most fundamental, requirement for measuring an excited state barrier is that the barrier exist. One sign of a barrier to reaction is of course a temperature dependence of the reaction quantum yield. Two spectroscopic signs are the presence of vibrational structure in the excitation and/or absorption spectra, and fluorescence. It is desirable that the reactant be fluorescent anyway, since it is only from the overlap of excitation and emission spectra that one can, without resorting to isotopic substitution, absolutely determine 0-0 energies. Without the 0-0 energy, the energy of the barrier to reaction is uninteresting: without it, the depth of the excited state well is not known.

The next most crucial point is that the quantum yield for reaction upon excitation to the S_1 minimum be reasonably low, so that a mild increase in the reaction quantum yield is detectable. This is an unfortunate point, since this excludes from this type of study some of the most interesting, high yield photochemistry.

Thirdly, unimolecular, photo-reversible reactions provide an opportunity to check the assignment of a barrier by determining it for both the forward and reverse reactions,' which also helps to resolve the previously discussed ambiguities associated with higher energy reaction pathways besides S_1. Confirmation does however rely on accurate knowledge of the ground state energy difference for the two forms.

Fourthly, the (at least relative) extinction coefficient must be accurately determinable. For this, molecules that do not have n,π* transitions are often simpler to work with, in that n,π* transitions have such low extinction coefficients, sometimes with low absorbance long wavelength tails. Also, n,π* transitions can be hidden under π,π* transitions, providing a source of ambiguity in interpretation of a detected wavelength dependence of the quantum yield. Another advantage of avoiding molecules with an n,π* transition is that n,π* excited states tend to couple strongly to triplet states, which can provide a low energy pathway to reaction.

Finally, rigid molecules devoid of groups that provide a source of low frequency internal rotation or torsional modes are thought to couple most poorly to the rare gas lattice, thus allowing for the most favorable competition between k_{react} and k_{deact}.

Polycylcic Cyclobutene The previously discussed cycloreversion of the polycyclic cylcobutene pictured below has been shown to exhibit a wavelength dependent quantum yield to reaction in a rigid 77K hydrocarbon glass[75].

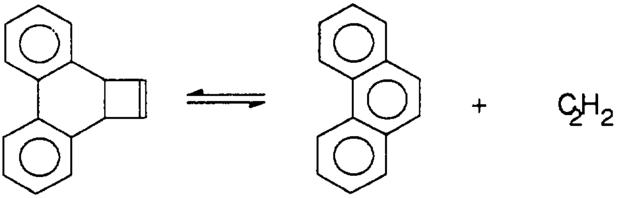

It should undoubtedly exhibit a wavelength dependence in a cryogenic rare gas matrix where coupling to the solvent is further reduced. It has the advantages of having no groups that produce low frequency torsional modes, structured fluorescence with a strong 0-0 transition, weak phosphorescence (perhaps indicating poor coupling of S_1 with triplet states), and a negligible quantum yield at the longer photolysis wavelengths. Non-trivial disadvantages are: it's a fairly large molecule to deposit into a matrix from its vapor pressure (although molecules as large as 3-hydroxyflavone have been successfully deposited[76]), and it does not undergo unimolecular rearrangement, such that it could prove difficult if not impossible to verify a barrier assignment by a reverse photolysis.

OHBA-F The photolysis of OHBA-C to OHBA-F is too fast to follow in the fluorimeter. The reverse reaction, with its five-fold lower quantum yield, is a good candidate however, particularly since OHBA-F has a significantly higher emission quantum yield. Thus, the disappearance of the 405 nm emission feature with excitation at 314 nm could be followed as a function of photolysis wavelength, with little interference from OHBA-C's emission. Again, the photolysis wavelengths would be essentially limited to those of its S_2 absorption system (314-280 nm), since the steady state population of OHBA-F with photolysis in its n,π* S_1 region is miniscule. As mentioned previously, the reduced and identical resolution of the photolysis and detection source could actually prove an advantage with this molecule.

o-Hydroxyacetophenone. Like OHBA, o-hydroxyacetophenone, pictured below, exists in its hydrogen-bonded conformer at room temperature, and photolyzes to a matrix-trappable non-hydrogen-bonded conformer.[14]

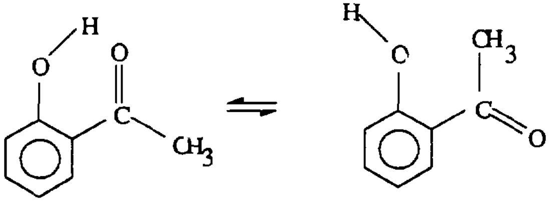

However, the photoreaction proceeds at a rate intermediate between that for OHBA-C and MS-C, making it an excellent candidate for such a study using the fluorimeter.

Acrolein Acrolein exists in both s-cis and s-trans forms, as pictured below.

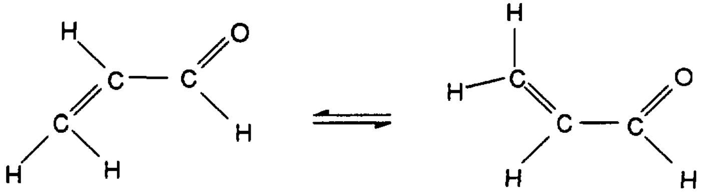

s-trans s-cis

It is predicted to have a double well excited state[77], and in fact fluoresces, although with a very low quantum yield (~.007 in 77K glasses). The ground state enthalpy difference is fairly well characterized[78] at 700 ± 40 cm^{-1}, with an excited state enthalpy difference of -522 ± 40 cm^{-1}, based on the ground state difference and the 0-0 transition energies. Unfortunately, the low quantum yield for fluorescence has meant that attempts to measure it, and thereby the 0-0 transition energies in a rare gas matrix, have been unsuccessful. Otherwise, this looks like a very promising avenue for research.

REFERENCES

(1) Frei, H.; Pimentel, G. C. *Ann. Rev. Phys. Chem.* **1985**, *36*, 491-524.

(2) Michl, J.; Castellan, A.; Souto, M. A.; Kolc, J. in *Excited States in Organic Chemistry and Biochemistry;* Pullman, B., Goldblum, N., Eds.; D. Reidel Publishing Co.: Dordrecht, Holland, 1977.

(3) Rentzepis, P. M.; Bondybey, V. E. *J. Chem. Phys.* **1984**, *80(10)*, 4727-4737.

(4) Collins, S. T.; Pimentel; G. C. *J. Phys. Chem.* **1984**, *88*, 4258.

(5) Cartland, H. E.; Pimentel, G. C. *J. Phys. Chem.* **1986**, *90*, 1822.

(6) Singmaster, K. A.; Pimentel, G. C. *J. Mol. Struct.* **1989**, *194*, 215-238.

(7) Laursen, S. L.; Pimentel, G. C. *J. Phys. Chem.* **1989**, *93*, 2328.

(8) Lippert, E. *Ber. Bunsenges. Phys. Chem.* **1988**, *92*, 1417.

(9) Morgan, M. A.; Pimentel, G. C. *J. Phys. Chem.* **1989**, *93*, 3056; and references therein.

(10) Morgan, M. A.; Orton, E.; Pimentel, G. C. *to be submitted to J. Phys. Chem.*

(11) Pederson, T.; Larsen, N. W.; Nygaard, L. *J. Mol. Struct.* **1969**, *4*, 59.

(12) Anet, F. A. L.; Ahmad, M. *J. Am. Chem. Soc.* **1964**, *86*, 119.

(13) Haque, M. K.; Thakur, S. N. *Chem. Phys. Lett.* **1979**, *66:3*, 561-564.

(14) Orton, E.; Morgan, M. A.; Pimentel, G. C. *to be submitted to J. Phys. Chem.*

(15) Turro, N. J. *Modern Molecular Photochemistry;* Benjamin/Cummings Publishing Co.: Menlo Park, CA, 1978; Chapter 5.

(16) Nishiya, T.; Yamauchi, S.; Hirota, N.; Baba, M.; Hanazaki, I. *J. Phys. Chem.* **1986**, *90*, 5730-5735.

(17) Nagaoka, S.; Nagashima, U.; Ohta, N.; Fujita, M.; Takemura, T. *J. Phys. Chem.* **1988**, *92*, 166-171.

(18) Toribio, F.; Catalan, J. Amat, F.; Acuna, A. U. *J. Phys. Chem.* **1983**, *87*, 817-832.

(19) Goodman, J.; Brus, L. E.; *J. Am. Chem. Soc.* **1978**, *100:24*, 7472-7474.

(20) Smith, K. K.; Kaufmann, K. J. *J. Phys. Chem.* **1981**, *85*, 2895-2897.

(21) Felder, P.; Gunthard, Hs. H. *J. Mol. Struct.* **1980**, *60*, 297-300.

(22) Rajogopal, E.; Sivakumar, K. V.; Subrahmanyam, S. V. *J. Chem. Soc., Faraday Trans. 1*, **1981**, *77*, 2149.

(23) Schaefer, T. *J. Phys. Chem.* **1975,** *79:17,* 1888-1890.

(24) Schaefer, T.; Sebastian, R.; Laatikainen, R; Salman, S. *Can. J. Chem.* **1984,** *62,* 326-331.

(25) Tabei, M.; Tezuka, T.; Hirota, M. *Tetrahedron,* **1971,** *27,* 301-306.

(26) Hirota, M.; Suzuki, T.; Abe, K. *Bull. Chem. Soc. Jap.* **1977,** *50:5,* 1129-1132.

(27) Smith, K. K.; Kaufmann, K. J. *J. Phys. Chem.* **1978,** *82:21,* 2286.

(28) Turro, N. J. *Modern Molecular Photochemistry;* Benjamin/Cummings Publishing Co.: Menlo Park, CA, 1978; Chapter 7.

(29) Bellamy, L. J. *Advances in Infrared Group Frequencies;* Methuen and Co. Ltd.: London, 1968; Chapter 8.

(30) Kuper, J. W.; Perry, D. S. *J. Chem. Phys.* **1984,** *80:10,* 4640-4645.

(31) Moore, J. W.; Pearson, R. G. *Kinetics and Mechanism,* 3rd ed.; John Wiley and Sons: New York, 1981; Chapter 4.

(32) Avouris, P.; Gelbart, W. M.; El-Sayed, M. A. *Chem. Rev.* **1977,** *77:6,* 793-833.

(33) Jacobson, B. A.; Guest, J. A.; Novak, f. A.; Rice, S. A. *J. Chem. Phys.* **1987,** *87:1,* 269-283.

(34) Nagaoka, S.; Hirota, N.; Sumitani, M.; Yoshihara, K. *J. Am. Chem. Soc.* **1983,** *105:13,* 4221.

(35) Levine, I. N. *Quantum Chemistry,* 2nd ed.; Allyn and Bacon, Inc.: Boston, 1974, p. 57.

(36) Duben, A. J.; Goodman, L.; Koyanagi, M. in *Excited States, Vol 1* Lim, E. C., Ed.; Academic Press: New York, 1974.

(37) Pimentel, G. C.; Spratley, R. D. *Understanding Chemistry*; Holden-Day: San Francisco, 1971; Appendix g.

(38) Orton, E.; personal communication.

(39) Carlson, G. L.; Fateley, W. G. *J. Phys. Chem.* **1973,** *77:9* 1157-1163.

(40) Seliskar, C.; Khalil, O.; McGlynn, S. in *Excited States, Vol. 1* Lim, E. C., Ed.; Academic Press: New York, 1974.

(41) Helmbrook, L.; Kenny, J. E.; Kohler, B. E.; Scott, G. W. *J. Phys. Chem.* **1983,** *87,* 280-289.

(42) Acuna, A.; Catalan, J.; Toribio, F.; *J. Phys. Chem.* **1981,** *85,* 241.

(43) Felker, P. M.; Lambert, W. R.; Zewail, A. H. *J. Chem. Phys.* **1982,** *77:3,* 1603-1605.

(44) *Tables of Interatomic Distances and Configuration in Molecules and Ions, Special Publication No. 11*, compiled by Bowen, H. J. M. et al.; The Chemical Society: London, 1958.

(45) Pimentel, G. C.; Spratley, R. D. *Understanding Chemistry*; Holden-Day: San Francisco, 1971; Chapter 18.

(46) McGlynn, S. P.; Azumi, T.; Kinoshita, M. *Molecular Spectroscopy of the Triplet State*; Prentice-Hall: Englewood Cliffs, NJ, 1969; Chapter 2.

(47) McGlynn, S. P.; Reynolds, M.J.; Daigre, G. W.; Christodoyleas, N. D. *J. Phys. Chem.* **1962,** *66*, 2499.

(48) Lippert, F.; Boos, H. *Proc. of the 4th Intern. Meeting Molecular Spectroscopy, Bologna, Italy 1959;* Macmillan: New York, 1962. p. 443.

(49) Rettig, W. *Angew. Chem. Int. Ed. Engl.* **1986,** *25*, 971.

(50) Peng, L. W.; Dantus, M.; Zewail, A. H.; Kemnitz, K.; Hicks, J. M.; Eisenthal, K. B. *J. Phys. Chem.* **1987,** *91*, 6162.

(51) Cazeau-Dubroca, C.; Peirigua, A.; Ait Lyazidi, S.; Nouchi, G.; Cazeau, Ph.; Lapouyade, R. *Chem. Phys. Letters* **1986,** *124*, 110.

(52) Lampert, R. A.; Meech, S. R.; Metcalfe, J.; Phillips, D.; Schaap, A. P. *Chem. Phys. Letters* **1983,** *94*, 137.

(53) Wiedeman, L.; Fajardo, M. E.; Apkarian, V. A. *J. Phys. Chem.* **1988,** *92*, 342.

(54) Fajard, M. E.; Apkarian, V. A. *J. Chem. Phys.* **1986,** *85*, 5660.

(55) The number of nearest neighbor positions was estimated using bond lengths of (Grabowski, Z. R.; Rotkiewicz, K.; Siemiarczuk, A.; Cowley, D. J.; Baumann, W. *Nouv. J. Chim.* **1979,** *3*, 443.), and van der Waals radii of reference 45.

(56) Gibson, E. M.; Jones, A. C.; Phillips, D *Chem. Phys. Letters* **1987,** *136*, 454.

(57) Schlag, E. W.; Schneider, S.; and Fischer, S. F. *Ann. Rev. of Phys. Chem.* **1971** *22*, 464.

(58) Siegel, S.; Judeikis, H. S. *J. Chem. Phys.* **1965,** *42*, 3060.

(59) McGlynn, S. P.; Azumi, T.; Kinoshita, M. *Molecular Spectroscopy of the Triplet State*; Prentice-Hall: Englewood Cliffs, NJ, 1969; Chapter 5.

(60) Rettig, W.; Wermuth, G.; Lippert, E. *Ber Bunsenges. Phys. Chem.* **1979,** *83*, 692.

(61) McGlynn, S. P.; Azumi, T.; Kinoshita, M. *Molecular Spectroscopy of the Triplet State*; Prentice-Hall: Englewood Cliffs, NJ, 1969; Chapter 7.

(62) Socrates, G. *Infrared Characteristic Group Frequencies*; Wiley: Chichester, 1980; Chapter 11.

(63) Green, J. H. S. *Spectrochimica Acta* **1970**, *26A*, 1503.

(64) Socrates, G. *Infrared Characteristic Group Frequencies*; Wiley: Chichester, 1980; Chapter 4.

(65) Langan, E. V.; Sitzmann, E. V.; Eisenthal, K. B. *Chem. Phys. Letters* **1984**, *110*, 521.

(66) Khalil, O. S.; Hofeldt, R. H.; McGlynn, S.P. *Chem. Phys. Letters* **1972**, *17*, 479.

(67) Heisel, F.; Miehe, J. A.; Martinho, J. M. G. *Chemical Physics* **1985**, *98*, 243-249.

(68) Bergmark, W. R.; Jones, G.; Reinhardt, T. E.; Halpern, A. M. *J. Am. Chem. Soc.* **1978**, *100:21*, 6665-6673.

(69) Syage, J. A.; Felker, P. M.; Zewail, A. H. *J. Chem. Phys.* **1984**, *81:11*, 4706-4723.

(70) Manring, L. E.; Peters, K. S.; Jones, G.; Bergmark, W. R. *J. Am. Chem. Soc.* **1985**, *107*, 1485-1489.

(71) Frei, H.; personal communication.

(72) Bondybey, V. *Ann. Rev. Phys. Chem.* **1984**, *35*, 591-612.

(73) Barbara, P. F.; Walsh, P. K.; Brus, L. E. *J. Phys. Chem.* **1989**, 29-34.

(74) Pimentel, G. C.; McClellan, A. L. *The Hydrogen Bond;* W. H. Freeman and Co.: San Francisco, 1960; Chapter 3.

(75) Souto, M. A.; Kolc, J.; Michl, J. *J. Am. Chem. Soc.* **1978**, *100:21*, 6692-6696.

(76) Brewer, W. E.; Studer, S. L.; Chou, P.-T.; Orton, E. *Chem. Phys. Lett.* **1989**, *158:5*, 350.

(77) Becker, R. S.; Inuzuka, K.; King, J. *J. Chem. Phys.* **1970**, *52:10*, 5164-5170.

(78) Alves, A. C. P.; Christoffersen, J.; Hollas, *J. Mol. Phys.* **1971**, *20:4*, 625-644.